Hollow core fibers for high power laser applications

Michieletto, Mattia; Bang, Ole; Lyngsøe, Jens Kristian; Lægsgaard, Jesper

Publication date:
2016

Document Version
Publisher's PDF, also known as Version of record

Hollow core fibers for high power laser applications

Mattia Michieletto

PhD Thesis

June 2016

DTU Fotonik
Department of Photonics Engineering

Tea

DTU

NKT Photonics

Preface

This thesis summarizes my work as a PhD. student at NKT Photonics A/S and DTU Fotonik. My PhD. project, titled “Hollow core fibers for high power laser applications”, is part of a Marie Curie Initial Training Network on "Quantum Sensor Technologies and Applications" (QTea). The majority of the work was carried out at NKT Photonics A/S in Birkerød in period between January 2013 and June 2016. The project was supervised by: Prof. Dr. Ole Bang, Assoc. Prof. Dr. Jesper Lægsgaard, DTU Fotonik, and Dr. Jens K. Lyngsø, NKT Photonics A/S. This work was made possible by the Marie Curie Initial Training Network QTea, financed by the FP7 of the European Commission contract-N MCITN-317485.

I thank all my supervisors for the support, guidance and knowledge sharing, without which this work would have been impossible. Particularly I would like to thank Jens K. Lyngsø , who had to deal with me daily. He has been in these years a friend and a role model. His optimism, enthusiasm and his omnipresent help and advice made the period of my PhD. studies highly enjoyable.

I wish to thanks all my colleagues and friends at NKT Photonics. Getting to know them and working with them was a great pleasure and I feel very lucky to have a future in this exciting environment. I am especially grateful to Lasse Leick and Thomas T. Alkeskjold for giving me an incredible boost and motivation when I needed it the most. Thanks to Christian Jakobsen for fabricating amazing fibers and being so enthusiastic in finding new and better ways to do so. The time spent in the drawing tower with him and Morten Buchwald was always exciting.

I also would like to thank all the people in the Qtea Network for the time spent together. Among them a special mention to Marco Triches for his companionship.

Thanks to my family for supporting me greatly and unconditionally, and in particular my parents Giuliana and Romeo. Finally I would like to thank Sarah and all my friends for their support and for the great fun.

Contents

List of Publications

Journal publications

I Mattia Michieletto, Jens K. Lyngsø, Jesper Lægsgaard, and Ole Bang, "Cladding defects in hollow core fibers for surface mode suppression and improved birefringence.", Opt. Express (2014), 23324-23332.

II Mattia Michieletto, Jens K. Lyngsø, Christian Jakobsen, Ole Bang, and Thomas T. Alkeskjold, "Hollow-core fibers for high power pulse delivery", Opt. Express (2016), 7103-7119.

III Marco Triches, Mattia Michieletto, Jan Hald, Jens K. Lyngsø, Jesper Lægsgaard, and Ole Bang, "Optical frequency standard using acetylene-filled hollow-core photonic crystal fibers", Opt. Express (2015), 11227-11241.

IV Philip G. Westergaard, Jan W. Thomsen, Marco Triches, R. Henriksen, Mattia Michieletto,Jens K. Lyngsø, and Jan Hald , "Compact, CO 2 -stabilized tuneable laser at 2 . 05 microns" Opt. Express (2015), 4872-4880.

Conference contributions

I Mattia Michieletto, Mette M. Johansen, Jens K. Lyngsø, Jesper Laegsgaard, Ole Bang, and Thomas T. Alkeskjold, "High-power picosecond pulse delivery through hollow core photonic band gap fibers" in Workshop on Specialty Optical Fibers and Their Applications, (2015), paper WF2A.4.

II Mette M. Johansen, Mattia Michieletto, Torben Kristensen, Thomas T. Alkeskjold, and Jesper Laegsgaard "High Power Performance of Rod Fiber Amplifiers", in Workshop on Specialty Optical Fibersand Their Applications, (2015), paper WT2A.5.

III Mattia Michieletto, Mette M. Johansen, Jens K. Lyngsø, Jesper Lægsgaard, Ole Bang, Thomas T. Alkeskjold, "High-power picosecond pulse delivery through hollow core photonic band gap fibers" , Proc. SPIE9728, Fiber Lasers XIII: Technology, Systems, and Applications, 97282Z (March 11, 2016)

IV Mette M. Johansen, Mattia Michieletto, Torben Kristensen, Thomas T. Alkeskjold, Jesper Lægsgaard, "85 µm core rod fiber amplifier delivering 350 W/m", Proc. SPIE 9728, Fiber Lasers XIII: Technology, Systems, and Applications, 97280I (March 9, 2016)

Patent applications

I Mattia Michieletto, Jens K. Lyngsø, Christian Jakobsen, "Hollow core optical fiber and a laser system", 23 December 2015, Patent Application: DK PA 2015 70877 (unpublished).

II Thomas T. Alkeskjold, Jens K. Lyngsø, Christian Jakobsen, Martin D. Maack, Mattia Michieletto, Sidsel R. Papior, "Photonic crystal fiber assembly", 23 December 2015, Patent Application: DK PA 2015 70876 (unpublished).

Chapter 1

Introduction

The pursuit of a hollow core (HC) fiber able to guide by the formation of a 2D photonic band gap was the thrust that lead to the creation of photonic crystal fibers (PCF). PCF are microstructured fibers that guides in virtue of either total internal reflection, anti-resonant reflection or a combination of the two. Air holes and doped glasses along the fiber suddenly offered an extreme flexibility in the design of optical fibers. Dispersion, non linearity and modal properties can be highly tailored in PCF thanks to the complex geometry and wide versatility possible with the fabrication technique. Applications flourished in many fields as optical fiber sensors, quantum optics, fiber lasers and amplifiers, and non-linear applications (supercontinnum generation as the most noticeable one).

Particularly the possibility of guiding light in a HC suggested potential for low loss, low non-linearity and low dispersion. More than this it offered long distances where light can have high intensity and diffraction-free propagation, hence providing a medium where light matter interaction can significantly be enhanced. These unique features find today applications in a multitude of fields, as I will shortly discuss in the following.

The gas composition and pressure can be exploited to tune the fiber non-linearity and dispersion. In doing so pulse compression down to few cycles and dispersive wave generation in the UV was demonstrated [1] as well as stimulated Raman scattering in gas [2]

Gas cells can be replaced with HC fibers to realize frequency standards based on saturated absorption spectroscopy [3–5]. In the field of quantum optics, cold atoms can be guided in the HC to enhance their interaction with the light field, potentially offering a 1D system where to investigate electromagnetically induced transparency [6, 7].

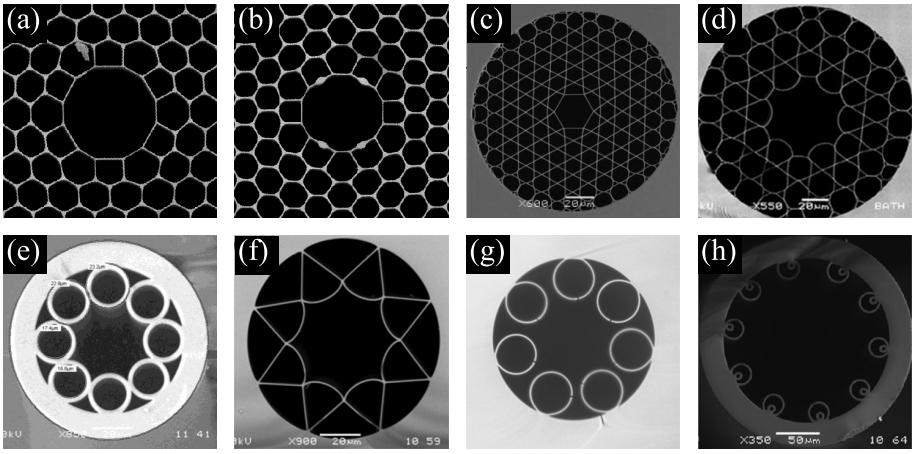

Figure 1.1: (a) SEM image of a PBG-HC fiber, (b) SEM image of a birefringent PBG-HC fiber, (c) SEM image of a Kagome HC fiber from [17], (d) SEM image of a hypocycloid Kagome HC fiber from [18], (e) SEM image of a AR-HC fiber with touching tubes from [19], (f) SEM image of a AR-HC fiber with touching tubes from [20], (g) Microscope image of a AR-HC fiber with non touching tubes, (h) SEM image of a nested AR-HC fiber from [21]

In optical communications the low latency and the exploitation of low loss high order modes (HOMs) in HC fibers renewed the interest in this technology in recent years. This allowed the realization of ultra high capacity data transmission and suggested the potential employment of HC fibers in short haul communication [8, 9].

In the field of optical fiber sensors HC fibers can be use to detect gas through spectroscopy [10–12], to realize thermally insensitive strain sensors [13, 14] and to realize optical fiber gyroscopes based on Sagnac interferometry [15].

The implementation of HC fiber based sensors and data transfer also benefits from a strong resistance towards radiation. HC fiber would indeed last much longer in high radiation environment where solid core fiber would rapidly degrade [16].

The extremely low overlap between the light and the fiber structure, beside giving low non-linearity, also translates in very high damage threshold. Because of this HC fibers can be exploited for the delivery of high power laser sources. In this field the possibility of delivering a diffraction limited beam is particularly interesting to achieve the lowest possible spatial accuracy for micro-machining, biological tissue ablation or microscopy.

Within this panorama of applications the development of HC fibers flourished in terms of their fabrication, understanding, design and engineering of their optical properties. The first photonic bandgap hollow core (PBG-HC) fiber was fabricated in 1999 [22]. Initial efforts focused at the reduction of its propagation loss leading to a record loss of 1.2dB/km at 1620nm in 2005 [23]. In applications that relies on spectroscopy, interferometry or require diffraction limited beams the propagation of a single fundamental mode is paramount. In PBG-HC fiber, though, two other kind of modes are typically propagated: high order core modes and surface modes, i.e. modes localized at the core wall of the fiber. Hence, several works were dedicated to to the design of fiber that can propagate a single core mode [24–27] and that can suppress the detrimental effects of surface modes [26, 28, 29]. Another important step in the development of PBG-HC fibers is the fiber birefringence [30–34] as in Fig.1.1(b). The introduction of birefringence allows indeed for the maintenance of the state of polarization of a linearly polarized input beam.

Few years after the first realized PBG-HC fiber a different fiber geometry was realized with a Kagome lattice [2] as the fiber in Fig.1.1(c). These fibers differentiate from PBG-HC for the typical larger core, the presence of several transmission bands, broadband guidance, higher loss and multi-mode propagation. Far more interesting, the design demonstrated that to achieve guidance in air core it is not essential to have a range of wavelengths and propagation constants where no cladding mode is present, but it is sufficient that no cladding mode couples to the core modes. The research on this kind of fiber showed how important the core wall shape is to achieve low confinement loss [35], suggesting that out of the intricate Kagome cladding the core wall is mainly responsible for guidance. An example of a Kagome fiber with hypocycloid core wall is shown in Fig.1.1(d). Tube lattice fibers were investigated numerically and in great detail by Vincetti et al. [36] in 2010. These were likely the basis upon which a new HC fiber design was fabricated in 2011 by Pryamikov et al. [19] in Fig.1.1(e). It is referred in literature as revolver fiber, negative curvature or anti-resonant fiber (AR-HC), as it will be referred in this work. The development of this new kind of HC fibers had a fast evolution and in few years several fiber design were considered with touching [37] or non touching tubes [38]. Two examples are in Fig.1.1(f) and (g). Numerical works showed that a nested version of the fiber could offer ultra low losses [39–41] (see Fig.1.1(h)) and more complex structures were proposed to improve the modal properties [42, 43] or to induce birefringence [44, 45]. AR-HC and Kagome HC fibers have

similar optical properties and the main differences relies on the lowest loss that can be achieved with AR-HC fibers for the same core size, and the typically higher bend loss of AR-HC fibers.

1.1 Scope

In this work I will consider PBG-HC fibers and AR-HC fibers. Regarding PBG-HC fibers I will focus on how to reduce the impact of low loss surface modes and their polarization properties. In the case of AR-HC I will consider the simple design consisting of non touching tubes and I will show numerically and experimentally how the design can be optimized to maximally suppress HOMs and at the same time obtain low bend loss. The work aims at developing HC fibers for a specific application that is high power beam delivery, and with this perspective two PBG-HC fibers and an AR-HC fiber were tested in the delivery of picosecond pulses. The main requirements that are expected for a delivery system to be used in micro-machining and medical sector are:

- † Diffraction limited output beam, i.e. single mode output
- † Bend robustness, i.e. no power change while the fiber is moved and no beam deformation/pointing instability
- † Polarization maintaining
- † High peak and average power

These properties will, therefore, be considered with particular attention throughout the thesis.

1.2 Outline

In Chapter 2 I will set the framework of this thesis, summarizing the main guidance features of PBG-HC and AR-HC fibers. The analysis is done for the two fibers in the same fashion by studying the mode properties of the cladding structure. This way differences and analogies between the two fiber designs can be easily highlighted. Through a detailed analysis of the modal properties of the AR-HC fibers I will show that their design can be optimized to suppress HOMs and have low loss and low bend loss.

Chapter 3 is dedicated to describe the AR-HC fibers that were drawn in NKT Photonics during my doctorate, with particular attention in the characterization of their bending performance and HOM suppression. Both numerical tools and experimental characterization will be used for this goal.

The optical properties of two PBG-HC fibers are reported in 4. In the chapter I will as well introduce an ideal structure, used to numerically simulate the fiber properties, that take into consideration the peculiarities of a real 7-cell PBG-HC fiber. Several optical properties are determine by small features of the core wall geometry. The proposed way of building the numerical model attempts to reconstruct the geometry of a drawn fiber on the sole basis of a microscope image of the fiber and the drawing parameters. The two fibers were selected for the pulse delivery experiment in Chapter 6.

In Chapter 5 I will show how the introduction of defects in the otherwise regular cladding of PBG-HC fibers can be exploited to resonantly couple surface modes to high loss cladding modes. This approach not only reduce the presence of surface modes at the operational wavelengths of the fiber but it has beneficial consequences on the fiber polarization maintenance. In the remaining part of the chapter I concentrate in characterizing the polarization properties of a PBG-HC fiber and a AR-HC fiber used in the pulse delivery experiment.

The performances in delivering a high power picosecond pulses are analyzed in Chapter 6 for two PBG-HC fibers and a AR-HC fiber.

Chapter 7 summaries the main experimental techniques used in characterizing the fibers as: spatially resolved side scattering, loss measurements, group velocity dispersion, HOMs content and polarization properties.

Conclusions and final remarks are in Chapter 8.

Chapter 2

Guiding mechanism and properties of hollow core fibers

This chapter is dedicated to a general description of the guidance mechanism of hollow core fibers. After shortly introducing a 1D model for guidance in Section 1 I will give particular emphasis to the description of the dielectric modes supported by the silica structure of the fibers, showing how they define the edges of the fibers transmission bands. The properties of these modes are indeed essential to understand how the geometrical features of the fiber affect the core modes. PBG-HC fibers are analyzed in Section 2, while AR-HC fibers in Section 3. In the case of AR-HC fibers I will show how this recently proposed fiber design [19, 37] can extend the unique properties of PBG-HC fibers to large core sizes and how this can be achieved minimizing the presence of HOMs along propagation and maintaining bend robustness.

2.1 Guidance mechanism in hollow core fibers

The guidance mechanism of hollow core fibers that consist of a single dielectric and air can be described by a simple 1D system. The idea, firstly proposed for hollow core fiber guidance by Litchinitser et al. [46], is that the cladding arrangement is such to provide a Fabry-Perot-like resonator that ensure light reflection and hence confinement for core modes. I will use here, and further on in this chapter, the Mercantili and Schmeltzer's model [47] that gives an analytical solution for a dielectric HC fiber with a circular hol-

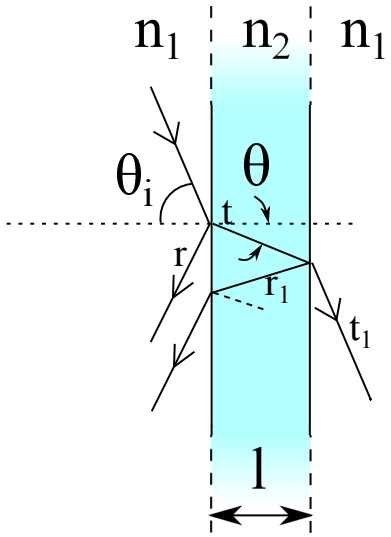

Figure 2.1: Scheme of the a Fabry-Perot etalon of thickness l.

low core and an infinite dielectric cladding. The analytical expression for the effective indices of the air modes in such a waveguide is:

$$n_{lm}(\lambda) = \sqrt{1 - \left(\frac{u_{lm}\lambda}{\pi d}\right)^2} \tag{2.1}$$

where n_{lm} is the effective index of the mode with l and m azimuthal and radial number, u_{lm} is the mth zero of the Bessel function J_{l-1}, λ is the wavelength and d the air core diameter. If we consider a Fabry-Perot etalon as in Fig.2.1, where n_1 is the refractive index of air and n_2 the refractive index of silica glass, we can set the angle

$$\theta_i = \arcsin(n_{lm}(\lambda)) \tag{2.2}$$

to account for the fundamental core mode effective index. I calculated the amplitude reflections (r and r_1) and transmissions (t and t_1) coefficients for p- and s-polarization incident light for the two interfaces in Fig.2.1 as a function of θ_i through the Fresnel equations.

The phase acquired by light in a round trip within the etalon is:

$$\delta = \frac{4\pi n_2 l \cos(\theta)}{\lambda} \tag{2.3}$$

while the etalon reflectance is:

$$R(\lambda) = \left(1 - \frac{(tt_1)^2}{(1 - rr_1)^2 + 4\sqrt{rr_1}\sin^2(\delta/2)}\right)^{1/2} \tag{2.4}$$

Figure 2.2 shows the reflectance calculated using eq.2.1 to 2.4 for an etalon of thickness $l = 0.75\mu m$, $\theta_i = asin(n_{11}(\lambda))$ and n_2 calculated with the Sellmeier equation for silica glass. The typical etalon reflectance shows several high reflectance bands separated by narrow resonances with high transmittance. The frequencies at which the narrow resonances occurs can be calculated by:

$$\nu_m = m\frac{c}{2n_2 l\cos(\theta)} \tag{2.5}$$

where c is the speed of light in vacuum and m an integer.

In all the fibers I will consider core sizes that are significantly larger than the wavelength, and hence from eq.2.1 this correspond to effective indices close to 1 and angles $\theta_i \simeq \pi/2$ and $\theta \simeq \theta_{critic} = arcsin(n_1/n_2)$. Equation 2.5 can than be rewritten as:

$$\nu_m = m\frac{c}{2l\sqrt{n_2^2 - n_1^2}} \tag{2.6}$$

These frequencies correspond to cutoff frequencies of modes in a slab waveguide.

In the following sections I will describe in details the cladding modes of PBG-HC and AR-HC fiber. The 1D model presented in this section applies more naturally to AR-HC because the tube resonator can be better approximated to an infinite slab waveguide, nevertheless I will show in the next section that the same principle of anti-resonant reflecting guidance applies to PBG-HC fibers and how the specific shape of the resonator affects the guidance properties of the fiber.

2.2 Photonic bandgap hollow core fibers

Historically the development of hollow core fibers stems from the idea of photonic band gap, i.e. the property of a three dimensional periodical dielectric structure (photonic crystal) to forbid, for a range of frequencies, electromagnetic propagation at any incident angle. Let us consider such a structure

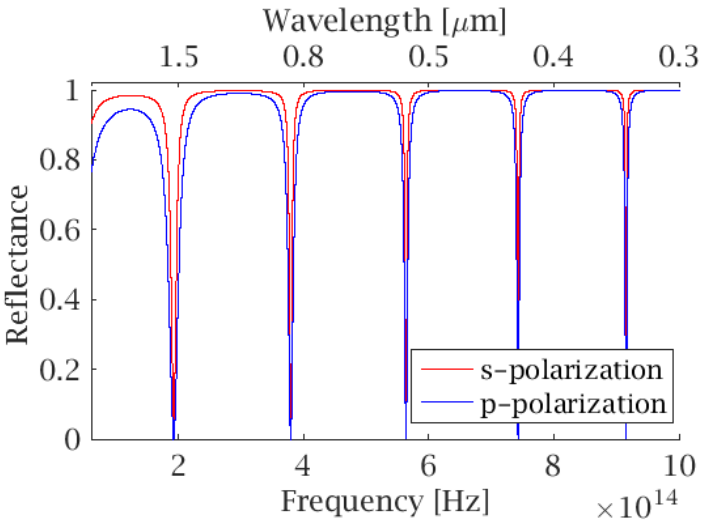

Figure 2.2: Reflectance calculated with eq.2.4

with two dielectric material of refractive indices n_1 and n_2, $n_1 < n_2$. An essential condition to achieve a photonic band gap in the plane of periodicity, such that guidance in the low refractive material can be supported, is for the two material to have a large enough refractive index difference $\Delta n = n_2 - n_1$, typically on the order of 2.2 - 2.6 [48]. If guidance in air is desired this requirement strongly restrict the choice of material to either glasses with high refractive index or semiconductors. The realization of Russell, P. St J in the early 1990s was that this condition can be greatly relaxed if one considers a two dimensional periodic structure, translationally invariant in the third dimension and out of plane of periodicity propagation. The idea is that what matters for the formation of a photonic band gap is the component of the wavevector in the plane of periodicity, and if the angle between the vector orthogonal to the plane of periodicity and the wavevector is kept small enough any two dielectric can lead to the formation of photonic band gap [49].

Guidance from a photonic crystal perspective

In order to study the properties of a given periodical structure one can adapt the techniques developed in solid state for electrons propagating in a periodical atomic potential. In the following we will consider a perfectly

periodical silica structure in air. The structure reproduces the main feature of a fabricated PBG-HC fiber cladding in Fig. 2.3(a). The pitch Λ, apex curvature D_c and strut thickness $\Lambda - D$ are 2735nm, 800nm and 87nm, respectively. The refractive index of the silica glass is approximated to be constant and equal to 1.45. I used a commercial finite element mode analysis software (COMSOL®) to find the modes supported by the cladding for a range of frequencies. The simulation is performed on one unit cell, as the one in Fig.2.3(b). The primitive vectors in the real space are defined as in Fig.2.3(b), so that $|\vec{a_1}| = |\vec{a_2}| = \Lambda$, the angle between the two is $\pi/3$ and $|\vec{a_3}| = 1$. The primitive vector in the reciprocal space are then obtain with the following equations:

$$\vec{b_1} = 2\pi \frac{\vec{a_2} \times \vec{a_3}}{\vec{a_1} \cdot (\vec{a_2} \times \vec{a_3})}; \quad \vec{b_2} = 2\pi \frac{\vec{a_3} \times \vec{a_1}}{\vec{a_2} \cdot (\vec{a_3} \times \vec{a_1})}; \quad \vec{b_3} = 2\pi \frac{\vec{a_1} \times \vec{a_2}}{\vec{a_3} \cdot (\vec{a_1} \times \vec{a_2})}; \tag{2.7}$$

so that $\left|\vec{b_1}\right| = \left|\vec{b_2}\right| = \frac{4\pi}{\Lambda\sqrt{3}}$ and $\left|\vec{b_3}\right| = 1$. The corners of the first irreducible Brillouin zones have the following coordinates: $\Gamma = (0,0)$; $\mathrm{M} = (0, \frac{2\pi}{\Lambda\sqrt{3}})$; $\mathrm{K} = (\frac{2\pi}{3\Lambda}, \frac{2\pi}{\Lambda\sqrt{3}})$.To account for the different wavevector directions, periodic Bloch boundary conditions in eq.2.8 are applied to opposite boundaries of the simulated domain. The Bloch periodic boundary conditions are defined as:

$$\vec{E_1} = \vec{E_2} e^{-i\vec{k_B}(\vec{r_1} - \vec{r_2})}; \qquad \vec{H_1} = \vec{H_2} e^{-i\vec{k_B}(\vec{r_1} - \vec{r_2})} \tag{2.8}$$

where $\vec{E_1}, \vec{E_2}, \vec{H_1}$ and $\vec{H_2}$ are the electric and magnetic fields at opposite boundaries, respectively. $\vec{k_B}$ is a vector of the reciprocal space and $\vec{r_1}$ and $\vec{r_2}$ are position vectors at the two boundaries.

In order to study the properties of the photonic band gap supported by the simulated structure it is sufficient to simulate the modes for $\vec{k_B}$ vectors belonging to the borders of the first irreducible Brillouin zone [?]. I did this for the structure in Fig.2.3 performing the mode analysis simulation for 20 different $\vec{k_B}$ vectors evenly distributed along the Γ, M and K perimeter. The results are shown in Fig.2.4, showing a bandgap that cross the airline ($n_{eff} = 1$) where no modes are supported by the structure. This means that a air defect can be engineered so that guidance in air can be achieved. The modes at the edges of the bandgap are depicted as well in Fig.2.4. Interestingly we can see that the short wavelengths edge supports modes mainly localized in the struts, the bottom edge of the bandgap supports modes localized in the air and the long wavelengths edge supports modes

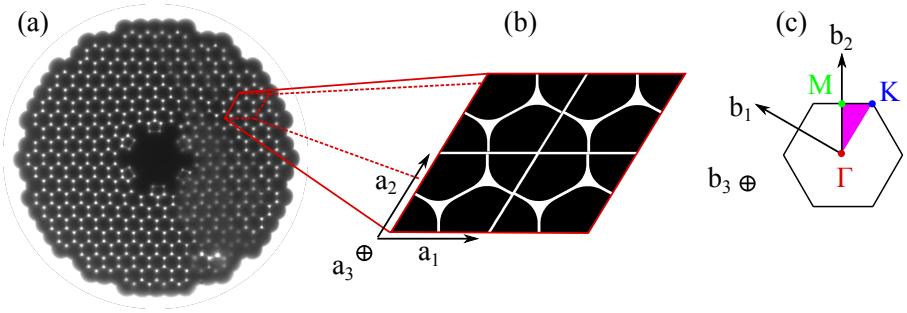

Figure 2.3: (a) Microscope image of a 7-cell PBG-HC. (b) 4 unit cells and the primitive vectors of the Bravais lattice. One of these unit sites is used for the simulation. (c) The reciprocal primitive vectors. The hexagon is the first Brillouin zone. The pink area is the first irreducible Brillouin zone, with the three corners Γ, M and K highlighted.

localized in the apexes. The long and short wavelength bandgap edges are determined by modes found at the Γ-point, while the bottom of the bandgap is defined by modes found at the K-point. A detailed analysis of the Bloch-modes in hollow-core fibers is done in [50], where these modes are also measured experimentally.

Cladding resonators and cladding modes in PBG-HC fibers

The kind of analysis presented so far is very powerful to determine whether a particular cladding structure provide a suitable bandgap for air guidance. On the other hand it is limited to analyze perfectly periodical and infinite structures and provide no information on the core modes. This of course derives from the fact that Bloch theory is meant to describe spatially delocalized modes and in the picture of photonic bandgap the air core represents a defect in the photonic crystal where optical modes are spatially confined. In order to gain information on the optical properties of the core defect modes through numerical finite element mode analysis techniques one is forced to consider the full fiber structure. I have used this brute force approach extensively to design new fibers and to have more insight on the optical properties of existing fibers. A limitation of both these numerical tools is that they offer little or no insight on the physical phenomenon that generate the photonic bandgap and core guidance. More recently the exploitation of fiber optics models offered an alternative view on the formation of a bandgap [51, 52].

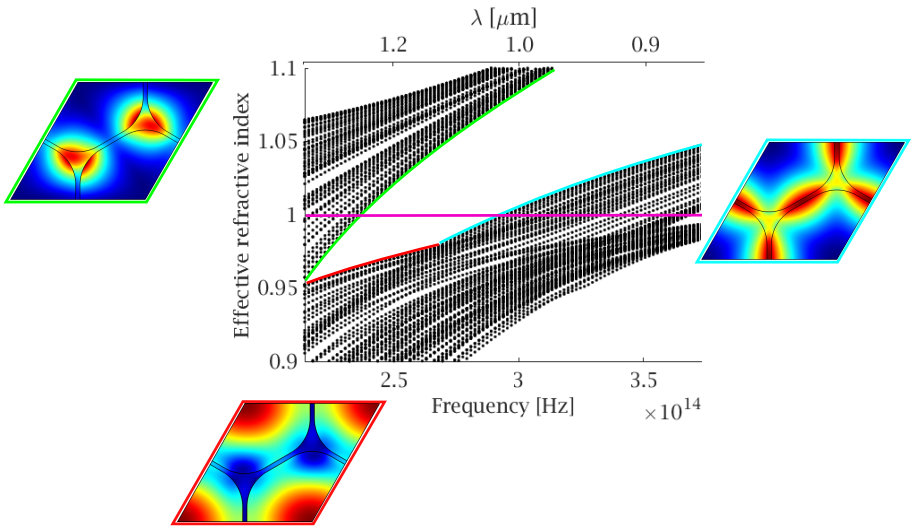

Figure 2.4: Simulation results showing the formation of a bandgap for the simulated structure. The edges of the bandgap are highlighted and the insets show the modes at the bandgap edges. The pink line is the airline.

The idea is to consider the building blocks of a photonic crystal as single optical elements called resonators. In Fig.2.4 it is clear that the cladding modes consists of modes localized either in the apexes, the struts or the air holes. In the following I will analyse the optical modes in small rods, that approximate the fiber apexes, and how the interaction of several of these rods generates the cladding modes. . The resonators in a PBG-HC fiber are the apexes and the connecting struts holding them in place. In Fig.2.5(a) the apexes are depicted in blue and the connecting struts in red.

In order to gain some insight on the formation of a photonic bandgap one can approximate the apexes with rods of radius r and the struts with rectangles connecting the rods as depicted in Fig.2.5(d). The numerical simulation of the modes supported by a single silica glass rod in air around the airline ($n_{eff} = 1$) is in Fig.2.6(a). Above the airline the vector modes localized in the rod are found and they are named after the corresponding scalar modes. Below the airline a continuum of modes in air are found. In the areas above the airline and between the modes in the rod no cladding or rod modes are allowed.

If 6 of these rods are arranged close to each other as in Fig.2.5(c) a number of interesting phenomena occur. The reason for this is that the modes

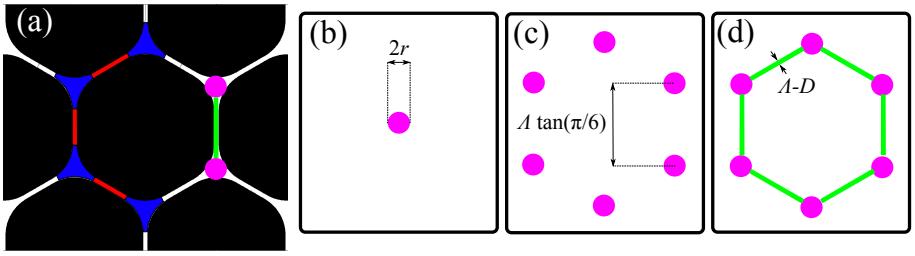

Figure 2.5: (a) The fiber structure. Blue areas are apexes, red areas are struts. The structure can be imagined as rods and connectors, in pink and green respectively. (b) a single rod of radius *r*. (c) An arrangement of 6 rods. (d) 6 rods connected by thin structures.

above the airline close to their cut off wavelength have a rather delocalized mode profile that extends significantly far away from the rod. If several rods are close enough super-modes are established, forming a broader band of modes rather than a well defined single mode effective index curve. Figure 2.6(b) shows the numerical simulation for this situation, where this effect is particularly marked for the LP_{01}-like mode. More interestingly below the airline, due to the rods interaction, several bandgaps are now open. Even though the simulation is here done for silica rods in air this holds for any two material where the refractive index of the rod is higher than the surrounding. For example it applies to solid core PBG fibers where up-doped rods in the cladding confine light in the lower refractive index core and several bandgaps are observed [53]. As shown in [54] the distance between the rods has a minor effect on the location of the bandgaps and only has an influence on their widths and on their depths. This derives from the fact that the boundaries of the bandgaps at short and long wavelengths are defined by the modes localized in the rods that depends only on the rods radius. The distance between the rods only influence the strength of their interaction and hence the broadening of the effective index curves of the supermodes. The bottom of the bandgaps are not well defined for the 6 rods and the effective index of one mode is particularly well distinguished from the rest. From the inset in Fig.2.6(b), showing the profile of this mode, it is clear that belongs to a fundamental air mode localized in the area between the rods., showing that even only 6 rods can provide air guidance. In Fig.2.6(b) the blue line is the effective index of the fundamental mode calculated from eq.2.1 with *d* equal to the fiber pitch Λ. Despite the Mercantili and Schmeltzer's analytical analitycal model is developed for a rather different fiber structure the effec-

tive index of the air-mode in the simulation is in qualitative agreement with the analytical effective index from the model. With this analogy it became clear that a reduction of Λ, i.e. d in the model, leads to a lowering of the effective index of the air-mode that defines the bottom of the bandgaps as predicted by eq.2.1. This explains why fiber with smaller pitch shows deeper bandgaps.

The contribution given by the connecting struts is shown in Fig.2.6(c). The presence of the struts shifts the bandgaps at high frequencies upwards. A new set of modes localized in the struts limits the low frequency bandgap, that is the widest remaining. The boundaries of this bandgap are formed at short wavelengths by strut modes, at long wavelengths by rod/apex modes and the bottom by air-modes, showing close resemblance to the results obtained for the realistic infinite photonic crystal in Fig.2.4.

Core modes, surface modes and anti-resonant guidance

The analysis of the formation of the optical modes defining the cladding modes facilitates greatly the description of the modes localized in the core. The two more typical ways to form the core defect is to remove either 7 or 19 cells in the cladding periodical structure. Figure 2.7 shows an ideal 7-cell PBG-HCF. This structure has a periodical cladding. The first ring of holes around the core consists of alternating hexagons and pentagons. The core radius R is 1.5Λ. The core shape is a dodecagon. The thicknesses t_h and t_p are related by the following equation [26]: $t_h = t_p - 0.35\,(\Lambda - D)/2$. This account for the way the fiber stack is arranged. The introduction of the core forms three "defects" respect to the periodical cladding: the air core, the core wall struts and the core wall apexes. From eq.2.1 we expect the fundamental core mode to have larger effective index than the bottom edge of the bandgap. The difference in size of the struts and apexes in the core wall are responsible for the formation of surface modes, i.e. modes localized in the proximity of the core wall. Surface modes can significantly compromise the low loss and beam quality of the fundamental core mode [55, 56]. The surface modes can be categorized in modes that localize in the core wall struts (type 1) and modes that localized in the core wall apexes (type 2).

Figure 2.8 shows the simulation of a 7-cell PBG-HCF with two rings of holes surrounding the core where different core wall thicknesses are considered. The core wall thickness affect both the size of the core wall struts and apexes. In Fig. 2.8 (a) the type 1 (green lines) surface modes are outside of the bandgap, the fundamental mode (red line) and the first HOM (blue line) are within the bandgap as well as a set of type 2 (pink lines) surface

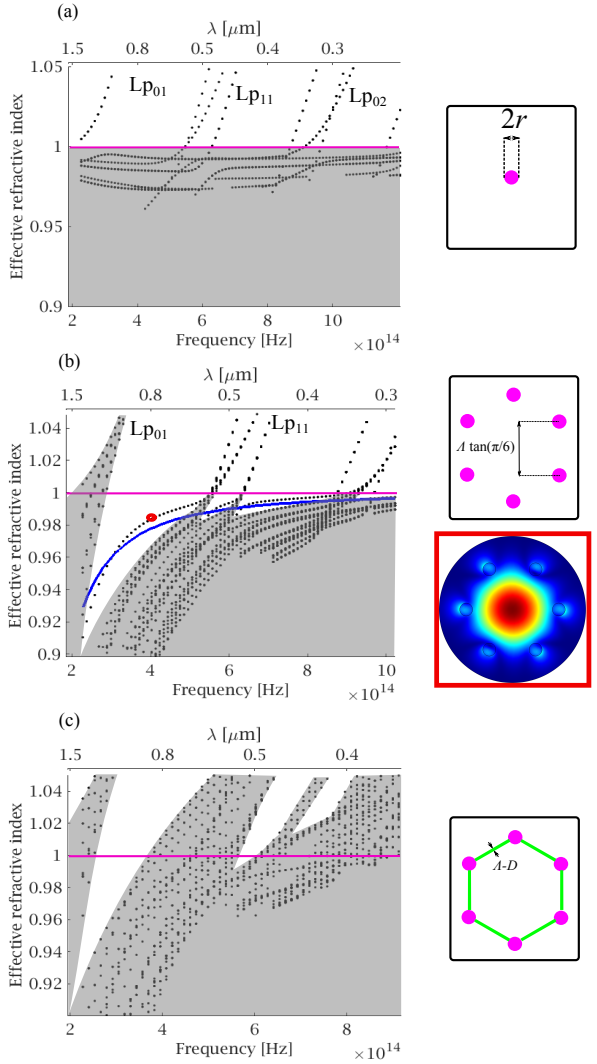

Figure 2.6: Bandgap formation. The pink line is the airline. The gray areas support dielectric and air cladding modes. The white areas do not support modes in the rods and in air. (a) Simulation performed on a single silica rod in air. Above the airline the mode confined in the rod can be observed. (b) Because of the interaction between the 6 rods several bandgaps are allowed below the airline. In blue there is the effective index of the fundamental mode for a dielectric hollow tube of radius Λ,with infinite thickness according to the Mercatili and Schmelter's model. In the inset the mode profile of an air guided mode. (c) The presence of connecting struts strongly distorts the bandgaps, leaving only a major one at low frequency below the airline.

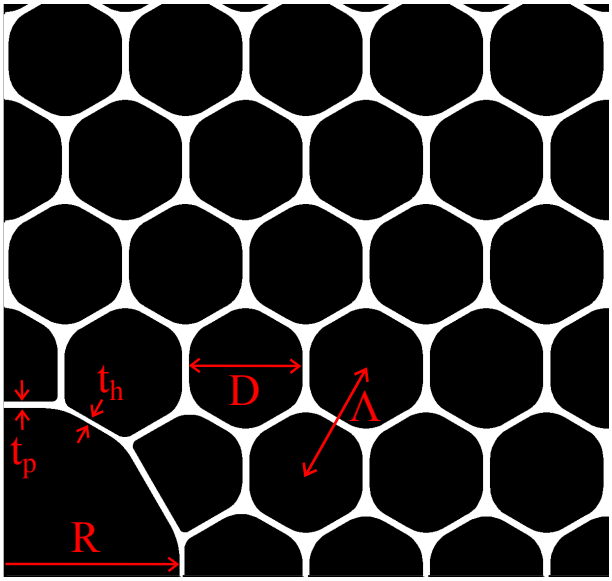

Figure 2.7: Ideal structure of a 7-cell PBG-HCF.

modes. As t_h is increased a new set of type 1 surface modes enters the bandgap from the short wavelength edge and the type 2 surface modes shift towards longer wavelengths Fig.2.8 (b),(c). Eventually the type 2 surface modes moves out of the bandgap and only type 1 surface modes are left. Figure 2.8 (c),(d) also shows a typical avoided crossing between a surface mode and the fundamental mode.

It is hence clear that the design of the core wall geometry strongly affects the guidance of core modes. This was shown in several publications both numerically and experimentally [26, 28, 57]. Furthermore it can be notice that, in the case the short wavelength edge of the bandgap is free of surface modes, single mode propagation can be obtained. In Fig. 2.8(a), for instance, there is a ~70nm bandwidth close to the short wavelength bandgap edge where the fundamental mode is guided and the first HOM lies outside of the bandgap and consequently is coupled to cladding modes and have very high loss [26].

The guidance mechanism responsible for the confinement of core modes is antiresonant reflection of the cladding [46], rather than Bragg reflection from the periodical photonic crystal, as described in the previous section. The fact that the bandgap location is nearly unaffected by the fiber pitch if the rod size is kept constant and that the localization of an air mode

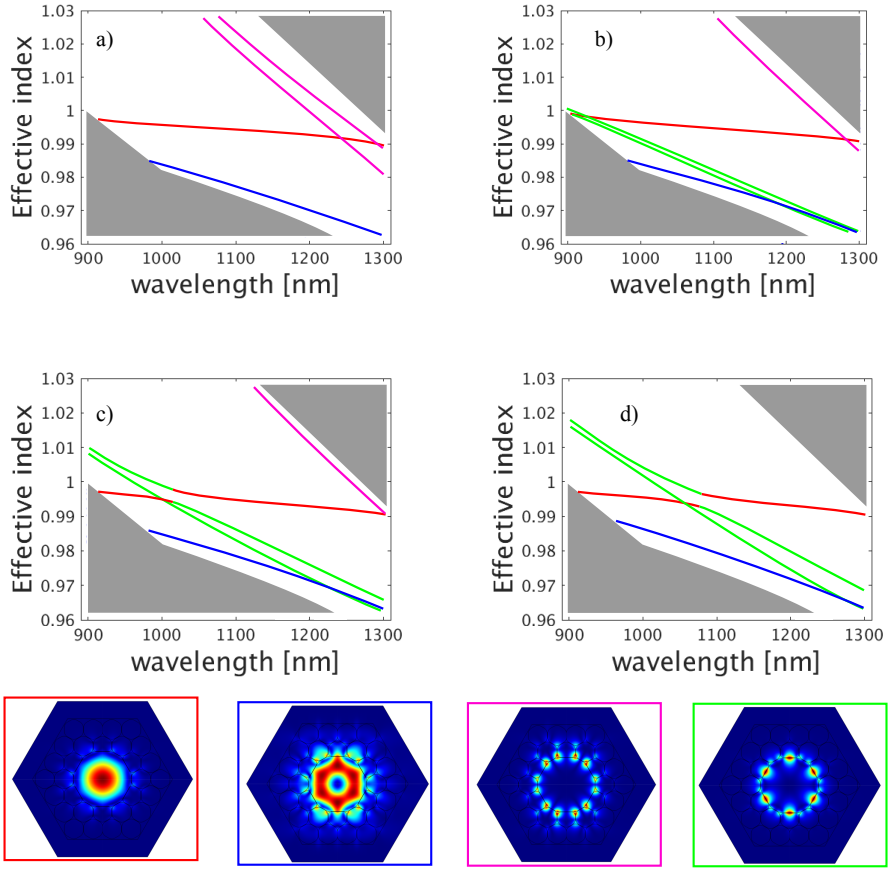

Figure 2.8: Simulations of a 7-cell PBG-HC with different core wall thicknesses: a)$t_h = 0.5 \times (\Lambda - D)$, b) $t_h = 0.85 \times (\Lambda - D)$, c) $t_h = 1.025 \times (\Lambda - D)$, d) $t_h = 1.2 \times (\Lambda - D)$. At the bottom the electric field amplitude are shown. The fundamental mode in the red box, a core high order mode in the blue box, a type 2 apex-like surface mode in the pink box and a type 1 strut-like surface mode in the green box.

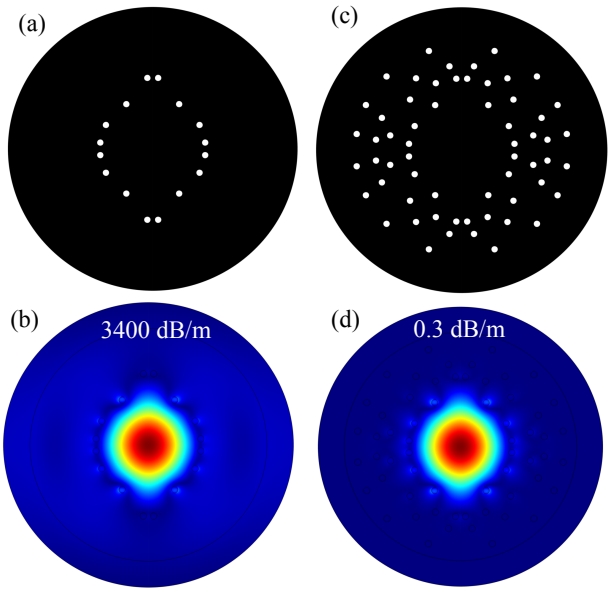

Figure 2.9: (a) Fiber structure with one layer of randomly spaced rod. (b) Fundamental mode of the fiber in (a) and its confinement loss at 1μm. (c)Fiber structure with several layers of randomly spaced rods. (d) Fundamental mode of the fiber in (c) and its confinement loss at 1μm

can be achieved with only 6 rods (Fig.2.6) strongly suggest that Bragg reflection can not be responsible for confinement. In order to further prove this I have performed a simulation of a fiber that consists of a randomly arranged silica rods with one layer of rods and several layers of rods. Figure 2.9(a),(c) show the structures of the two fibers, while figure 2.9(b),(d) show the corresponded guided fundamental modes. Not only the random rod arrangement can provide air guidance, but several layer of randomly arranged rods and drastically decrease confinement loss from ~3400 dB/m to 0.3 dB/m. This shows that the relative distance of the rods does not play a major role in the confinement mechanism of this fibers ruling out Bragg reflection where the distance of the cladding layers is essential to ensure guidance. Each silica rod acts as a reflecting element for light traveling in air at a grazing angle for wavelengths that are away from resonances. The resonances occur at the cut-off frequencies of the modes supported by the rod arrangement. For this fibers the 1D Fabry-Perot model fails to give any relevant prediction on the fiber guidance because it does not consider the two dimensional resonator features.

Fundamental mode attenuation

There are two main contribution to the loss of the fundamental mode: the confinement loss and the scattering loss. The confinement loss can be arbitrary reduced within the transmission band simply by increasing the number of resonators in the periodical cladding. Nonetheless the confinement loss gives an important contribution in defining the edges of the transmission band [58]. The scattering loss arises from the roughness of the glass/air interfaces. As described in [23] during the fiber manufacture surface capillary waves are frozen in the glass as its temperature decreases below the glass transition temperature. There were several attempt to measure the roughness of the silica in the PBG-HC fiber [23, 59, 60] and also several works dedicated to the description of how the scattering loss can be expressed in terms of the surface roughness of the fiber [23, 58, 61, 62]. Despite the efforts it is still very challenging to estimate numerically and reliably the fiber scattering loss. The typical approach is to assume that within the band the scattering loss is proportional to the field along the glass/air interfaces and hence proportional to the following :

$$F = \left(\frac{\epsilon_0}{\mu_0}\right)^{1/2} \frac{\int_{glass/air} \left|\vec{E}\right| dl}{\int \vec{E} \times conj(\vec{H}) \cdot \vec{z}\, dA} \tag{2.9}$$

The fundamental mode scattering loss can therefore be expressed as [40]:

$$\alpha_{scattering}[dB/km] = \eta F[\mu m^{-1}] \left(\frac{\lambda[nm]}{1550nm}\right)^{-3} \tag{2.10}$$

where $\eta = 300$ is a proportionality factor obtained empirically.

A rigorous approach in [63] showed that assuming thin film surface capillary waves and strong perturbation mode coupling theory an accurate numerical estimation of the scattering loss of real fiber is possible. Nevertheless the computational requirements are quite stringent since approximately 1000 modes are required to be found at a given wavelength.

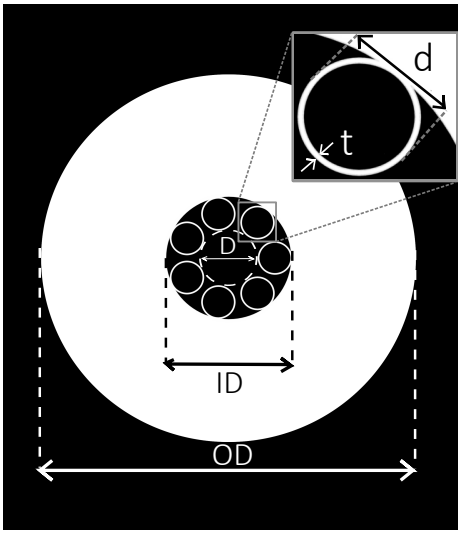

Figure 2.10: Scheme of an antiresonant hollow core fiber

2.3 Antiresonant hollow core fibers

Antiresonant hollow core fibers comes in a variety of kinds. The one I will consider is formed by a number of non-touching silica tubes that defines a hollow core as depicted in Fig. 2.10. The guidance mechanism of these fibers is the same as for PBG-HCF. The difference between the two is the resonator that provides antiresonant reflection and more importantly the fact that in the core proximity no other kind of silica structure is present but the elements providing confinement.

In order to describe the guidance of this kind of fiber I will go through a similar analysis as the one done for the PBG-HCF taking particular care in the description of cladding modes.

Dielectric tube modes

Vincetti et al. did a detailed analysis of the cladding modes in tube fibers in [36]. I will here summarize the major features of these modes. Figure 2.11 shows some of the supported dielectric modes for a silica tube in air of outer diameter d and thickness t. The first and second mode numbers are the azimuthal number of periods μ and radial number of maxima and minimaν of the electric field, respectively. It is useful to introduce a normalized frequency based on Eq. 2.6: $F = 2t\sqrt{(n^2-1)}/c$, where n is the silica refractive index

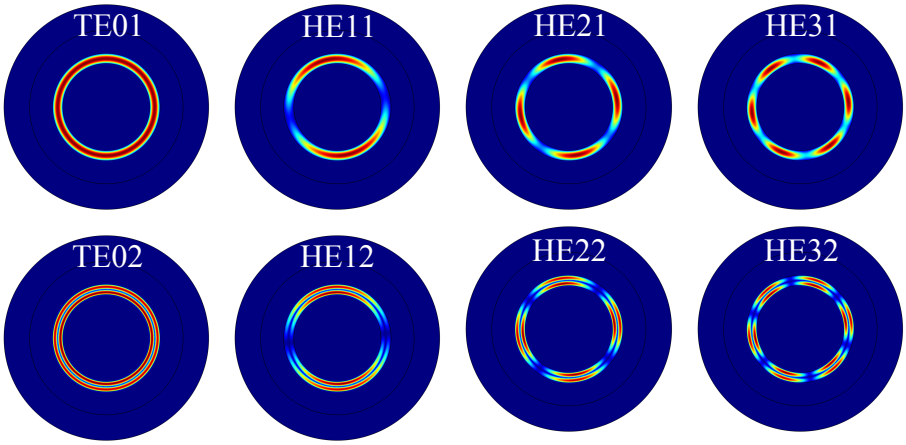

Figure 2.11: Dielectric modes supported by a silica glass tube in air.

and c the speed of light in vacuum. We are interested in the properties of the dielectric modes in proximity of the airline where they can couple with air modes due to the similar effective index. This means that we are interested at these modes at their cut-off frequencies. As I will show their optical properties define the transmission bands and the bandwidth of the high loss regions in AR-HC fibers.

Figure 2.12 shows the cut-off frequencies of dielectric modes with μ number up to 4 as a function of the ratio between the inner diameter and outer diameter of the tube. The cut-off frequencies of modes with different ν number are well distinguished for $(d-2t)/d > 0.6$, while they get mixed up at lower $(d-2t)/d$ values. Moreover as the $(d-2t)/d$ ratio tends to 1 the cut-off frequencies of modes with the same ν number converge to the same value that is a normalized frequency integer. Many other modes with higher μ number are present in the frequency range considered but are omitted. Dielectric modes with high μ number present high spatial variations that lead to a reduction of field overlap with air modes with low azimuthal variations leading to a very week coupling. If a fixed thickness t is considered, the ratio $(d-2t)/d = 1$ correspond to a tube with infinite diameter d. This situation correspond to a slab waveguide made of a silica layer in air and as expected integer values of the introduced normalized frequency correspond to the cut-off frequencies of TE modes of such a

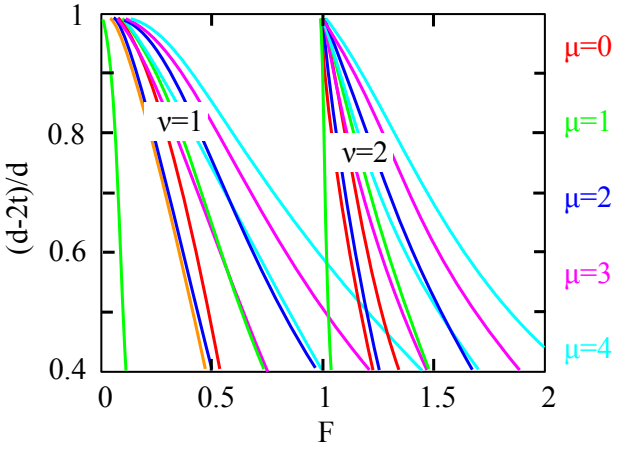

Figure 2.12: Cut-off frequencies of the dielectric modes in a tube as function of the ratio between the inner diameter and the outer diameter of the tube

waveguide [36] and they match as well the analysis done by Litchinitser et al. in [46] for antiresonant reflecting photonic crystal optical waveguides.

The results for lower values of $(d-2t)/d$ in Fig. 2.12 not only explain why in tube fibers we observe high loss region at specific frequencies, but they explain as well the bandwidth of the high loss regions. The cause of it is the presence of dielectric modes with different μ number that couple to air modes in the fiber.

In order to prove this experimentally I performed a near field measurement of a fiber in Fig.2.13(b). The measure was done over a 6cm fiber. The fiber transmission spectrum is depicted in Fig.2.13 (a). The laser I used is a narrow linewidth laser tunable from 1509nm to 1630nm. At 1509nm the laser is within the fiber transmission band. At this wavelength I ensured that the light is optimally coupled to the core. The output near field was recorded with an infrared Vidicon camera C2741. The near field at 1564nm in Fig.2.13(d) clearly shows the coupling between the core mode and a dielectric cladding mode that correspond to a HE23. Figure 2.13(c) shows a HE23 dielectric mode in a tube close to its cut-off frequency. The dielectric mode in the near field measurement appears distorted most probably because of the touching point with the outer cladding, but the 6 lobes as well as the two radial maxima are clearly visible.

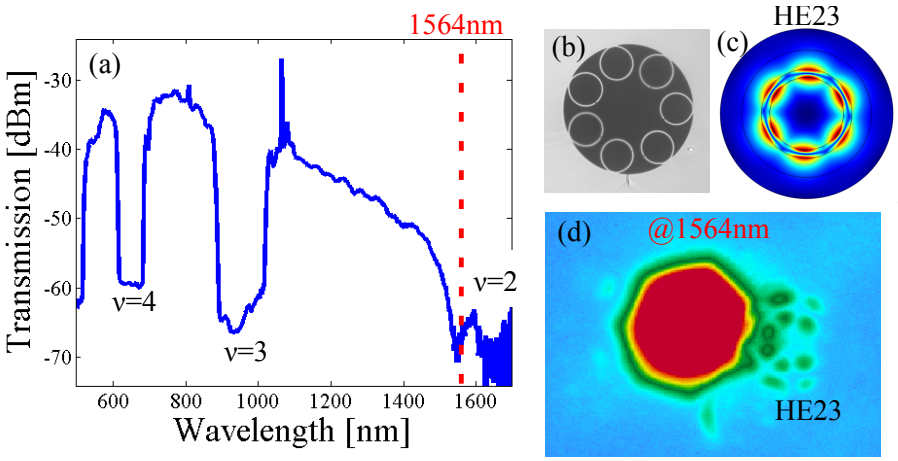

Figure 2.13: (a) Transmission spectrum through 2m of fiber. Each high loss region is marked with the ν number corresponding to the dielectric modes responsible for it. (b) Fiber facet (c) HE23 close at its cut-off frequency (d) Near field image obtained launching a tunable narrow linewidth laser in the fiber core and measuring the output near field after 6cm fiber. The near field shows the coupling between the fundamental mode and the HE23 dielectric mode in the cladding. The core light is saturated on purpose to enhance the visibility of the cladding mode.

Air tube modes

I will now discuss the air modes that localize inside the tube. I have performed a simulation of a tube of outer diameter d=21µm and thickness t=0.75µm. The cut-off wavelengths for dielectric modes with $\nu = 2$ and $\nu = 3$ are can be calculated using the following equation [46]:

$$\lambda_{\nu-1} = \frac{2t}{\nu - 1}\sqrt{n^2 - 1} \tag{2.11}$$

and equals to 1575nm and 787.5nm, respectively. The simulation is done in this wavelength range. Figure 2.14 shows the modes effective index. The modes in red are dielectric modes with low μ number (type 2) and determine the transmission edges of the air modes. Several dielectric modes with high μ number (type 1) are present at any frequency. The modes in green are the fundamental mode confined in the tube air core (upper effective index line) and several high order modes. I here compare the effective index of air modes with the analytical prediction from the Mercantili and Schmeltzer's

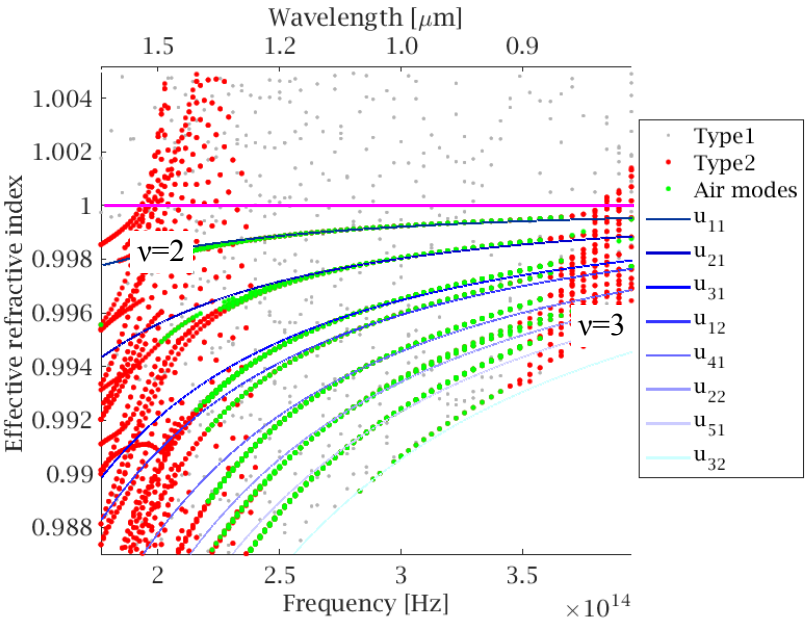

Figure 2.14: Simulation of the optical modes supported by a silica tube in air across the airline. Type1 modes in gray are dielectric modes with high μ number. Type2 modes in red are dielectric modes with low μ number. Air modes are in green. The continuous lines are the analytical effective indices of air modes calculated with the Mercantili and Schmeltzer's model. u_{lm} is the mth zero of the Bessel function J_{l-1} and identifies different modes in the model (see eq.2.1). The air line is pink.

model [47]. The continuous blue lines in 2.14 are calculated with 2.1. The is a remarkable agreement between the analytical model and the numerically simulated effective index of air modes, especially far away from type 2 dielectric modes. Deviations are visible at the edges of the transmission band where the air modes couple to type 2 dielectric modes.

Core modes in AR-HC fibers

The idea behind AR-HC is to exploit a number of tube resonator to form an air core where light can be confined and guided. If now we compare the results in Fig.2.14 for the tube resonator to the simulation for the rod resonators for PBG-HC in Fig.2.6 we can notice several similarities. The transmission edges are determined by dielectric modes at their cut-off frequencies

there is an area below the airline where a core mode can be obtained, and the lower part of the anti-resonant region is defined by cladding air modes. There are two main differences due to the different shape of the resonators and their arrangement:

1. Within the anti-resonant region there are dielectric modes for the tube resonator, while they are absent for the rod resonator. This is due to the different resonator shapes.

2. The air modes that clearly define a bottom edge of the anti-resonant region in the rod resonators have discrete effective index curves in the tube resonator. The effective index of the air modes in the tube resonator are much closer to the airline. This is mainly due to the specific rod arrangement that allows air confinement.

The first difference have a minor impact since the coupling between type 1 dielectric modes and air modes is generally negligible. The second difference is more relevant. It means that in the design of AR-HC fibers one has to consider that the core defined by and arrangement of tube resonator have to be such that the effective index of the fundamental core mode differ significantly from the effective index of the tube air modes. This condition can easily be fulfilled for core sizes larger than the inner tube diameter, since in this case the effective index of the fundamental core mode will be higher that the fundamental tube air mode, as it can be seen from eq.2.1. Low loss confinement can be achieved as well for core sizes smaller than the tube inner diameter if the effective index of the fundamental core mode is such to sit in between the effective index of tube air modes. Within this work only AR-HC fibers with cores larger than the inner tube diameter were considered.

The transmission bands in AR-HC fibers can be numbered based on the ν number of the dielectric modes that defined the edges of the transmission band. First band is delimited by dielectric modes with ν numbers 1 and 2, second band by dielectric modes with ν numbers 2 and 3, and so on.

Number of tubes in AR-HC and HOM suppression

The following considerations were part of a publication in Optics Express [64]. In the frame considered in this work of equal size non-touching tubes AR-HC fibers, as depicted in Fig. 2.10, the number of independent parameter to define unambiguously the fiber geometry is five. For example this set can be defined: the outer diameter OD, the diameter of the largest inscribed

circle in the core D, the outer diameter of the tube d, the thickness of the tubes t and the number of tubes n.

The outer diameter OD has a minor impact on the optical properties of the fiber, but it is relevant to control the fiber sensitivity towards micro-bending. Fibers with a relatively thin solid outer cladding show high sensitivity to micro-bending, for example leading in a distorted output near field due to the fiber clamping. To minimize this a large OD is preferred.

The core size D dictates the effective index of the core modes approximately following Eq.2.1, and the macro bend induced loss in the fiber.

The thickness of the tubes t, as discussed previously in this section and in section 2.1, defines the cut-off frequencies of the dielectric tube modes and hence the fiber transmissions bands.

The tube outer diameter d mainly influences the effective index of the air tube modes.

The number of tubes n sets the maximum ratio d/D that can be achieved in the fiber geometry and it consequently has a major impact on the modal properties of the fiber.

My aim in designing these fibers is to obtain a large core hollow core fiber able to deliver a single optical mode over a short distance and to be insensitive to bending. HOM suppression in a large core (>20µm) HC fibers can be achieved exploiting resonant coupling to cladding modes [27]. As shown by Uebel et al. [65] Eq. 2.1 can be used to evaluate the ratio d/D at which the LP_{11} core mode couples to the fundamental air mode in the cladding tubes as follow:

$$n_{11}^{core} = n_{01}^{tube}, \qquad 1 - \left(\frac{u_{11}}{\pi f_{core}}\right)^2 \left(\frac{\lambda}{D}\right)^2 = 1 - \left(\frac{u_{01}}{\pi f_{tube}}\right)^2 \left(\frac{\lambda}{d-2t}\right)^2 \quad (2.12)$$

$$\frac{d-2t}{D} = \frac{u_{11}}{u_{01}} \frac{f_{core}}{f_{tube}} = 0.68 \quad (2.13)$$

where $f_{core} = 1.077$ and $f_{tube} = 0.991$ are correction factors for the analytical core and tube effective index, respectively.

Interestingly Eq.2.13 shows that the coupling is broadband and moreover it sets a reference to the ratio d/D needed to resonantly couple the LP_{11} core modes to cladding modes. The maximum ratio d/D that can be achieved in the considered fiber geometry as a function of the number of tubes n is:

$$\left(\frac{d}{D}\right)_{max}(n) = \frac{\sin(\pi/n)}{1-\sin(\pi/n)} \qquad for \quad n \geq 3 \tag{2.14}$$

In order to analyze the impact of different number of tubes in the following I simulated a number of fiber geometries fixing 3 of these parameter and focusing on n and d. OD is irrelevant for the simulation where an infinite solid cladding is considered by the use of a perfectly matched layer. D and t are set to 30µm and 750nm, respectively. The core size is chosen to obtain low confinement loss and bend loss, while the thickness is optimize to have the minimum loss at 1032nm in the second transmission band. The specific choice of using the second transmission is to ease the fabrication. Using Eq.2.14 one can determine that the condition in Eq.2.13 can only be fulfilled if $n \leq 7$. On the other hand having less than 6 tubes would lead either to a pronounced gap between tubes or to have $d \geq D$. Both scenarios are detrimental because of higher confinement and bend loss, and cladding modes with similar and/or higher effective index than the fundamental core modes, as discussed in the previous section. Because of these arguments only 6- or 7-tube AR-HC fibers are considered in the following.

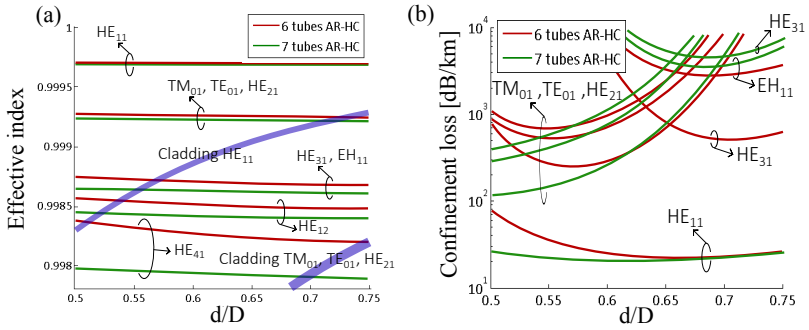

Figure 2.15: Results of simulations with constant D=30μm and t=750nm for two AR-HC fiber designs with 6 tubes (red curves) and 7 tubes (green curves). (a) Modes effective indices vs ratio d/D. The effective indices of the cladding modes are the same for the two fiber and represented by blue bands. The upper band correspond to a number of HE_{11}-like modes localized in the tubes, while the lower band correspond to TM_{01}, TE_{01}, and HE_{21}-like modes. (b) Corresponding mode confinement loss vs d/D.

Figure 2.15 (a) show the effective index as a function of the ratio d/D for several core modes in the case of a 6- and 7-tube design. The effective

index of the cladding HE_{11} mode is split into several modes because of the establishment of supermodes due to the interaction among neighbor tubes. This applies as well for the high order cladding TM_{01} , TE_{01} , and HE_{21} - like modes. As expected the effective index of the cladding modes depends only on the tube size and they are the same for the two fiber designs. They are depicted as blue bands. The effective indices of the HE_{11}, TM_{01},$TE_{21}$and HE_{21} core modes are nearly identical for the two fiber design, while a larger difference can be observed for other HOMs. In both case the effective indices of the cladding HE_{11} modes cross the TM_{01},$TE_{21}$and HE_{21} effective indices at approximately$d/D = 0.72 - 0.73$. This is in agreement with the requirement given by the analytical model in Eq.2.13(d=21.6μm, D=30μm, t=750nm). Figure 2.15 (b) shows the loss of the core modes as a function of the d/D ratio. The loss of the HE11, TM01, TE01 and HE21 modes behave analogously for d/D>0.65 showing a larger loss at larger d/D values due to the coupling with cladding modes. At shorter values the discrepancy between the two designs is due to the larger gap between neighboring tubes in the 6-tube fiber that leads to higher confinement loss. More interestingly the loss of the HE_{31} modes differ significantly in the two cases. The reason for the lower loss of the HE_{31} ($\simeq 0.4-0.5dB/m$) in the 6-tube design derives from the tube different tube arrangement. Figure 2.16 shows the HE_11 and HE31 modes for the two designs. As I have shown in section 2.1 s-polarized light shows higher reflectance in the 1D model, and here similarly the HE31 mode shows lower confinement loss in the 6-tube design because the polarization profile of the mode can be accommodated in the fiber core so to have the electric field mostly parallel to the air/silica interfaces. The same condition can not be accomplished in the 7-tube design due to the different symmetry between the mode and the fiber, resulting in higher loss. The same behavior can be observed in the 3dB contour plot of the amplitude of the electric field of the fundamental mode in both fiber. The electric field penetrate more through the silica structures when the field is orthogonal to the air/silica interface.

For this reason the HOM extinction ratio, i.e., the ratio between the confinement loss of the lowest loss HOM and the fundamental mode, differs greatly for the two AR-HC fibers, as shown in Fig.2.17(a). For d/D> 0.65 the 7-tube design shows a much higher HOM extinction ratio above 150. Let me consider a 7-tube fiber with d/D=0.7, beside of the HOM extinction ratio it is interesting to notice the absolute value of the confinement loss of the lowest loss HOM. In this case it is approximately 3.7dB/m, while the loss of the fundamental mode is 0.022dB/m. Over 5 meters of fiber the HOM loss

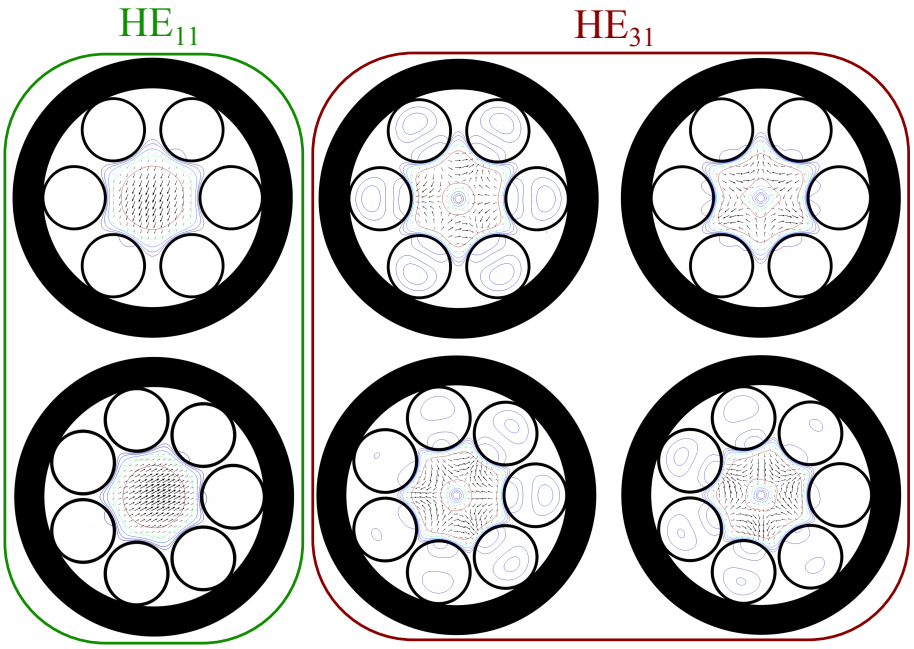

Figure 2.16: Vector representation of the calculated transverse electric field of one HE_{11} and both HE_{31}modes (arrows) with 3dB contour lines of the amplitude of the electric field. Upper row is for a 6-tube AR-HC fiber, lower row is for a 7-tube AR-HC fiber.

would be larger than 18dB. Figure 2.17 (b) and (c) show the confinement loss of the fundamental mode versus d/D and the effect of bending on it. The two fiber shows a similar trend, as discussed earlier confinement loss for $d/D < 0.65$ is higher for the 6-tube design due to the larger gaps between neighboring tubes.

Confinement and bend loss

Regarding the confinement loss of the fundamental mode and its bend loss, Fig.2.17(b) and Fig.2.17(c) show that there is no clear advantage in exploiting either of the two designs for d/D> 0.65, since all loss curves are practically on top of each other. However, the 7-tube AR-HC fiber shows a remarkably weak dependence of the fundamental mode confinement loss on d/D (Fig.2.15(b)) that is below 30dB/km for the whole considered range of d/D values from 0.5 to 0.75. This not only facilitates fabrication, but allows

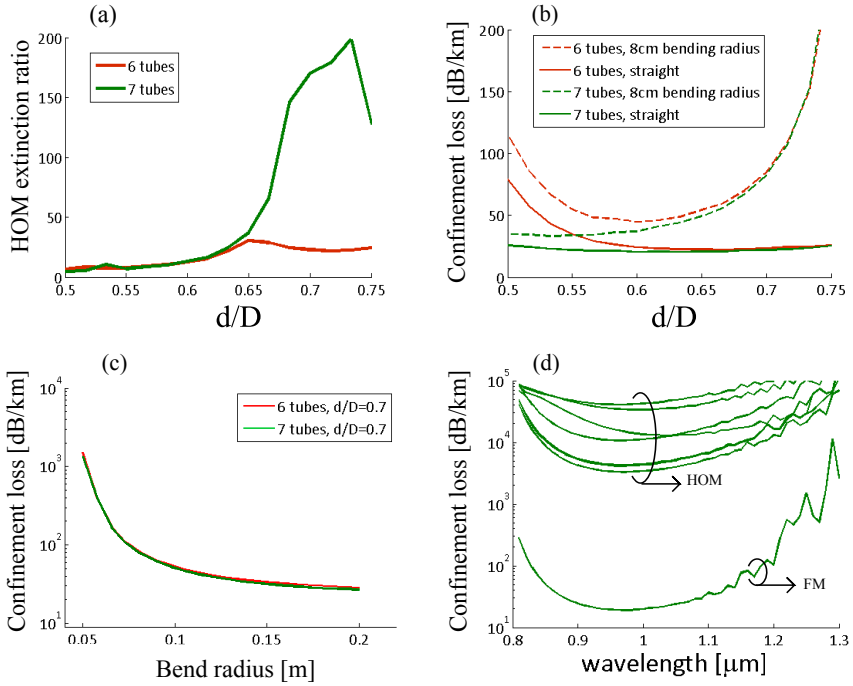

Figure 2.17: Results of simulations with constant D=30μm and t=750nm for two AR-HC fiber designs with 6 tubes (red curves) and 7 tubes (green curves). (a) HOM extinction ratio vs ratio d/D. (b) Confinement loss of the fundamental mode vs d/D for a straight fiber and a bent fiber. (c) Confinement loss of the fundamental mode vs bend radius for d/D=0.7. (d) 7 tube AR-HC spectral confinement loss of the fundamental mode and lower loss HOMs

to adjust d/D during fiber drawing either to target high HOMs suppression for d/D > 0.65 or lower bend loss for d/D < 0.65 with minimal consequences for the confinement loss. Furthermore Fig.2.17(d) shows that the low confinement loss and the HOM suppression are obtained for a bandwidth of 200-300nm for the 7-tube design. While in this contest the simulation is limited to the second transmission band of the fiber to reduce the computational time, there is no reason to expect different behavior in all the other transmission bands.

2.4 Conclusions

I have shown how the anti-resonant reflection guidance applies to PBG-HC fibers and AR-HC fibers. In PBG-HC fibers a careful design of the core wall geometry is essential to determine the fiber optical properties, in particular it strongly affects the location of surface modes within the transmission band. AR-HC are surface modes free. With the considered design low loss can only be achieved with large core sizes. I showed that the nature of the cladding modes in AR-HC is analogous to that of PBG-HC. The "airy" cladding modes in AR-HC are such that the fiber can be designed to suppress HOMs by resonantly couple them to high loss cladding modes. This is maximized in a fiber with 7 non-touching cladding tubes. Therefore this shows that is possible to have a large core hollow core fiber that has nearly single mode propagation, low loss and that is robust toward bending. Most remarkably this can be achieved within the whole transmission band.

Chapter 3

Novel antiresonant hollow core fiber

In the course of my doctorate several AR-HC fibers were fabricated at NKT Photonics. All the fibers were produced with the stack and draw technique. As discussed in Section 2.3 the focus is on the tube fiber design where the tubes are not touching. The main challenge in the fabrication of this AR-HC fiber design is to obtain identical tubes in order to achieve a symmetrical fiber. In contrast with PBG-HC where the capillary tubes are touching and stabilizing each other in AR-HC they have the tendency to behave indepen-

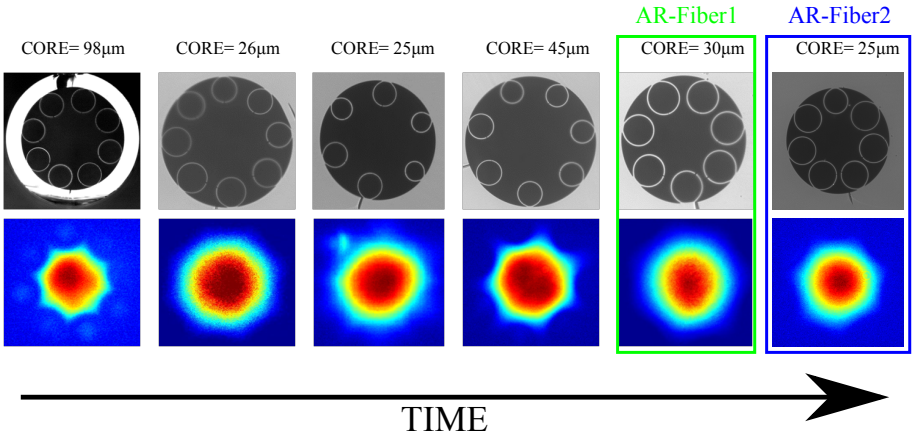

Figure 3.1: Summary of the fabricated fibers. Top row are microscope images of the fiber facets. Bottom row are near field images.

	D [μm]	t [μm]	d/D [μm]	d_1/D [μm]	n
Target design	30	0.750	0.7	X	7
AR-Fiber1	30	0.83	0.568	X	7
AR-Fiber2	25	0.72	0.644	0.557	7

Table 3.1: Structural parameters of the realized fibers are compared to the design target.

dently. Particular care is hence necessary in the positioning and welding of the capillary tube to the outer solid cladding, as well as during the drawing to fiber. Figure 3.1 shows some of the fabricated fibers. While at the beginning fibers with 8 or 6 tubes where fabricated the target in time shifted towards 7 tubes fibers with the aim of achieving a fiber able to suppress HOMs as well as being robust towards bending. The geometrical specifications that we were aiming at derive from the analysis done in Section 2.3. Interestingly this kind of fiber proved to be extremely robust and even asymmetrical fibers with large variations in tube sizes could guide light in the core. In the following I will concentrate on the last two fibers in Fig.3.1, describing their optical properties and comparing them to numerical simulations. AR-Fiber1 has a rather symmetrical structure and tube to tube variation are not accounted for in the numerical simulations. On the contrary AR-Fiber2 shows one tube that deviates significantly from the others and I consequently account for it in the numerical model. Table 3.1 summarizes the geometrical parameters of the two fibers and of the target design as defined in Fig.2.10. Please notice that D and d/D are evaluated from the microscope images, while t is fitted to match the minimum loss wavelength between the simulation and the loss measurement. In the case of AR-Fiber2 the smaller tube outer diameter d_1 is also measured, while its thickness t_1 is calculated by the following equation:

$$t_1 = \frac{d_1 - \sqrt{(d-2t)^2 + d_1^2 - d^2}}{2} \tag{3.1}$$

assuming the glass area conservation and hence that all the tubes have the same glass area.

Both fibers does not meet the requirements set by the target design it is hence to be expected that both do not suppress the TM_{01}, TE_{01}, and HE_{21}core modes. On the other hand because they are close to the desired condition of $d/D = 0.7$ bend induced suppression of HOMs is possible and as I will discuss it is easier to achieve with AR-Fiber2.

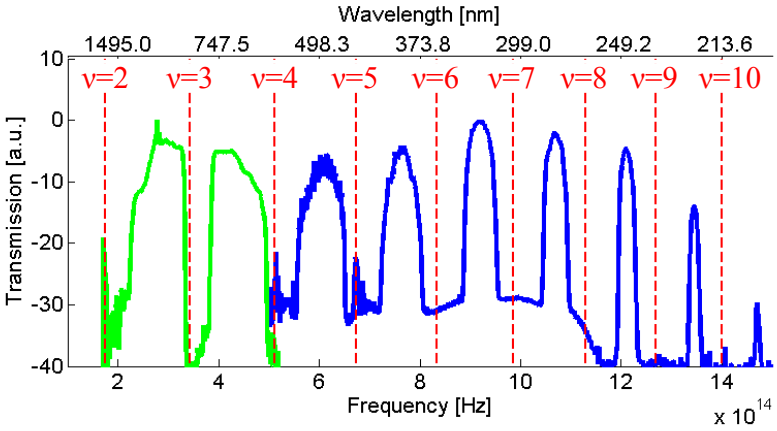

Figure 3.2: Fiber normalized transmission. The green part of the spectrum was obtained with a supercontinuum source and a optical spectrum analyzer. The blue part was measured with a deuterium lamp and Ocean Optics, Maya2000 pro UV spectrometer . The dashed red lines are the frequencies as calculated with Eq.2.11 with ν from 2 to 10.

3.1 AR-Fiber1

A description of the optical properties of AR-Fiber1 was done in [64], and it is here presented with some extensions and a more thorough comparison with the numerical simulation. Figure 3.2 shows the fiber transmission from 200nm to 1500nm. Despite the fiber is designed to offer the best performance in terms of bend robustness and suppression of HOMs in the second transmission band, many other bands at higher frequencies offer core guidance. The red dashed line are the cutoff wavelengths calculated with Eq.2.11 and t=0.83µm . Because of the huge wavelength range it was necessary to account for the material dispersion by using the Sellmeier equation for fused silica. The agreement between the simple 1D analytical model in determining the cutoff wavelengths of the dielectric modes in the tubes and the transmission measurement in Fig.3.2 is excellent. The frequency bandwidth of the transmission bands at high frequencies is smaller. This is likely due to bend induce loss that is much higher at shorter wavelengths.

The simulation was performed in a half domain, with a constant silica glass refractive index of 1.45. Figure 3.3 shows the fiber facet, a near field at 1064nm and a comparison between the measured loss (blue line) and the

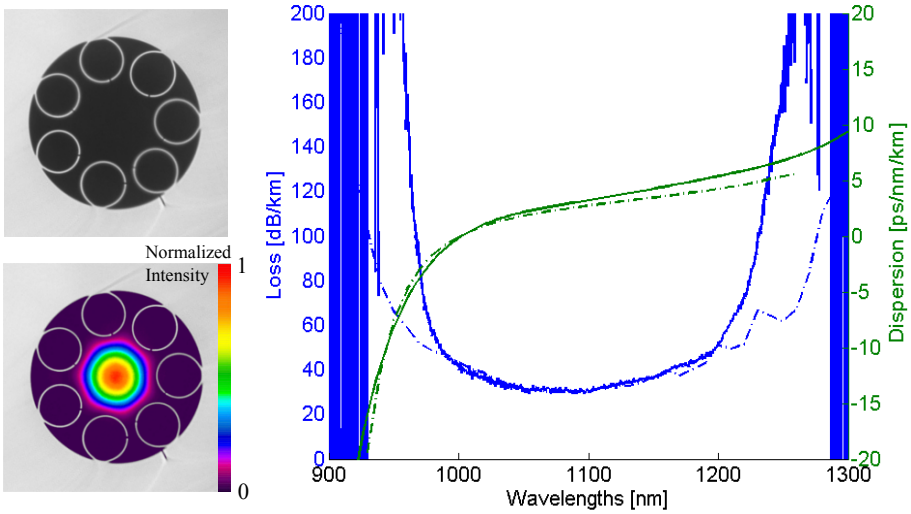

Figure 3.3: Left: Microscope image of the fiber structure and measured near field profile at 1064nm, Right: Measured loss (blue curves) and dispersion (green curves) as continuous lines, calculated confinement loss and dispersion as dashed lines.

simulated confinement loss (dashed blue line), as well as between the measured dispersion (green line) and the simulated dispersion (green dashed line). The dispersion was measured as described in Section 7.3. The loss was measured as described in Section 7.2 with L1+L2= 115m and L1=50m, with the fiber spooled with a 32cm diameter to minimize bend induced loss. The spectra were recorded with 1nm resolution. There is good agreement between the numerical simulation and the properties of the actual fiber, demonstrating that the loss of this fiber is limited by confinement loss. This loss level is such that only few percentage of the light is lost over short distances, making the fiber a suitable candidate for beam delivery. We believe that the discrepancy at the transmission edges are due to the fluctuations in size of the tubes, that therefore have slightly different wall thicknesses. The narrower bandwidth, as expected, affects as well the fiber dispersion. The fiber has minimum loss of 30dB/km at 1090nm, a 50dB/km bandwidth of 213nm and a 100 dB/km bandwidth of 266nm. Dispersion is anomalous over almost the entire transmission band and ultra-low (<10ps/nm/km). This loss figure is among the lowest ever measured around $1\mu m$ for this kind of fiber (lowest we are aware of is 26dB/km at 1041nm for a $32\mu m$ core

fiber [66])

Figure 3.4 shows the simulated mode effective indices and confinement loss. The vertical dashed black line is the cutoff wavelength calculated with Eq.2.11 and $\nu = 2.$, and as expected it matches the cutoff wavelength of the dielectric modes in the simulation. The fluctuations at long wavelengths in the loss are due to the interactions of core modes with dielectric modes. The ratio d/D in this fiber is such to match the dispersion of the cladding HE_{11} modes to the EH_{11} - HE_{21} modes (corresponding to linearly polarized modes LP_{21}). A small index separation is also present between the HE_{12} and the cladding HE_{11} modes. The lowest loss HOMs are the TE01 - HE21 modes (corresponding to linearly polarized modes LP_{11}) followed by the EH_{21} - HE_{41} modes (corresponding to linearly polarized modes LP_{31}). As I will show in the following these are the modes that can be observed in the realized fiber.

Higher order modes

In order to characterize the modal content of AR-Fiber1 we measured the near field profile upon transverse misalignment of the input beam in a 1m fiber under test (FUT) at 1064nm. Figure 3.5 clearly shows the presence of the LP_{11}-like modes as well as LP_{31}-like modes. The same measurements but having two coils with 3cm bending radius resulted in a strong bend induced suppression of the HOMs (Fig.3.5).

A closer look at the LP_{31}-like modes, excited by strong input misalignment, revealed a rather distorted mode compared to the expected intensity profile of a LP_{31}. A comparison between the measured near field profile and its numerical counterpart in Fig.3.6 shows remarkable agreement and suggests that the distortion is induced by the fiber symmetry.

To prove that the fiber resonantly couples HE_{31} and EH_{11} to cladding HE_{11} modes we have measured the near field profile of an ~ 8 cm FUT where instead of coupling the input beam to the fiber core we coupled it to one of the cladding tubes. If any coupling occurs between cladding and core modes then we would expect to observe some light in the core at the output. The measurement were done with a 1064nm laser and polarizers at both the input and output of the fiber. The output near field profiles in Fig.3.6 show an LP_{21}-like mode and an LP_{02}-like mode, suggesting that not only the HE_{31} and EH_{11} are coupled to cladding modes but also HE_{12} modes. The corresponding simulated modes are also presented in Fig.3.6, showing once again remarkable agreement between the numerically calculated and

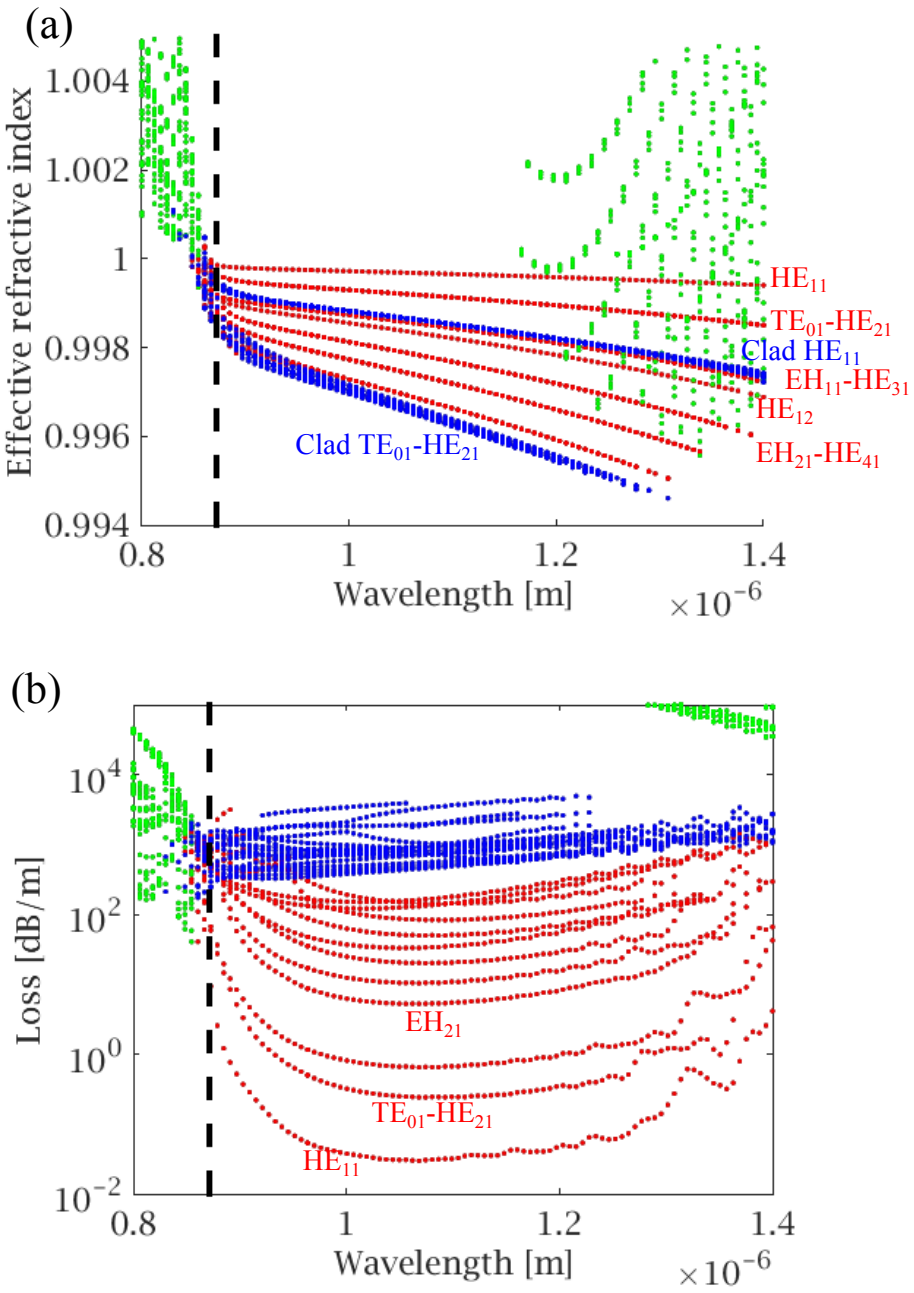

Figure 3.4: The green dots correspond to dielectric tube modes, red dots are core modes and blue dots are air-like modes in the tubes. The simulation was done in half domain with perfect electrical conductor boundary condition. The solutions found with perfect magnetic conductor boundary condition are nearly degenerate to watch shown here and are hence omitted for clarity.(a) Simulated effective refractive indices. (b) Simulated confinement loss

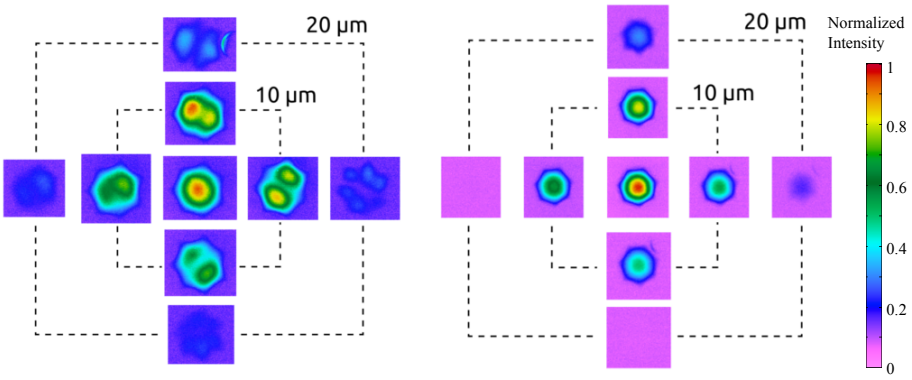

Figure 3.5: Measured near-field output beam profiles versus misalignment of input beam for a straight (left) and coiled (right) 7-tube AR-HC fiber, showing bend-induced suppression of HOMs. Bending was performed with 2 coils with 3 cm bend radius. FUT is 1 meter long

the fabricated fiber mode properties.

Bending properties

One of the downsides of the single layer of confinement in an AR-HC fiber is a relatively large bend induced loss if compared to PBG-HC fibers. To characterize the fiber bend loss we used a custom automated set up. A light beam from a supercontinuum light source is coupled to the fiber and at different bend radii the output spectrum or the near field profile is detected with an optical spectrum analyzer or a camera, respectively. The relative changes in the measured spectra permit to estimate the spectral bend induced loss. The measurement was done with three coils, starting from a bend radius of 12cm and down to the minimum allowed by the set up: 3cm. The measured near field profile in Fig.3.7 were measured at 1064nm by inserting a 10nm bandwidth filter. A significant change in the output profile is visible only at the lowest bend radius and the stability of the beam profile is remarkable. The spectral measure of the bend loss in Fig.3.7 shows a clear trend: negligible bend loss is present down to 5cm bend radius, at smaller radii the short wavelength edge of the transmission band is highly effected and shifts towards longer wavelengths. Finally a comparison between measured bend loss and the numerically simulated one as a function of the bend radius is presented in Fig.3.7 for two selected wavelengths. There is a fairly good agreement between the two at small bend radii. We believe

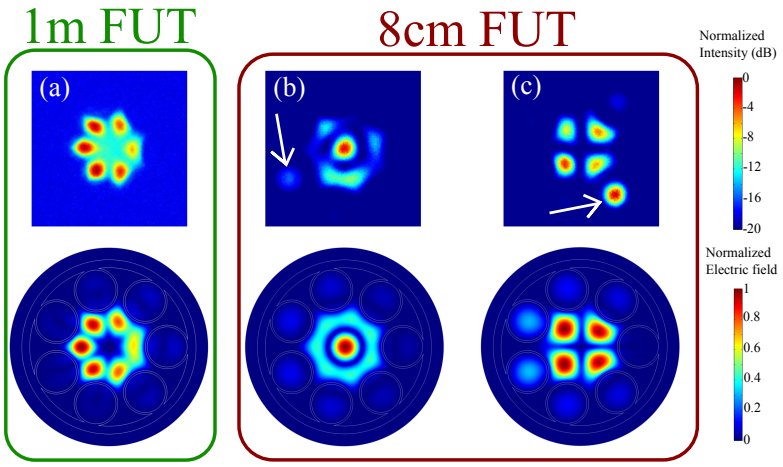

Figure 3.6: Green box: Comparison between the measured near field output profile for a 1 m fiber with ~20μm misalignment of the input beam, showing a LP_{31}-like mode (top) and the corresponding simulated amplitude of the electric field (bottom) for a 1m fiber. Red box: On the top part, measured near field profile in 8cm FUT, coupling input beam to one of the cladding tube. In the bottom part the corresponding simulated amplitude of the electric field. (b) LP_{02}-like mode, (c) LP_{21}-like mode. The white arrows point at the excited cladding tube

that the discrepancy at larger bend radii is mainly due to the measurement uncertainty at low bend losses (<0.5 dB/m). The fiber has a bend-induced loss at 1032nm of ~0.5dB/m and <0.5dB/m at 1064nm for 3cm bending radius, performing significantly better than previously reported in kagome HC fibers [67] and other AR-HC fibers [20] around these wavelengths.

Mode quality

We measured mode quality factor of the fabricated fiber with a camera-based M^2 measurement system (Spiricon M^2-200s) with a laser at a wavelength of 1064nm and a 5m FUT. We performed two measurements: with the fiber coiled on a standard 8 cm spool and no further coils, and with the fiber coiled on a standard 8 cm spool and with an extra two coils with 3cm radius to suppress HOM. The results are summarized in Table 3.2. The fiber output beam presents negligible astigmatism and asymmetry and a M^2 of 1.5. The extra small coils induce suppression of the HOM and the M^2 is consequently improved to 1.2.

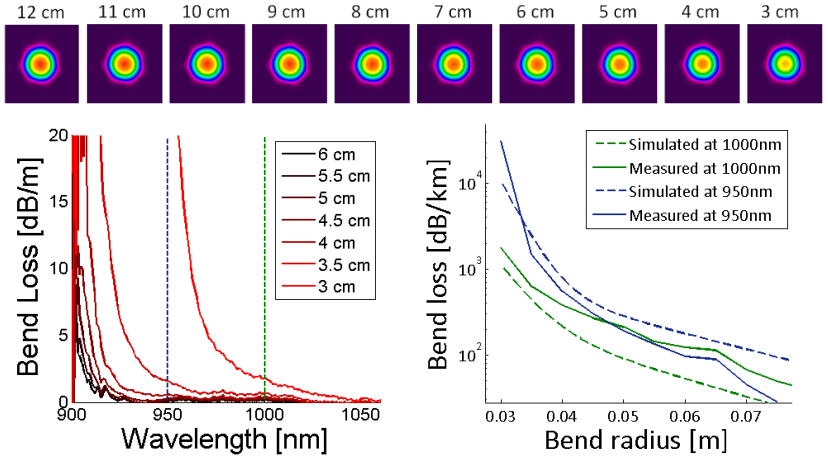

Figure 3.7: Top: Near field profile of the fiber at different bending radii at 1064nm. The fiber had three coils; Bottom left: Induced bend loss measured at different bending radii. The measurements across the blue and green dashed lines are plotted on the right; Bottom right: Comparison between the measured and simulated bend induced loss at two different wavelengths

Table 3.2: Measured M^2, astigmatism and asymmetry

	M^2	Astigmatism	Asymmetry
No extra coils	1.5	0.01	1.02
2 coils, 3cm radius	1.2	0.00	1.07

3.2 AR-Fiber2

AR-Fiber2 has a larger ratio d/D compared to fiber AR-Fiber1 along with a smaller core of approximately 25µm. Moreover one of the tube is significantly smaller than the other as it can be seen in Fig.3.8. In this section I will discuss the main optical properties of AR-Fiber2, comparing it with AR-Fiber1. Figure 3.8 shows the measured and simulated loss. The loss was measured as described in Section 7.2 with L1+L2= 290m and L1=190m, with the fiber spooled with a 32cm diameter to exclude bend induced loss. The spectra were recorded with 1nm resolution. Surprisingly the fiber has a slightly lower loss that its numerical counterpart, with a minimum loss at 978nm of 39dB/km. The 50dB/km bandwidth is 113dB/km and the 100dB/km bandwidth is 185nm. The drastic reduction in bandwidth, com-

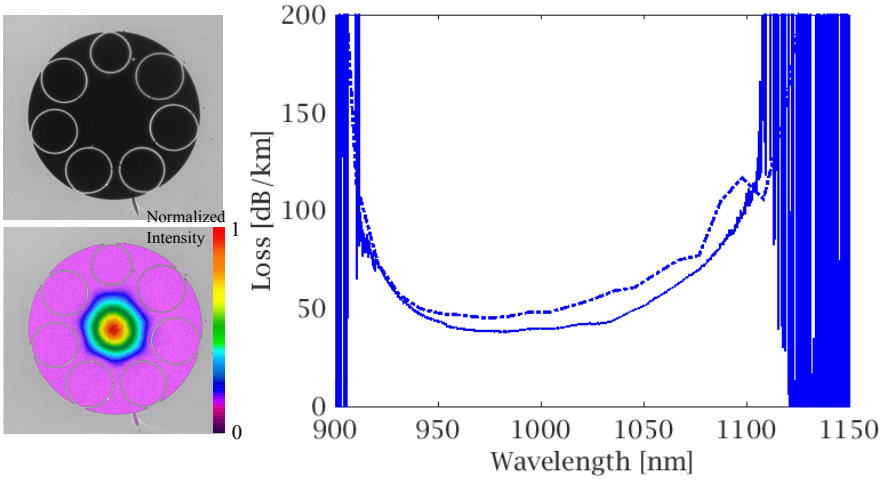

Figure 3.8: Left: Microscope image of the fiber structure and measured near field profile at 1064nm, Right: Measured loss as continuous blue line, calculated confinement loss as dashed blue line.

pared to AR-Fiber1, is entirely due to the presence of the smaller and thicker tube.

Figure 3.9 shows the effective refractive indices of several modes and theirs confinement loss. There are several differences if compared to AR-Fiber1. First of all there are two distinct sets of cladding HE_{11} modes: Clad HE^1_{11} related to the identical 6 cladding tubes and Clad HE^2_{11} to the smaller tube, and they possess well distinct dispersion. Clad HE^2_{11} has a dispersion that matches the one of the HE_{31} and EH_{11} core modes. Because the vectorial HE_{31} and EH_{11} modes are nearly degenerate and because of the interaction with the cladding modes these modes found in the model are linearly polarized as depicted in Fig.3.9 and are hence named LP_{21}. Moreover because of the small tube the core is no more symmetrical and a particularly marked birefringence appears between the LP_{11} modes. Also in this case they are found to be linearly polarized in the numerical model. The norm of the electrical field of the two sets of the LP_{11} modes is depicted in Fig.3.9. The lowest loss HOM is the LP_{11} as seen in Fig.3.9(b) with a loss >1dB/km that is an improvement in comparison to AR-Fiber1.

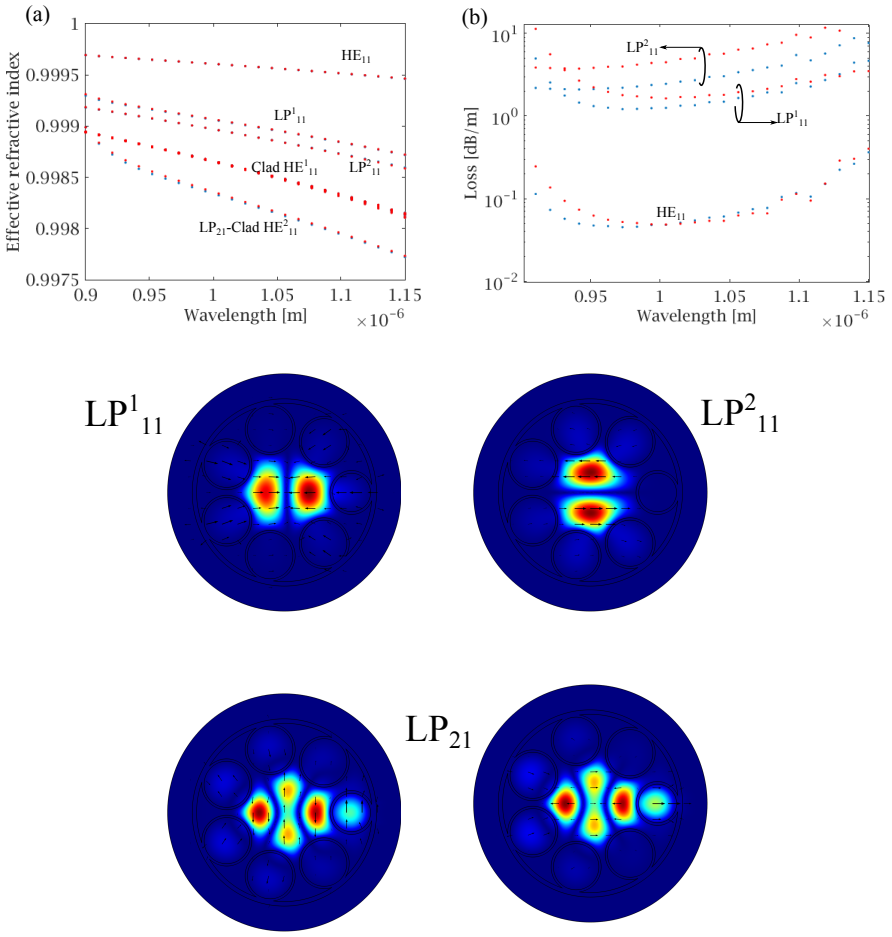

Figure 3.9: (a)Numerical mode effective refractive indices. (b) Corresponding confinement loss. The simulation was done in half domain. Red dots are solutions with perfect electrical conductor boundary condition. Blue dots are solution with perfect magnetic conductor boundary condition. Bottom: Norm of the electric field for the LP_{11} modes and the LP_{21} modes. The arrows represent the transverse electrical field.

Higher order modes

Similarly to what done with AR-FIber1 I measured the near field profile of the fiber upon transverse misalignment of the input beam in a 1m FUT at

1064nm. The result is analogous, but it presents some pecularities. For a straight fiber a LP_{11}-like mode is clearly excited as it can be seen in Fig.3.10, but in this case the misalignment in the vertical and horizontal directions does not produce LP11 modes with nearly orthogonal mode profile as in AR-Fiber1 (see Fig.3.5). It seems that a specifically oriented LP_{11} appears preferentially. This is consistent with the results from the fiber simulation where the LP^1_{11} has a lower loss than the LP^2_{11}. In the lower part of Fig.3.10 the norm of the electric field of the LP^1_{11} and LP^2_{11} are shown. The mode that appears in the measurement with the horizontal misalignment resembles the LP^1_{11} mode. Figure 3.10 shows the norm of the electric field of a linear combination of the normalized field of LP^1_{11} and LP^2_{11}. The resulting profile fits the intensity profile measured during vertical misalignment. This suggests that this behavior of the is due to the the difference in confinement loss between the two LP_{11} modes. Optimal HOMs bend suppression can be achieved in this fiber with a bending radius of 4.5cm. Figure 3.10 shows the measurement performed with a single 4.5cm radius coil. The result is comparable to what achieved in AR-Fiber2 with two 3cm radius coils. The different bending radii are due to the different effective refractive index separation between the cladding HE_{11} modes and the LP_{11}-like modes in the two fibers.

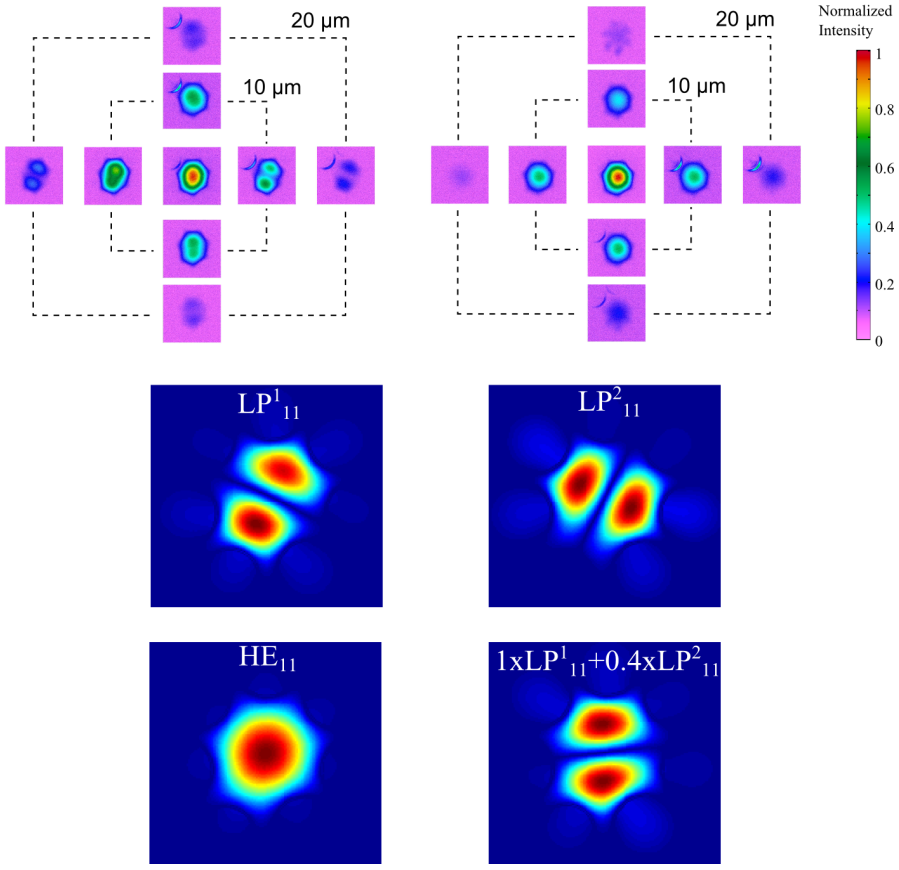

Figure 3.10: Measured near-field output beam profiles versus misalignment of input beam for a straight (left) and coiled (right) 7-tube AR-HC fiber, showing bend-induced suppression of HOMs. Bending was performed with 1 coils with 4.5 cm bend radius. FUT is 1 meter long. The lower figures show the norm of the electric field from the numerical calculation for the two LP_{11}-like modes, a linear combination of the two and the fundamental mode.

Bending properties

I used the same automated set described for AR-Fiber1 in order to characterized the bend induced loss in AR-Fiber2. The measurement in this case was done with 10 coils to increase the measurement accuracy at low bending loss. As before the starting bend radius is 12cm and it was measured down to the minimum allowed by the set up: 3cm. The spectral measure of the bend

loss in Fig.3.11(a) shows that AR-Fiber2 has a even lower bend induced loss (please notice that here the y axis is up to only 5dB/m) as expected since the fiber has a smaller core. The fiber has a bend-induced loss at 1032nm of ~0.25dB/m and ~0.2dB/m at 1064nm for 3cm bending radius. Figure 3.11(b) and (c) show the position stability of the output beam for a static fiber and for the fiber repetitively moved from 12cm bending radius to 5cm bending radius. The relative position of the centroid of the beam was logged regularly over a time of 5 minutes for the two cases. In Fig. 3.11(b) and (c) the relative positions normalized by the beam MFD are depicted. The measurement shows no difference in the two cases with variations smaller than 1% of the MFD. If any bend induced variation of the position of the output beam was achieved it was below the set up sensitivity.

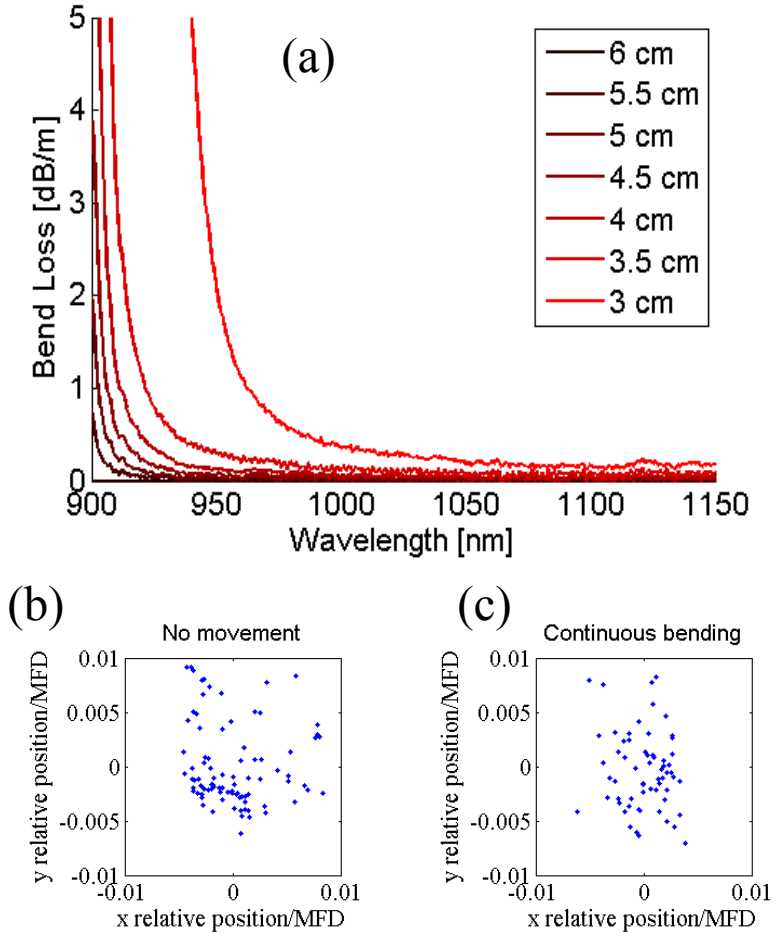

Figure 3.11: (a) Induced bend loss measured at different bending radii. The measurement was done with 10 fiber coils (b) The relative position compared to the MFD is plotted when the fiber is kept still. (c) The relative position compared to the MFD is plotted when the fiber is moved from 12cm to 5cm and back repetitively.

3.3 Conclusions

The fabricated AR-HC fibers show remarkable optical properties. I could prove experimentally the occurrence of HOMs resonant coupling to cladding modes in AR-Fiber1. Despite the straight fibers do not suppress the LP_{11}-like modes it can be obtained through bending to the point that even after only 1m of fiber no HOMs can be seen in the near field when the input light beam is misaligned. The comparison between the numerical model and the fiber characterization measurements shows great agreement, supporting the idea that the target fiber design will show the expected modal properties described in Section 2.3. Finally the robustness of these fibers towards bending demonstrate that they can be exploited in application where tight bending and continuous movements are required, providing an output beam with excellent beam quality and pointing stability. The encouraging numerical results in Section 2.3 and the experimental results shown in this Chapter resolved in a patent application on the 7-tube AR-HC fiber design [68].

Chapter 4

PBG-HC fibers for beam delivery

In this chapter I will describe the optical properties of two PBG-HC fibers that were used in the high power beam delivery in Chapter 6. The light source used in the experiment has a center wavelength of 1032nm. In doing so I will introduce a technique to construct an idealized geometry that closely resembles fabricated 7-cell PBG-HC fibers.

4.1 7-cell PBG-HC fiber: PBG-HC-1

The PBG-HC-1 fiber has a core diameter of 10μm and a mode field diameter of ~7.8μm at 1064nm. Figure 4.1(d) shows a microscope image of the fiber facet. In order to accuratevely describe the modal properties of this fiber I have performed a numerical simulation on closely resemble geometry. As described in Section 2.1 a standard approach to construct the core geometry produce a structure as in Fig.4.1(a) where the core size is fixed to be 3 times the pitch of the regular cladding structure. This clearly differs from the actual fiber structure where not only the core has a different size but some of the holes surrounding the core have a large deviations in size compared to the rest of the cladding holes. To account for these differences I introduced two deformations in the ideal fiber structure. The first ring around the core has 12 holes that consist of 6 hexagonal and 6 pentagonal interchanging holes. To mimic the expanded hexagons and shrunk pentagons in the actual fiber, the parallel edges of the pentagons in the ideal structure are moved closer together, keeping the center. The resulting structure is depicted in Fig.4.1(b). The core size is still 3 times the pitch. In doing this deformation

the glass area in the straight sections of the core wall is kept constant. Finally a radial Gaussian deformation is applied to the entire structure. The amplitude and half width of the Gaussian function used are calculated to obtain the desired core size and location of the second ring of holes surrounding the core. Figure 4.1(c) shows the resulting structure that possess all the main features observed in the actual fiber in Fig. 4.1(d). In Fig. 4.1(e) the norm of the electric field of the fundamental mode from the simulated structure is depicted, showing very good agreement with the measured near field profile of the real fiber in Fig.4.1(f). While accounting for the peculiarities of the realized fiber this approach maintains the symmetries of the original ideal structure, allowing for faster quarter domain simulations.

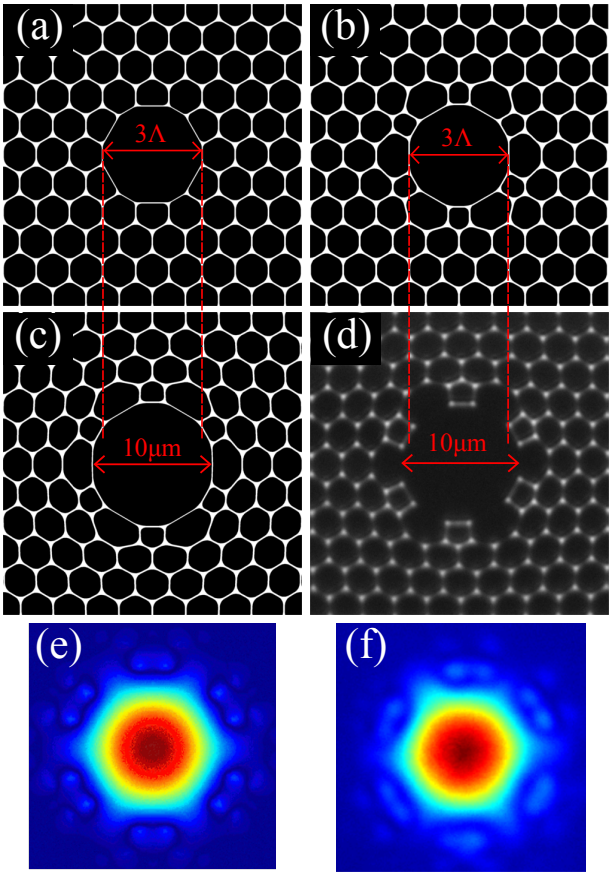

Figure 4.1: (a) Ideal fiber structure. (b) Modified fiber structure with small pentagonal holes in the first ring of holes around the core. (c) Structure in (b) with a radial Gaussian deformation. (d) Microscope image of the fabricated fiber facet. (e) Norm of electric field of the fundamental mode numerically obtained from the geometry in (c). (f) Output beam profile of the fiber in (d) in logarithmic scale

The numerical loss is the sum of the confinement loss and scattering loss (Eq.2.10) and it is shown in Fig.4.2 as a dashed blue line, together with the measured loss as a continuous blue line. The loss was measured as described in Section 7.2, with a length L1+L2=250m and L1=50m. Figure 4.2 also compares the measured and simulated dispersion depicted as continuous and dashed green lines, respectively. The dispersion was measured as described in Section 7.3.

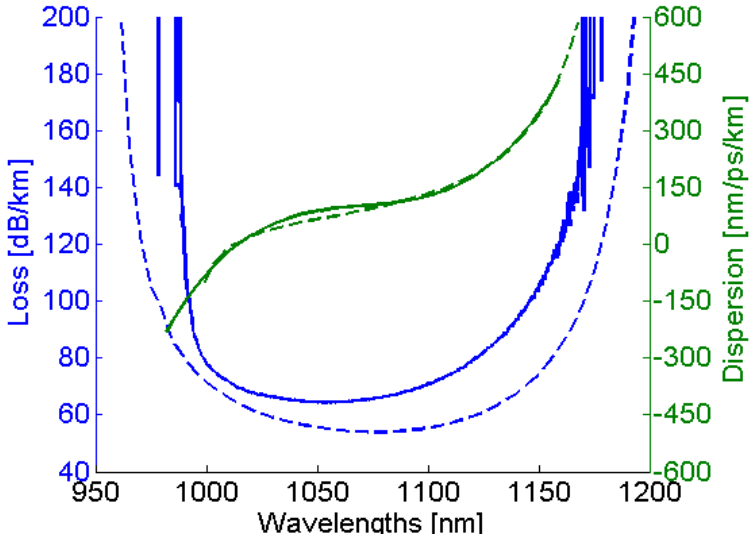

Figure 4.2: PBG-HC-1: Measured loss and dispersion as continuous lines, simulated loss and dispersion as dashed line. The simulated loss is the sum of the confinement loss and scattering loss calculated with Eq.2.10.

In order to characterized the HOMs in this fiber I used the technique described in Section 7.3 to evaluate the group index difference between the fundamental and HOMs. Figure 4.3 (b) shows the spectrogram of the transmission spectrum over a 50cm FUT. By comparing this measurement with the numerically obtained effective refractive indices and losses in Fig.4.3(a) and (b) one can determine that the short wavelength edge of the bandgap is set by a surface mode rather than the cladding modes. The same surface mode is likely responsible for the short wavelength cutoff of the TE_{01} mode.

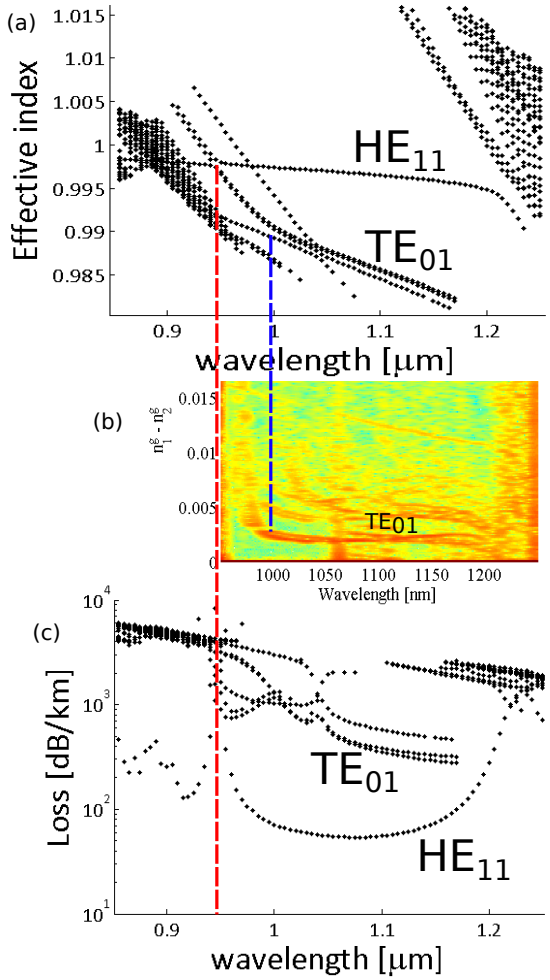

Figure 4.3: (a) Numerical effective refractive indices. (b) Spectrogram of the fiber transmission over 50cm FUT measured as described in Section 7.3. (c) Numerical losses.. The red dashed line shows the wavelength at which the fundamental mode is crossed by a surface mode that determine the short wavelength edge of the bandgap. The blue dashed line show the wavelength at which the TE_{01} mode has a avoided crossing with a surface mode.

4.2 19-cell PBG-HC fiber: PBG-HC-2

In order to reduce the fiber non-linearity in the framework of PGB-HC fibers one should consider larger core fibers. Larger cores are obtained by omitting a higher number of cladding unit cells in order to form the core defect. I will here consider a 19-cell PBG-HC fiber with a core diameter of approximately 18μm and a mode field diameter of about 13μm at 1064 nm. A 19-cell PBG-HC fiber design holds the record low loss of 1.2dB/km at 1620nm [23]. It was possible to achieve such a low loss by introducing an anti-resonant core wall, i.e. the thickness of the core wall is chosen to provide a extra confinement contribution. This reduces the overlap between the core modes and the silica structure minimizing the scattering loss [69]. A drawback in this approach is the increased number of surface modes supported by the core wall that drastically limits the operational bandwidth of the fiber to 10-20 nm [70].

The fiber that I will describe here is designed to achieve low loss by introducing 12 anti-resonant elements on the core wall, rather than having a uniform thicker core, as is can be seen from Fig. 4.4(a). In this manner the detrimental effect of the newly introduced surface modes is reduced and the obtained operational bandwidth is significantly larger.

A typical fiber 1 meter transmission curve is compared to the measured fiber loss in Fig. 4.4(d), showing a 20dB/km and 50dB/km bandwidth of ~30nm and ~50nm, respectively. Minimum loss is 15dB/km at 1058nm. The low loss bandwidth is limited by the surface modes inducing high loss rather than by the photonic bandgap edges as typically occurs in 7-cell PBG-HC fibers.

The near field profile measured at 1032nm and the measured loss of the fiber used in the high power beam delivery experiment in Chapter 6 are in Fig. 4.4(b) and Fig. 4.4(c), respectively. The measured loss shows a high loss peak centered at 1060nm. This is due to an unwanted surface mode. The fiber was nonetheless selected for the beam delivery experiment because it presents the lowest loss at 1032nm among the drawn fibers.

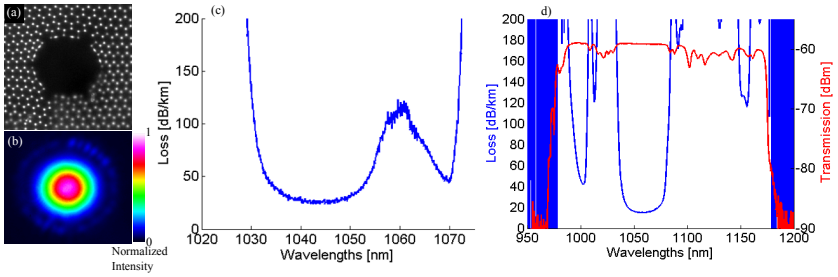

Figure 4.4: PBG-HC-2 : (a) Microscope image of the fabricated fiber (b) Near field profile measured at 1032nm (c) Measured loss of the fiber used in the delivery experiment (d) Typical 1m transmission and measured loss that can be achieved with this fiber design

4.3 Conclusions

Two high quality PBG-HC fibers suitable for the delivery of picosecond pulses at 1032nm were here described. I also introduced an approach to obtain a ideal 7-cell PBG-HC geometry solely from the microscope image of the fiber facet, the drawing parameter and the fiber transmission spectrum. I have shown how this approach is useful to determine the fiber modal properties.

Chapter 5

Polarization properties of hollow core fibers

Hollow core fiber can be designed to be polarization maintaining inducing a difference in the effective indices of the two polarization of the fundamental mode : $B = n_{eff,1} - n_{eff,2}$, i.e. birefringence. As I discussed in section2.1 the core wall geometry has a great impact on the guidance properties of the fiber, and it can be for example designed to induce birefringence. Typically this is achieved with the introduction in the core wall of anti-resonant elements. The idea is to break the fiber symmetry by introducing a two fold arrangement of rods in the core wall [31]. Two orthogonal fiber axes can hence be defined. The two polarization of the fundamental mode will experience a different overlap with the fiber structure leading to a difference in their effective indices. In the picture of these elements being Fabry-Perot like reflecting elements the difference between the two polarization comes from the different reflectance for s- and p- wave as it can be seen in Fig.2.2. Because of the different size of these elements in comparison to the cladding apexes (see Fig.2.8) they also introduce a new set of surface modes. Following this concept PM PBG-HC can be designed to maintain polarization over relatively long distances of the order of 100m [34].

As described in Section 2.1 7-cell PBG-HC fibers can be designed to avoid crossing between surface modes and the fundamental mode. Despite of this surface modes with higher effective index than the fundamental mode can still be present with relatively low loss. This is detrimental in several applications where a single optical mode is required. In section 5.1 I will describe the main properties of a PM fiber geometry that has a modified cladding structure. The introduction of cladding defects can lead to the

suppression of some of the low loss surface modes and hence enhance the beam quality of the output fiber beam. At the same time the proposed fiber structure shows lower polarization cross talk than state of the art PM PBG-HC fibers. The analysis regarding this fiber design was published in [71].

In the perspective of beam delivery, where much shorted length are typically needed, the requirements in the fiber birefringence are less stringent to maintain the polarization. In this regard I will show in section 5.2 that even a fiber that is not specifically designed to be PM can hold the polarization over a short distance. This lead to the question of how much phase birefringence is sufficient in a HC fiber to achieve acceptable polarization maintenance over a short fiber distance. Some of the characterization of the polarization properties of this 7-cell PBG-HC fiber were published in [64].

Finally in the last section of this chapter I will describe the polarization properties of AR-HC fibers. These fibers have typically a very small birefringence due to extremely low overlap between the light field and the silica structure, even in presence of slightly elliptical cores.

5.1 7-cell PBG-HC with cladding defects

In order to achieve a PM PBG-HC fiber with high birefringence and at the same time limit the amount of surface modes within the fiber transmission band one can introduce in the cladding a number of defects with the aim of resonantly couple low loss surface modes to high loss defect modes in the cladding. Figure 5.1 show 4 PBG-HC fibers that has a 4 anti-resonant core wall elements to make the fiber PM and at the same time 6 partly collapsed holes in the cladding lying in a straight line, 3 on each side of the core. The fibers were fabricated using the stack and draw technique and they were drawn from the same preform. The capillaries that correspond to the cladding defects have pressure control independent from the rest of the cladding, which allow to introduce a pressure difference during drawing that was used to produce the cladding defects in a controlled way. The collapse of the cladding holes is different for the four fibers. If we define the collapse ratio α as the ratio between the diameter of the hole in the defect and the unaltered average cladding hole diameter the four fibers have the following collapse ratios $\alpha_I = 60\%$, $\alpha_{II} = 55\%$, $\alpha_{III} = 46\%$, $\alpha_{IV} = 37\%$. The fibers have approximately the same core size, pitch and cladding structure. Because of the lower pressure in the direction of the defects the core becomes elliptical.

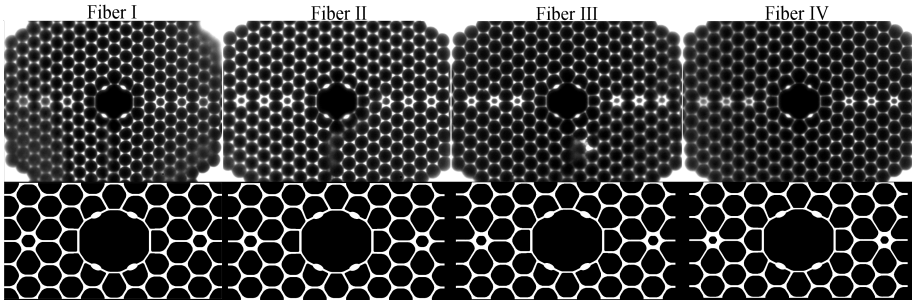

Figure 5.1: Top:Microscope images of the fibers considered. Bottom: Corresponding idealized structures used in the modeling.

I realized an ideal geometrical structure in order to simulate the modal properties of these fibers, as shown in Fig. 5.1. The geometry reproduces of the major features of these fibers. Starting from a realistic fiber structure known in literature [26,72], I accounted for the elliptical core, the anti-resonant core wall elements and the cladding defect. With respect to the cladding defect I assumed the glass area of the fiber is a conserved quantity and no glass flow between apex and strut or between different unit cells. The local area conservation in each unit cell, strut and apex has been proven to be a good approach in previous publications [73,74]. The four fiber geometry have the same pitch of 3.2 μm, the same thickness of the strut of 180nm and the same core size with an aspect ratio of about 1.2.

A first set of simulations were done with four rings of holes surrounding the core with a single defect per core side to analyze the effect of the collapse ratio over the fiber modal properties.

For Fiber III, that shows the best performance, the simulation was extended to six and eight rings of holes, i.e. two and three defects per core side, respectively.

Surface mode stripping

The scheme in Fig.5.2 summarizes the principle that is exploited to strip the surfaces modes. Three types of modes are relevant for this analysis: a surface mode in green, the fundamental mode in red and the defect mode in blue. By tuning the collapse ratio of the cladding defects it is possible to couple the modes localized on the defect to surface modes at wavelengths where the fundamental mode is unaffected. As a trade-off at longer wavelengths the defect mode couples to the fundamental mode limiting the fiber bandwidth.

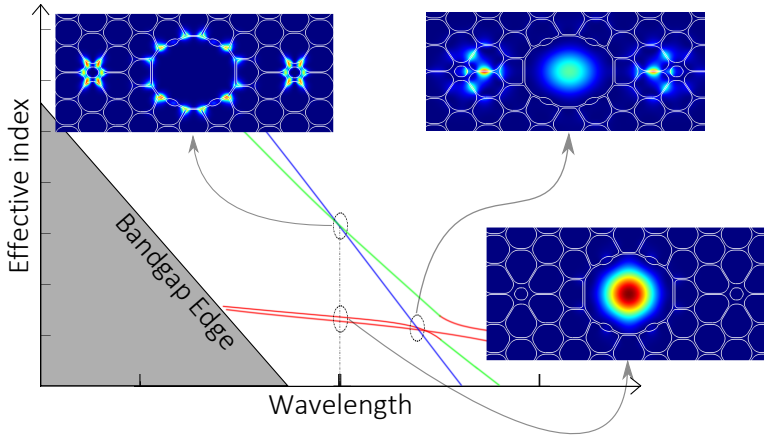

Figure 5.2: Sketch of the surface mode stripping. The green line represents an unwanted surface mode, the red lines the two polarization of the fundamental mode and the blue line is the cladding defect mode that can be used to attenuate the surface modes

The same color scheme is used in Fig.5.3 to identify the different modes. Comparing the three fibers it is clear that there is no difference in the dispersion curves of the surface modes and the fundamental modes, as expected since core size, core wall and the regular cladding are identical. Fiber I shows a set of defect modes that correspond to apex-like modes in the defect. Because a smaller collapse ratio correspond to a larger glass areas in the cladding defects this set of defect modes shifts to shorter wavelengths. In Fiber III and IV a second set of defect mode appears at short wavelengths. This is due to the different size of the struts connecting the defect to the rest of the cladding. Due to the condition in the model of local conservation of the glass area these struts are thinner for smaller collapse ratios. Therefore the modes localized on them shift towards longer wavelengths for smaller collapse ratios, see Fiber III and Fiber IV in Fig.5.3. Consequently the defect modes can be controlled during the fiber drawing. The transmission measurements for the 4 fibers in Fig.5.3 shows good agreement with the simulated mode trajectories, showing a reduction of the operational bandwidth around 1550nm for smaller collapse ratios. The mismatch at longer wavelengths for Fiber III and Fiber IV is likely due to the fact that the simulation are here performed for only one defect per core side.

The simulations are extended for two defects and three defects per core side for Fiber III. Figure 5.4 shows how the presence of several neighbor defects

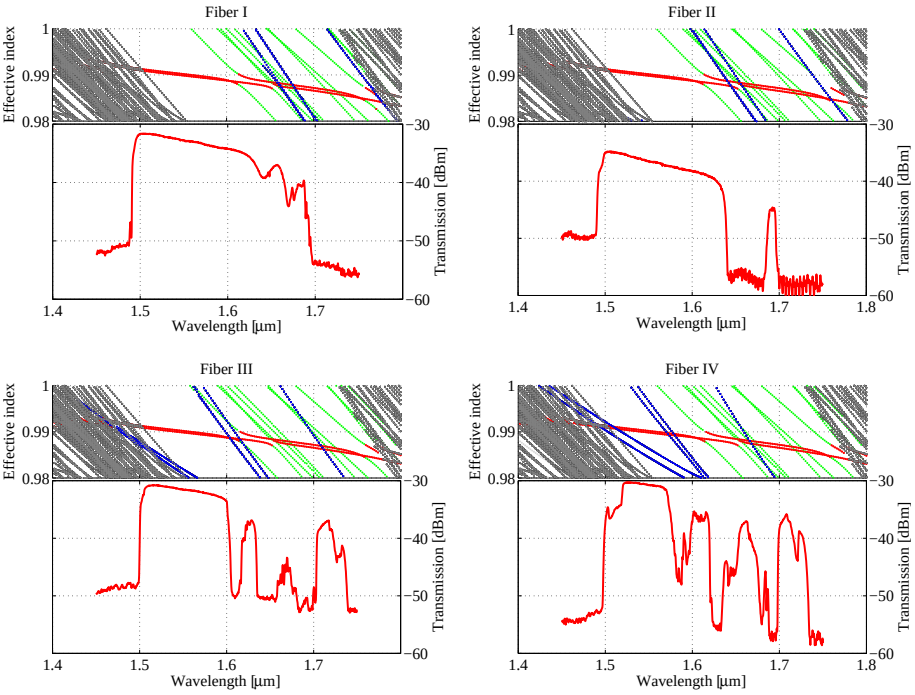

Figure 5.3: For the four fibers the simulations from the idealized model (upper part of each quadrant) and the measured transmissions (bottom part of each quadrant) are compared. In the mode trajectory plots green dots represent surface modes, red dots the fundamental modes, blue dots the cladding defect modes and dark grey the cladding modes

leads to the establishment of supermodes, populating the transmission band with several others defects modes. This increases the interaction between cladding defect modes and surface modes within the bandgap. In order to quantify this I estimated through an overlap integral the coupling between all the surface modes and all the defect modes. Since these modes have a considerable field amplitude at the glass/air interfaces, scattering from glass surface roughness can be considered as a primary contribution to the coupling. For this reason, similarly to what is typically done to estimate scattering loss for the fundamental mode [23], the following overlap integral were used as coupling coefficient:

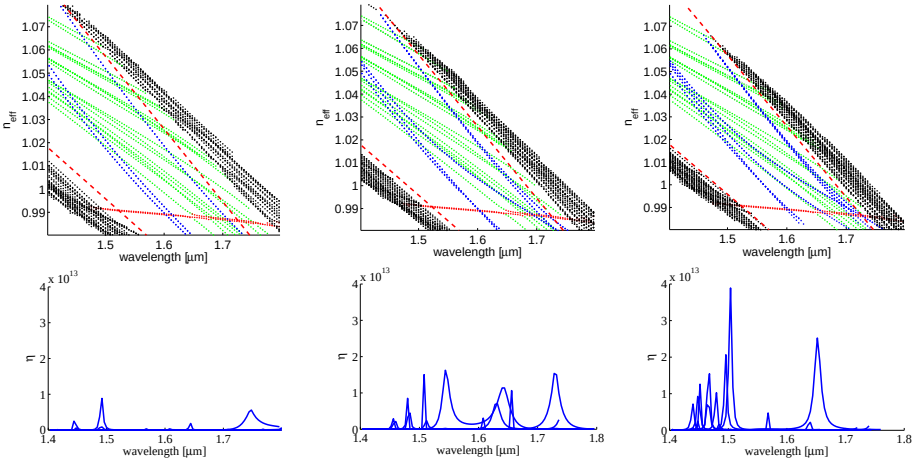

Figure 5.4: The simulated mode trajectories for fiber III and the overlap integrals between surface modes and cladding defect modes are plotted in the case of 4, 6 and 8 rings of holes, respectively. Green dots represent surface modes, red dots the fundamental modes, blue dots the cladding defect modes and black dots the cladding modes. The red dashed lines represent the bandgap edges for the simulation in the case of an infinite photonic crystal

$$\eta = \frac{\left| \oint_{\text{glass/air interfaces}} \mathrm{E}_1^* \cdot \mathrm{E}_2 \, \mathrm{d}l \right|^2}{\int \mathrm{E}_1^* \cdot \mathrm{E}_1 \, \mathrm{d}A \int \mathrm{E}_2^* \cdot \mathrm{E}_2 \, \mathrm{d}A} \tag{5.1}$$

The simulations were performed in a quarter domain for all the four boundary conditions, therefore η was evaluated only between modes calculated with the same boundary conditions, since otherwise it would automatically be zero for symmetry reasons. In Fig.5.4 the calculated coupling coefficients are plotted. We notice that despite the high number of crossings that are occurring only a few are relevant. Moreover since the dispersion curves of the cladding defect modes and surface modes are so similar, tiny differences in their relative location can drastically change the coupling between them, as it is evident comparing the six and eight rings cases. We also expect that more couplings than the ones predicted by the numerical model are present because of geometrical deformations along the fiber.

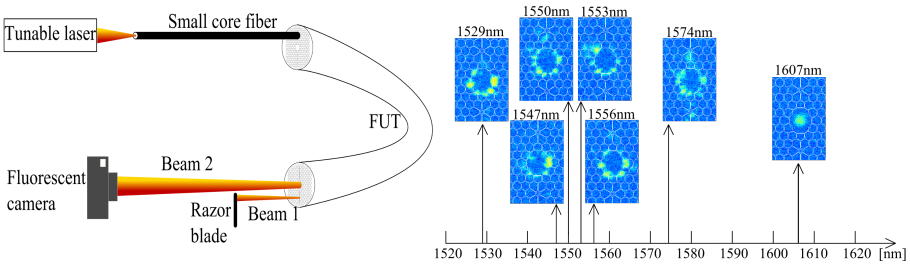

Figure 5.5: Left: Schematic of the measurement. Right: Obtained optical intensity profiles

To prove the occurrence of the coupling between surface modes and defect modes I coupled the light from a tunable laser by butt-coupling via a small core (~3µm) fiber directly to one of the cladding defects. At the output a razor blade is used to dump the residual light guided by the defect and the core area of the fiber is imaged on a infrared Vidicon camera C2741. A scheme of the measurement is in Fig.5.5. The signal on the camera was very week, but by tuning the laser wavelengths we could clearly observed light in the surface modes in proximity of 1550nm and at longer wavelengths the fundamental core modes. This measurement strongly indicates that there is a coupling between defect and surface modes. Moreover as expected by the numerical analysis done so far at 1607nm was possible to observe the coupling between the fundamental and defect mode. This also match with the transmission dip in the measurement in Fig.5.3 for Fiber III.

Polarization Maintenance

Thanks to the joint presence of birefringent elements on the core wall and the elliptical core we obtained a fiber with low loss (~60dB/km at 1550nm) and good polarization maintenance, as shown in the following.

The group modal birefringence (GMB) was measured for Fiber III as described in 7.3. Two different fiber lengths, 1.3m for the short wavelengths and 19.4m for the long wavelengths, to have a good resolution for the whole measurement range. In Fig.5.6 two simulations of the numerical model performed with slightly different core wall thickness are compared to the experimental measurement, showing a fairly good agreement.

The fiber h-parameter was measured for a 50m FUT as described in chapter 7.4 and it is shown in Fig.5.6. A flat profile with a value of about $5{\times}10^{-5}m^{-1}$ around 1550nm was measured. This is at least a factor of two lower than

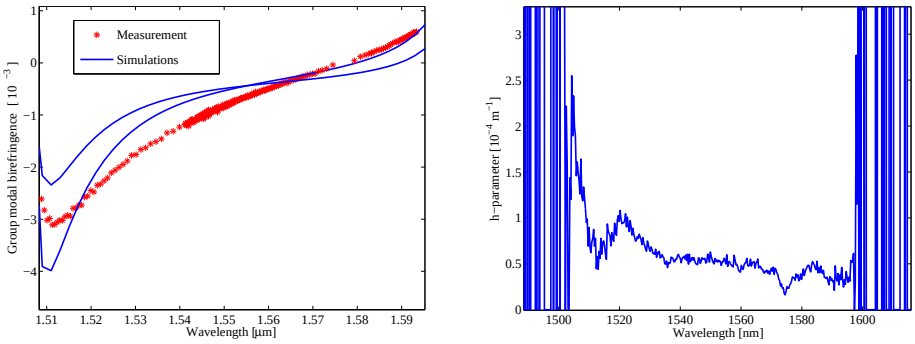

Figure 5.6: Left: Measured group modal birefringence with scanning wavelength method is compared to the idealized model simulation. Right: Measured polarization holding parameter (h-parameter)

state of the art fibers without cladding defects [34]. If in a given application a maximum of -20dB polarization crosstalk can be tolerated, at best 100m of a hollow core fiber without cladding defect can be exploited, while up to 200m can be used in case of Fiber III.

5.2 PM properties of 7-cell PBG-HC-1

For a given polarization extinction ratio (PER) requirement, the shorter the fiber the larger h-parameter can be tolerated. Consequently the birefringence can be lower. In this section I will consider the 7-cell PBG-HC-1 fiber described in Chapter 4. The slight elliptical core induces a small birefringence that is sufficient to maintain polarization over 5 meters of fiber. In order to quantify the robustness of this fiber in maintaining and delivering linearly polarized light I measured the PER of the fiber output signal for a unperturbed coiled fiber and with the fiber subjected to bend and twist. The measure was performed as described in chapter 7.4 and the results are summarized in Fig.5.7. The fiber not only maintains and deliver linearly polarized light with a PER >15dB but is surprisingly resistant towards bending. The fiber is more sensitive to twist but the measurement was done with a significant amount of twist that can easily be avoided in most practical situations.

It is therefore interesting to evaluate the fiber phase birefringence $B = \Delta n_{eff}$, i.e. the difference in the effective index of the two polarization of the fundamental mode. The aim is to quantify how much birefringence is needed to maintain polarization with a PER>15 over 5m. To measure the fiber bire-

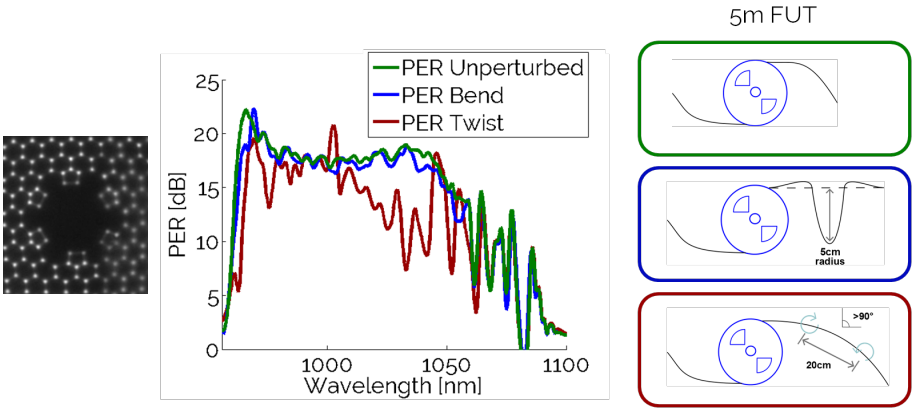

Figure 5.7: Left: Fiber structure. Center: Measured PER for the unperturbed fiber and with bend and twist. The measurement was done with the set up in Section 7.4

fringence a typical approach [75] in solid core birefringent fibers is to launch linearly polarized light with the polarization direction aligned to one of the fiber axis and to induce a coupling between the two polarization along the fiber by applying a point like pressure. The collected spectra shows spectral interference and the variations on the position of the maxima in the as the point-like pressure point is moved along the fiber allow to quantify the phase birefringence. This approach fails in the case of PBG-HC fibers because the coupling between the two polarization can not be obtained by applying a point-like pressure. To overcome this I launched the light with the polarization direction at 45º and varied the fiber length by cleaving small sections of the output end of the fiber, maintaining unaltered coupling conditions. At each fiber length a spectrum is collected with an OSA. Notice that in this measure the spatial resolution needed depends on the polarization beat length $L_b = \lambda/\Delta n_{eff}$. This fiber have low birefringence and therefore relatively long beat length. The position of each maximum is indexed as shown in Fig.5.8 and the position as a function of the total length of the removed fiber. The shift of the maxima is such that $\lambda_n(L) = \lambda_{n+1}(L - L_b)$ as illustrated in Fig.5.8 and it is hence possible to evaluate the phase birefringence.

Figure 5.9(a) shows the measured phase birefringence around a wavelength of 1030nm. The measurement was done with the set up described in Section 7.4. The FUT was 25m long, the total cut back was 9.5cm and it was done cleaving 0.5cm sections at the time. After each cleaving a spectrum was

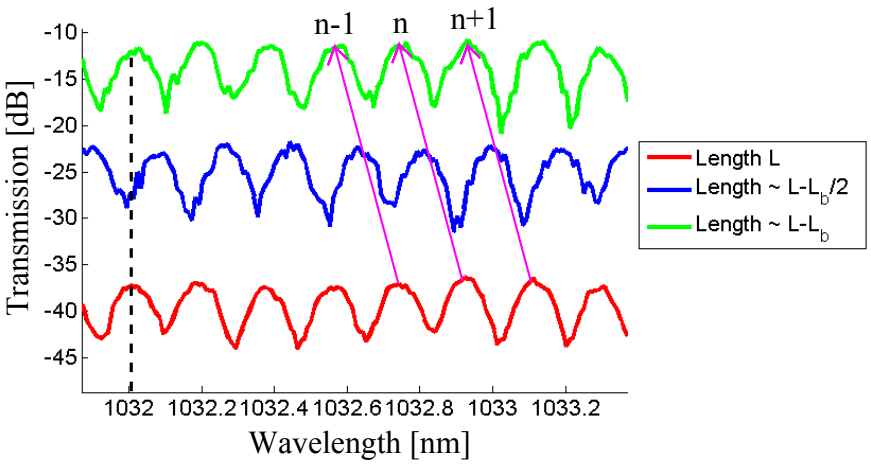

Figure 5.8: Measured spectra for a fiber of length L and for a fiber shorten by ~$L_b/2$ and ~L_b. The spectra are shifted by 10dB to improve visibility.

collected. A phase birefringence of ~1.3×10^{-5} was measured at 1030nm with a slope of $-2.16 \times 10^{2} nm^{-1}$. In order to make a consistency test in fig.5.9(b) I compare the measured GMB with the GMB calculated from the phase birefrincence by the following equation:

$$GMB = B_{phase}(\lambda) - \lambda \frac{dB_{phase}(\lambda)}{d\lambda} \tag{5.2}$$

The two are indipendent mesaures of the same quantity and there is a good agreement between the two. Moreover by integrating the GMB and knowing $B_{phase}(1030nm)$ one can derive the B_{phase} over the whole fiber transmission band as depicted in Fig.5.9(c). By this analysis I can hence estimate that a phase birefringence of the order of $1 \times 10^{-5} \div 2.5 \times 10^{-5}$ is sufficient for a HC fiber to maintain linearly polarized light over 5m with a PER>15dB.

5.3 PM properties of AR-Fiber1

As discussed in Section 2.3 AR-HC fibers typically have large cores and very low overlap between the light field and the silica structure. For these reasons these fibers are expected to show no polarization maintaining properties. I will here consider AR- Fiber1, described in Chapter 3.

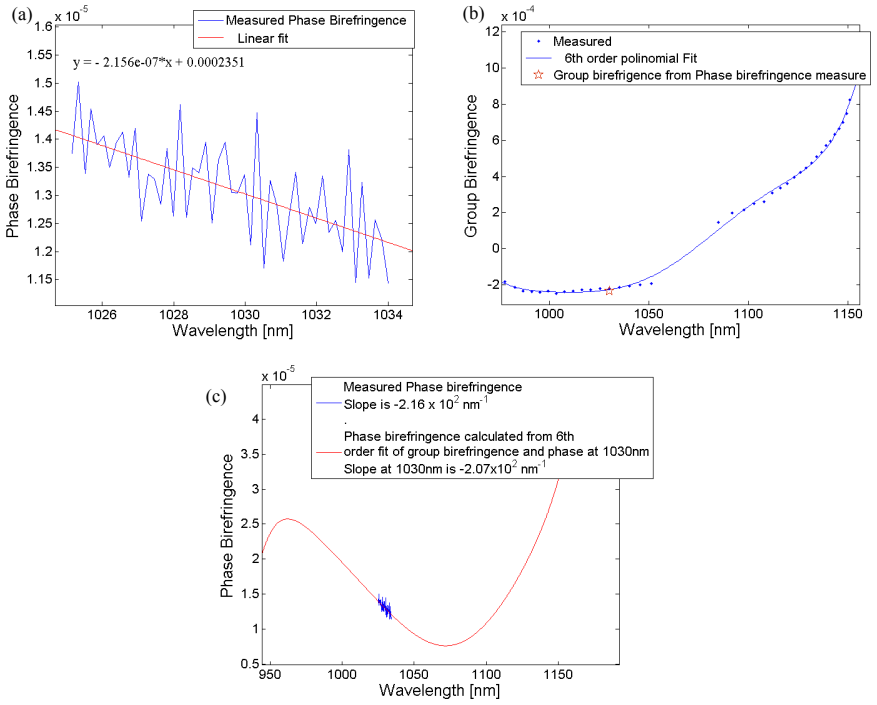

Figure 5.9: (a) Measured phase birefringence. (b) Measured group modal birefringence as described in Section7.4. The star represent the GMB calculated from the phase birefringence measurement. (c) The phase birefringence calculated from integrating the group birefringence and the value of the phase birefringence at 1030nm.

I measured the PER for the AR-HC fiber with the set up in Section 7.4, using a laser at 1064nm and 5m FUT. The result in Fig.5.10(left) is quite surprising, showing a PER in excess of 30dB. In contrast to the PBG-HC fiber in the previous section the fiber showed very high sensitivity to external perturbation. In light of this result I repeated the measure using a supercontinuum light source. Differently from what expected by a polarization maintaining fiber the output fiber spectrum always showed spectral interference as depicted in Fig.5.10(right), regardless of the direction of the polarization of the input light signal. This indicates that the fiber is not maintaining the polarization state even when the input light polarization is optimally coupled to one fundamental mode polarization. The particular position of the fiber determines the cross talk between the two polarization of the fundamen-

tal mode. Because of the very low birefringence at 1064nm one can find a coupling condition such that the output beam is linearly polarized. This condition though highly depends on the fiber length and position, meaning that any movement of the fiber will affect the output polarization state. In other words even though the state of polarization is not maintained along the fiber, it can still provide a linearly polarized output at certain wavelengths by optimizing the input polarization angle.

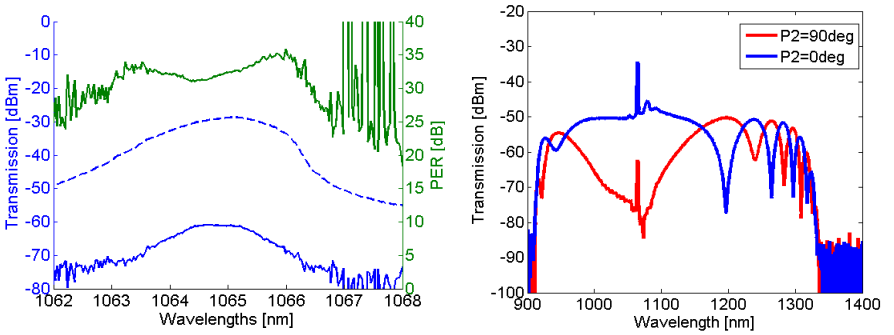

Figure 5.10: Left: In green the PER measured with a 1064nm laser and a 5m FUT. The blue dashed line is the trasnmission with the output polarizer rotated to allow the maximum power through. The continuos blue line is the trasmission with the output polarizer rotated by 90 degree. Right: Typical transmission curves from the PER set up (Section 7.4) with the output polarizer at 0 and 90 degree.

5.4 Conclusions

I demonstrated, both numerically and experimentally, that the introduction of cladding defects in a 7-cell PBG-HC fiber leads to a suppression of low loss surface modes that are otherwise guided within the transmission band. The defects are produces by independent pressurization of some of the cladding holes during draw and it is therefore adjustable. Spectral feature in the fiber transmission can be exploited during fabrication to adjust the spectral position of the induced defects modes as it can be seen in Fig.5.3. The resulting fiber has a lower polarization cross talk than state of the art PM PBG-HC fiber [34] allowing polarization maintenance over much longer lengths.

Driven by the good PM performance of the 7-cell PBG-HC-1 I measured its phase birefringence, showing that $B = 1{\times}10^{-5} \div 2.5{\times}10^{-5}$ is sufficient to have

a PER>15dB over 5 meter of fiber. This set a target for future development of HC fiber where PM properties are required over short distances.

The AR-HC do not show relevant PM properties and the output state of polarization is affected by the spatial arrangement of the fiber and varies if the fiber is moved. Designing a PM version of this kind of fibers is very challenging because of the extremely low overlap between the fundamental mode and the silica. On the other hand because of the very low scattering with the air-glass interface the coupling between the two polarization of the fundamental mode should be lower than in PBG-HC. This hopefully means that some relevant PM properties could arise from a modest phase birefringence, maybe even lower than 1×10^{-5}.

Chapter 6

High power pulse delivery

The ultra low non-linearity and the low and tailorable dispersion make hollow core fiber a unique medium for the delivery and manipulation of high power continuous wave and pulsed laser light. Since the early 2000s several experimental works were conducted to demonstrate the potential of PBG-HC fiber in beam delivery [53, 76–80], in the generation of solitons [81] and pulse compression [82–84]. In 2014 up to 200W CW laser at 1064nm was coupled to a 7-cell PBG-HC with as high as 90% coupling efficiency [85]. With the advent of large core Kagome hollow core fiber at first, and AR-HC fibers lately, larger and larger average powers and pulse energies could be coupled and guided through hollow core fibers resulting into a multitude of publications in this field [20, 86–90]. Recently impressive results were also obtained in delivery systems where HC fibers are connectorized [91, 92].

In this chapter I will describe the work I have conducted in showing experimentally that PBG-HC fibers and AR-HC offer a linear, non-dispersive medium for the delivery of picosecond pulses. Input pulse energies to up to 17 μJ and input average powers up to 90W were investigated, identifying some of the limitations of these fibers in terms of facet damage threshold and non-linearity. Large part of this work was published in [64].

The three fibers considered are 7-cell HC-PBG-1 described in Section 4.1, 19-cell HC-PBG-2 described in Section 4.2 and AR-Fiber1 described in Section 3.1. Table 6.1 summarizes the main fiber properties.

6.1 Optical set up and experimental procedure

The light source for the experiment consists of an ytterbium doped double clad fiber (aeroGAIN-ROD-PM85 from NKT Photonics) in a high power

Table 6.1: Summary of fiber properties.

	Loss @ 1032nm	MFD @ 1064nm	Modal content	Critical Bend radius	PM
7-cell PBG-HC-1	66 dB/km	7.8μ	Single mode	<3cm	yes
19-cell PBG-HC-2	66 dB/km (<20 dB/km is possible)	13μ	Weakly multimode	<3cm	no
AR-Fiber1	34 dB/km	22μ	Weakly multimode (Bend suppression of HOMs)	~3cm	no

amplifier setup [93]. It provided 22ps pulses with a maximum average power of 95W, 40MHz repetition rate at 1032nm (~2.4μJ pulse energy), with M^2<1.05. In order to investigate higher peak powers in the case of AR-Fiber1 the repetition rate was changed to 10MHz and 4MHz maintaining similar average powers. The active fiber has a mode field diameter of about 65μm and it is operated so to obtain an output signal with a PER of 25dB. Figure 6.1 shows a schematic representation of the optical set up. The upper part represents the backward pumped amplifier, the lower part the delivery through HC fibers. The lens L1 collimates the linearly polarized output from the amplifier. A half wave plate (HWP) and a polarizing beam splitter (PBS) are used to control the optical power reaching the fiber facet. Lenses L2 and L3 are arranged in a telescope. Mirrors M1 and M2 are used with the 3-axis stage to minimize angular and transverse misalignment. Lens L4 focuses the beam on the fiber facet. The waist of the input beam at the fiber facet was calculated by assuming a Gaussian beam and propagation through thin lenses. This allows to chose the lenses for a coarse optimization of the mode matching. A finer optimization is achieved by changing the relative position of L2 and L3. This produce a slightly converging or diverging beam after lens L3 and consequently a larger or smaller beam waist after L4. The output beam from the HC fibers is sampled twice with the beam samplers S1 and S2 and imaged on a camera. The output power and the light spectrum are monitored with a power meter and an optical spectrum analyzer, respectively. During the pulse delivery measurements the amplifier is maintained at a constant output average power. Most of the power is dumped into Power meter 1. The coupling optimization was done by an iterative two step process. Firstly the transverse and angular misalignment

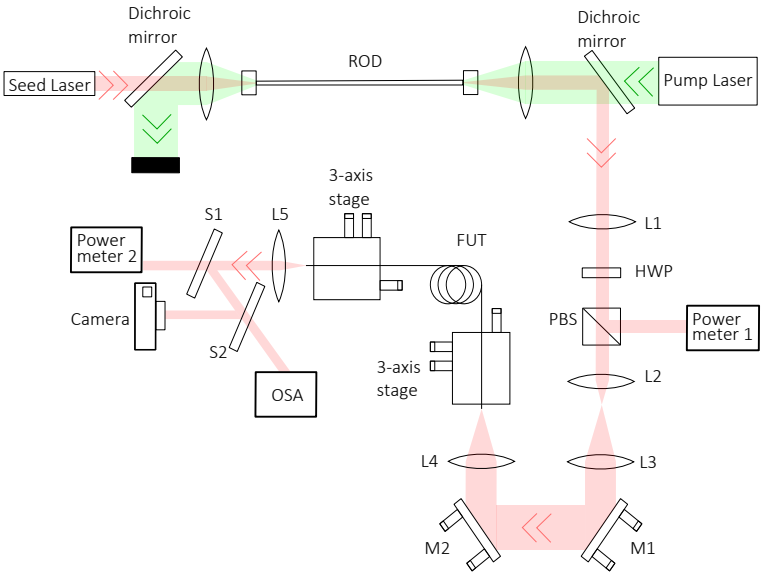

Figure 6.1: Schematics of the optical set up for pulse delivery. L1 to L5 are lenses, HWP is half wave plate, PBS is polarizing beam splitter. M1 and M2 are adjustable mirrors. S1 and S2 are wedges. OSA stands for optical spectrum analyzer.

are minimized through the two mirrors M1, M2 and the 3-axis stage holding the fiber. Secondly the relative position of L2 and L3 is changed. This was done at low average powers of 3 to 5W. The power reaching the fiber facet is later raised by rotating the HWP. Having the amplifier at a constant output power avoids the change in the beam output profile and pointing stability that might occur when varying the pump power. A summary of the lenses used for the different fibers is given in Table 6.2.

Table 6.2: Summary of the lenses used for the different fibers

FUT	L1	L2	L3	L4	L5
PBG-HC-1	200mm	50mm	100mm	35mm	6mm
PBG-HC-2	200mm	50mm	100mm	50mm	6mm
AR-HC	-	75mm	50mm	40mm	6mm

6.2 Results

In the following the transmission efficiency is defined as the ratio between the output power measured after the collimation lens L5 and the input power measured before the focusing lens L4, and the coupling efficiency is the transmission efficiency corrected by the fiber attenuation. The bare fiber terminations are secured to a v-groove mounted on 3-axis stages in the same way for the three fibers. Particular care was taken in cleaving the fibers so to obtain a facet that is as flat as possible. Irregularities in the micro-structure, especially around the core, can indeed lead to a reduced coupling efficiency and ultimately to a reduced threshold for the facet damage. All the fibers were operated in air.

7-cell HC-PBG-1

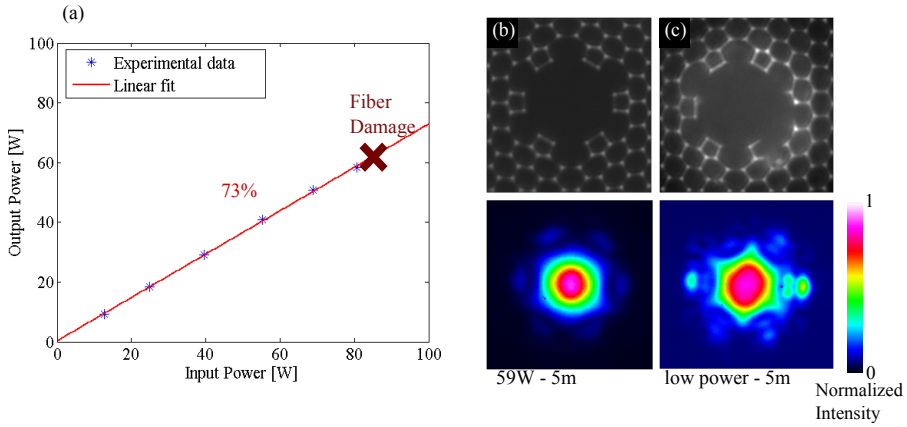

Figure 6.2: (a) Transmission efficiency over 5m FUT, (b) Fiber facet and output mode profile at 59W avarage power, (c) Facet of a damaged fiber and output near field after the fiber is damaged

The 7-cell PBG-HC-1 fiber was coiled in a standard 8 cm radius spool and no special handling was necessary. Figure 6.2(a) shows the achieved transmission efficiency of 73% for a 5m long fiber (~78% coupling efficiency), allowing us to reach up to 59W average power output (1.47 µJ pulse energy, 67kW peak power). Above this power level damage of the fiber facet was inevitable, see Fig. 6.2(c). In Fig. 6.3(a) the spectra for 2.5W and 59W average output power, measured with an OSA with 0.05nm resolution, are compared showing negligible, but measurable, spectral broadening. Figure

6.3(b) shows the 10dB spectral width as a function of the average output power. This suggest that even though the limitation in this fiber, for the considered light source, is set by the threshold for the facet damage, higher peak power would lead to a significant broadening due to non linearity. Among the three fibers here considered the 7-cell PBG-HC-1 is the one with the highest non-linearity because of the small MFD and higher overlap between the fundamental mode and the silica structure. As a consequence of this air and silica contributes approximately equally to the fiber non-linearity [94] and the possible improvements achieved by applying vacuum to the fiber are limited.

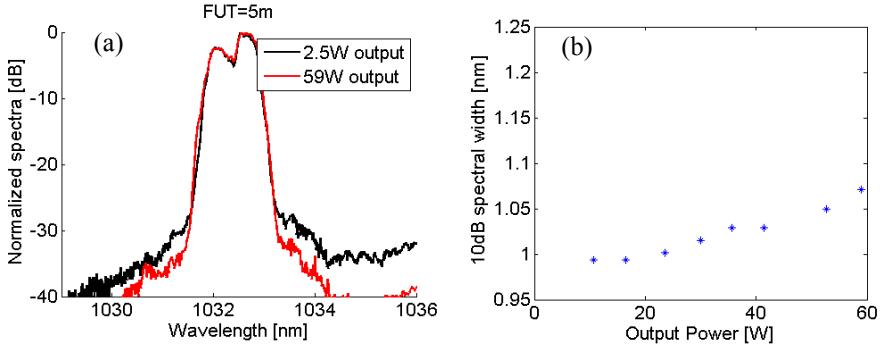

Figure 6.3: (a) Comparison of the output spectra at 2.5W and 59W average power. (b) 10dB spectral width as function of the output average power

19-cell PBG-HC-2

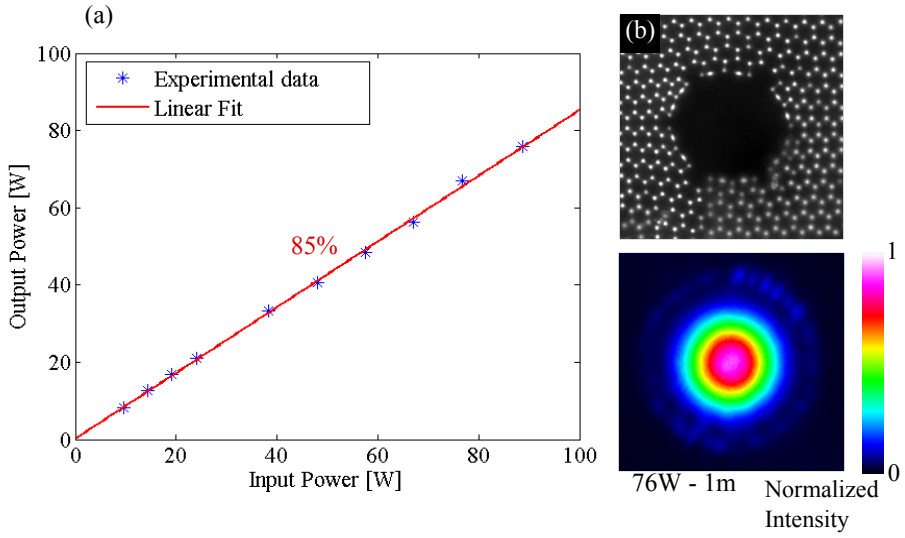

Figure 6.4: (a) Transmission efficiency over 1m FUT, (b) Fiber facet and output mode profile at 76W avarage power

Similarly for the 19-cell PBG-HC-2 fiber no special care was necessary in terms of fiber bending, the fiber had a bend radius < 8cm radius and could tolerate external perturbation, even at the maximum output power, with negligible effect on the output near field and power. Figure 6.4(a) shows that the achieved coupling transmission of 85% over 1m fiber (~86% coupling efficiency), with a maximum output average power of 76W (1.9µJ pulse energy, 86kW peak power). No spectral broadening was detected and we could not reach the fiber facet damage threshold. In order to observe some non-linearity coming from the hollow-core fiber we tested a 42m fiber. Due to fiber loss the highest output average power was 46.4W with 89W input. The fiber was coiled in a standard 8cm radius spool. In Fig. 6.5(a) the spectra, measured with an OSA with 0.05nm resolution, for 2.5W and 46.4W output are compared. A small spectral broadening is present and some strong extra lines appear at high power. The 10dB spectral width is shown in Fig. 6.5(b) as a function of the output average power. The measured broadening is likely an underestimation since the fiber is operated very close to the short wavelength edge of the bandgap (see Fig.4.4(c)). The lines at longer wavelengths arise from stimulated rotational Raman scattering (SRRS) from N_2 molecules. The Raman shift of the five strongest lines match the S(6),

S(8), S(9), S(10) and S(12) rotational transitions, and the spectrum is comparable to previously reported atmospheric measurements [95]. In order to prove this I calculated the N_2 rotational Raman response function as described in [96], and the calculated rotational Raman spectrum is compared to the measured one in Fig.6.5(c). This suggests that for this fiber the main contribution for non-linearity arises from the gas present in the fiber and can in principle be significantly suppressed by applying vacuum.

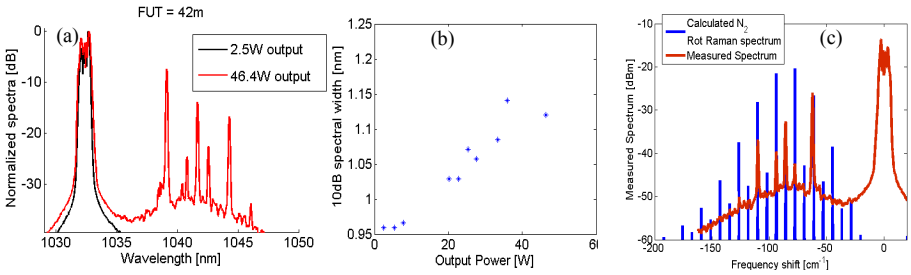

Figure 6.5: (a) Comparison of the output spectra at 2.5W and 46.4W average power. (b) 10dB Spectral width as function of the output average power. (c) Comparison between the measured spectrum and the calculated N_2 rotational Raman spectrum.

AR-Fiber1

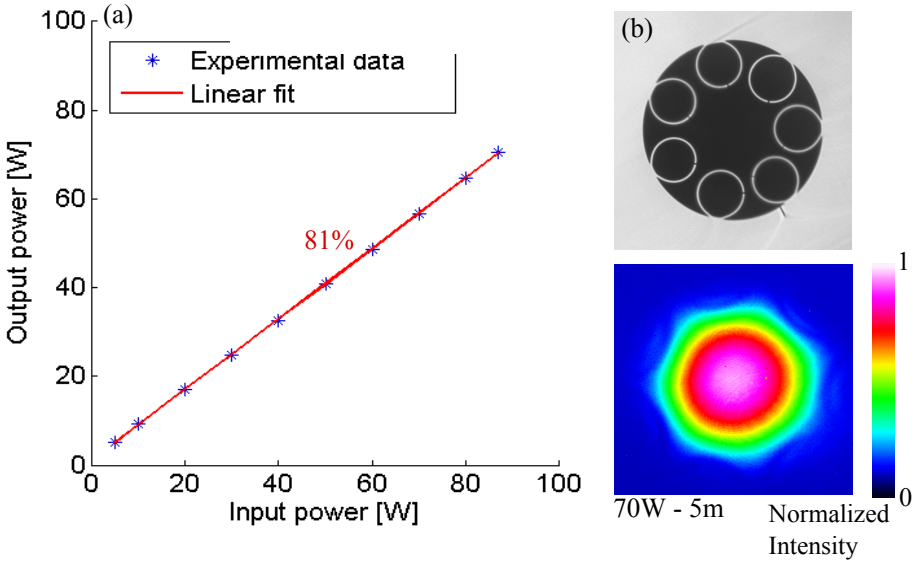

Figure 6.6: (a) Transmission efficiency over 5m FUT, (b) Fiber facet and output mode profile at 70W avarage power

The 7-tube AR-HC fiber was coiled in a 16 cm radius spool to avoid any possible bend loss contribution. For this fiber we performed the measurement for lower repetition rate of 10MHz and 4MHz.

At 10MHz the transmission efficiency was 81% for a 5m FUT(~85% coupling efficiency, see Fig. 6.6(a)) with a maximum output average power of 70W (7µJ pulse energy, 318kW peak power, near field profile in Fig. 6.6(b)). No spectral broadening was detected and we could not reach the fiber facet damage threshold, see Fig. 6.7(a).

The coupling transmission and efficiency were analogous in the case of 4MHz repetition rate and we obtained up to 56W output average power (14µJ pulse energy, 636kW peak power, limited by the light source) with no spectral broadening.

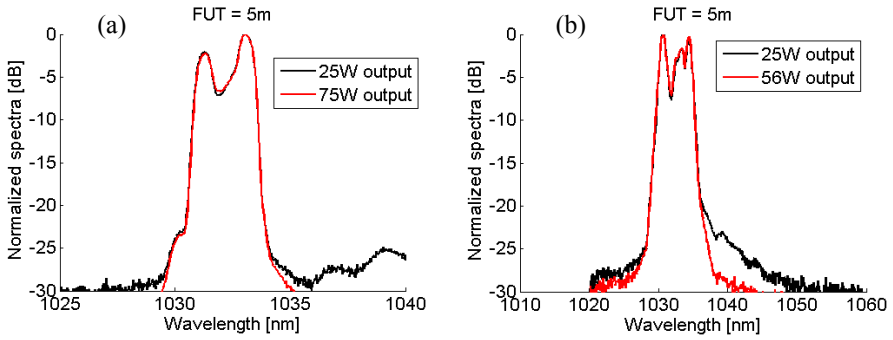

Figure 6.7: (a) Comparison of the output spectra at 25W and 75W average power, with a repetition rate of 10MHz (b) Comparison of the output spectra at 25W and 56W average power, with a repetition rate of 4MHz

6.3 Conclusions

The 7-cell PBG-HC-1 fiber is the only one that showed a clear facet damage threshold within the power levels investigated. Preliminary results (not shown) suggests that pulses with higher peak power can be delivered with this fiber and hence the high average power plays a role in the damage formation. Because of the small core is also the fiber among the three considered where the coupling accuracy and stability is more demanding and only 78% coupling efficiency was possible. This also means that the fiber could tolerate more than 20W of optical power that was not coupled to the fundamental mode before damage occurred. Possible improvements in the coupling efficiency will certainly improve the damage threshold of the facet, but as suggested by Fig.6.3(b) will also likely lead to an appreciable contribution from the fiber non-linearity.

Similar coupling efficiency were obtained for 19-cell PBG-HC-2 and AR-Fiber1 of approximately 86% and 85%, respectively. Higher coupling efficiency were obtained in [92] for similar fibers. This suggests that the limitation is likely due to the optical set up and we expect further improvements in the future. Both fibers do not show any sign of non-linearity for short fiber sections and much higher pulse energies and average powers are expected to be possible.

A longer section of 42m of the 19-cell PBG-HC-2 showed non-linearity arising from N_2. This sets a clear limit for the pulse energies at which the fiber can be considered linear, nevertheless since the non-linearity comes from the gas

within the hollow core it can easily be reduced by applying vacuum. It also demonstrate to which extend the light matter interaction can be enhanced in a hollow core fiber. A previous experiment done in atmospheric air used a 5cm beam diameter in air with 35m path, 20J pulse energy, 600ps pulse duration at 1054nm in order to observe a similar SRRS response [95].

All the fiber are robust towards bending and can be touched and moved with negligible impact on the output power and beam stability.

This promising initial results encouraged the pursuit of a delivery system where the fiber is connectorized and embedded in a robust cable. In light of this I have collaborated into a patent application for a HC fiber connector [97].

Chapter 7

Fiber characterization techniques and procedures

In this chapter I will described the main experimental techniques I have used to characterized the hollow core fibers discussed in this thesis.

7.1 Spatially resolved side scattering (SRSS)

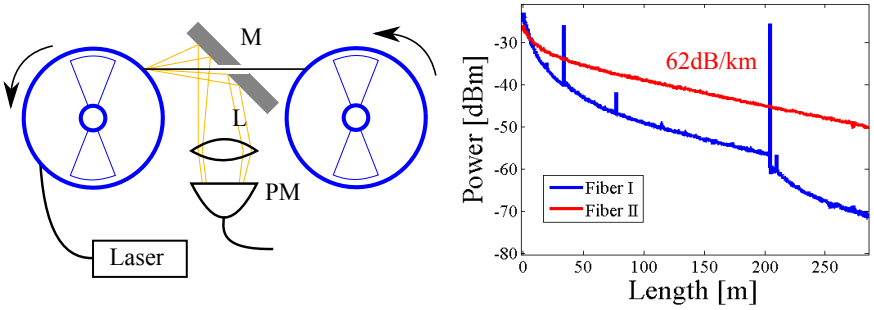

Figure 7.1: On the left there is a scheme of the experimental set up. The blue circles represent two fiber spools. M is a mirror with a cut that allows the fiber to pass through it. L is a lens and PM is a photomultiplier. On the right an example of the measurement output

This measurement is performed to identify sections of fiber that are defect free. Figure 7.1 shows a scheme of the experimental set up. A fiber is re-wound from a spool to another. A laser light source with fiber output

is butt-coupled to the FUT. The delivery fiber has a joint that is free to rotate to avoid twist while the FUT is rewinded. A photomultiplier is placed in between the two spools and collect the light that is scattered out from the side of the FUT. The FUT passes through a cut mirror. A lens with short focal lens is placed in between the mirror and the photomultiplier to maximize the amount of scattered light from the FUT that reaches the detector, as depicted in 7.1. This set up hence allow to collect the scattered light as a function of the fiber position. Figure 7.1 also shows two typical measurements for PBG-HC. Fiber I shows several scatter points that are indicators of a core defect. Fiber II instead is defect free for the whole length. The curve correspond to a sum of exponential with a fast decay at the fiber beginning and a slower decay afterwards. This behavior is due to the coupling to high order modes that have higher loss and hence contribute to the initial fast decay of the scattered light. In Fig7.1 for Fiber II, after approximately 50 meter the remaining light in the fiber core is only in the fundamental mode. The curve slope above 50 meters gives an estimation of the fundamental mode loss at the laser wavelength. For Fiber II the measurement was done at 1064nm and the fundamental mode loss corresponds to 62dB/km.

7.2 Loss measurement

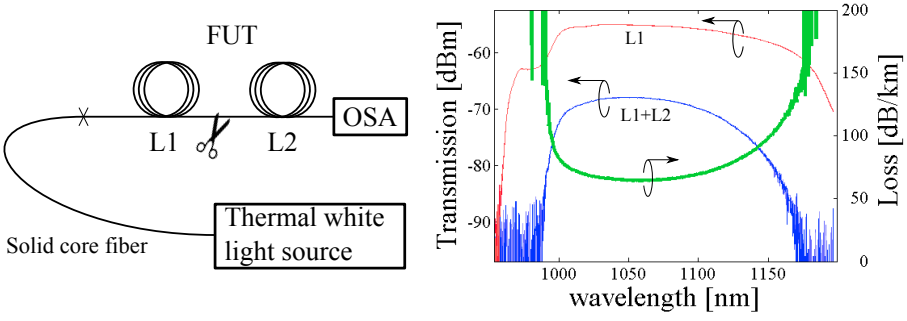

Figure 7.2: On the left there is a scheme of the loss measurement. The FUT is coiled in two sections of length L1 and L2. Light is coupled by butt-coupling with a solid core fiber and the output spectrum from the FUT is measured with an OSA. On the right a typical measurements of the transmission spectra for different fiber lengths and the corresponding fiber loss.

In order to measure the loss of the fundamental mode in hollow core fibers I used the cutback technique. The general principle is to measure the transmission spectrum through different fiber lengths and through these spectra calculate the fiber attenuation. In order to exclude the contributions given by the low reproducibility of the coupling from the light source to the hollow core fiber, a single fiber is used. A thermal white light source is typically preferred over supercontunuum light sources for the higher stability of its spectrum over the time of the measurement. A single mode solid core fiber delivers the light signal to the hollow core fiber. The core size of the solid core fiber is chosen to closely match the mode field diameter of the hollow core fiber and butt-coupling is used to couple the light signal to the hollow core fiber. Maintaining a stable coupling to the FUT a first set of spectra is collected on the full fiber length, the fiber is cut to a shorter length and a second set of spectra is collected for the shorter fiber length. The spectra are collected with a optical spectrum analyzer. A set of minimum 3 spectra is collected at each fiber length, where the fiber is freshly cleaved each time. This is done to ensure that the cleave to cleave variations are minimal and averaged out. Typical variations due to cleaving are of the order of less than 0.1 dB. Figure 7.2 shows a scheme of the measurement. The FUT length L1 is chosen to achieve an optimal spatial filter, i.e. L1 is such that high order modes with relative high loss are strongly attenuated in comparison to the fundamental mode. The information obtained by the SRSS (see sec.7.1) on the length necessary to suppress the HOM content in the fiber is used to optimally chose L1. The length L2 is chosen to obtain a large enough difference between the spectra collected for the two fiber lengths. A difference of at least 1 dB is necessary to achieve accurate results, and preferably as large as possible to minimize the uncertainty contribution given by the cleaving. Figure 7.2 shows an example of a cutback measurement where three spectra are collected at length L1+L2 and three more after the fiber is cut to the length L1. The loss at 1064nm is 64dB/km that is in close agreement with the estimation done for the same fiber in the SRRS set up (Fiber II in fig. 7.1).

Bend loss is negligible in PBG-HC fibers and have no effect on their loss measurement. On the contrary AR-HC are much more bend sensitive. Large spool diameter are necessary to exclude any bend induced contribution to the loss measurement. AR-HC can also show strong

suppression of HOMs through bending. This can be used in the loss measurement to reduce drastically the length L1.

7.3 Group velocity dispersion and HOM measurements

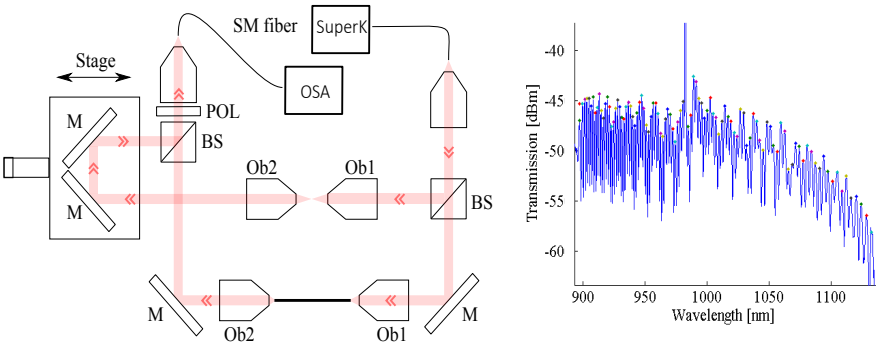

Figure 7.3: Left: Scheme of the dispersion set up where BS are beam splitters, M are mirrors, Ob1 and Ob2 are objectives, POL is a polarizer and SM fiber is a single mode fiber. Right: An example of a collected spectrum. The color dots are the peak positions as recovered by a sine function fit performed for each peak. The large peak at 1064nm is due to the pump of the supercontinuum and it is neglected.

The fiber group velocity dispersion (GVD) can be measure with a white light interferometric Mach-Zender set up [98, 99] as in Fig.7.3. In the signal arm of the interferometer the light from a supercontinuum light source is coupled through a 8cm FUT. The reference arm of the interferometer has the same optical components to cancel out their dispersion contributions. The length of the reference arm can be adjusted so that is possible to have similar optical path for the light traveling in the two arms. The combined beams after the second beam splitter are launched into a single mode fiber. The spectrum is measured with an optical spectrum analyzer. Because of the fiber dispersion, the measured spectrum shows spectral interference. The group index difference between the arms can be expressed in terms of the spacing between neighboring maxima $\Delta\lambda$ as follow:

$$B_g = \frac{\lambda^2}{\Delta\lambda L} + n_g^{ref}\frac{\Delta L}{L} \tag{7.1}$$

where L is the FUT length, ΔL is the difference in length between the two arm of the interferometer, n_g^{ref} is the group index of the reference arm. From the measured spectrum the position of the peaks are determined by a sinusoidal fit and $\Delta\lambda(\lambda) = \lambda_i^{peak} - \lambda_{i-1}^{peak}$ is calculated. An example of the collected spectrum is in Fig.7.3(right) where the position of the peak is highlighted. Assuming n_g^{ref} to be constant in wavelength the following approximation is used to calculate the fiber dispersion:

$$D(\lambda) \doteq \frac{1}{c}\frac{dn_g}{d\lambda} \simeq \frac{1}{c}\frac{dB_g}{d\lambda} \tag{7.2}$$

A polynomial fit is performed on the data set $\frac{\lambda^2}{\Delta\lambda L}$ derived from the spectrum. The fitted curve is differentiated to calculate $D(\lambda)$. Figure 7.3 shows an example of the obtained dispersion curve.

The same set up can also be used to measure the group index difference between the fundamental mode and HOMs. In this case the reference arm is blocked, light is couple with a misalignment to the fiber to ensure the excitement of HOMs. Light propagating in different spatial modes experience different group indices. Similarly to the GVD measurement, the measured spectrum shows spectral interference Because of the interaction of several guided modes the spectrum is more complex to analyze. A windowed Fourier transform is performed on the spectrum in order to obtain an interferogram. This technique was for instance used in [4] to determine the cutoff wavelength at the short wavelength edge of the bandgap of the LP_{11} mode for a 7-cell PBG-HC fiber. Figure 7.4 shows the obtained interferogram and compares the results to the simulated group refractive index differences of the fundamental modes with several HOMs and a surface mode. Noticeably also the present of a surface mode can be clearly identify thanks to the comparison with the numerical simulation.

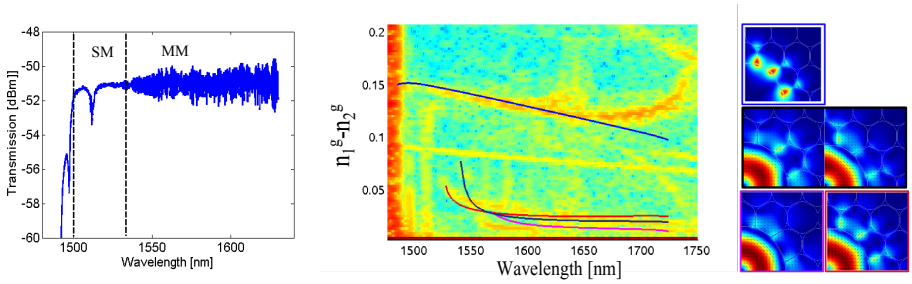

Figure 7.4: Left: Transmission spectrum of a ~80mm long FUT, measure with the set up in Fig.7.3 and no reference beam. At the short wavelength edge there is a single mode region, while at longer wavelengths a beating between different spatial modes is measured. Right: Windowed Fourier transform of the measured spetrum highlights the presence of HOMs and their cutoff wavelengths. The measured results are compared to a simulation of the fiber showing good agreement.

7.4 Polarization extinction ratio, group modal birefringence and h-parameter

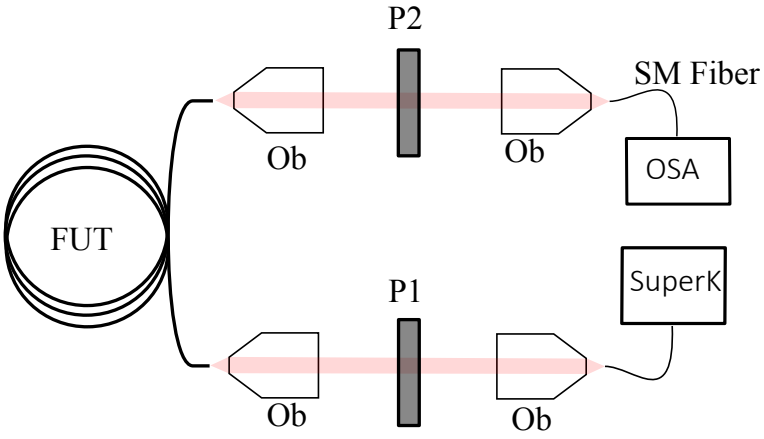

Figure 7.5: Scheme of the set up used to measure the fiber polarization extinction ratio, group modal birefringence and h-parameter. Ob are objective lenses, P1 and P2 are polarizers, and SM fiber stands for single mode fiber.

Some of the fibers discussed in this thesis are polarization maintaining. In order to achieve that the fiber has to be birefringent, i.e. two polarization of the fundamental mode propagate through the fiber with a different effective index. The separation in effective index lowers the coupling between the two fundamental modes, allowing for linearly polarized light coupled to one of the fundamental modes to maintain its polarization state to a certain degree along the propagation through the fiber.

Some of the small core PBG-HC fibers show polarization maintenance through a short fiber section despite they are not explicitly designed to be birefringent. This is due to a slight elliptical core. To quantify the polarization properties of these fibers I have simply measured the PER over a short distance (5 meters). The light source for this measurement is supercontinuum light source. As shown in fig. 7.5 a polarizer is placed at both the input and output of the fiber. The linearly polarized input light is coupled to the FUT, carefully adjusting the angle of the polarization to one of the fiber axis. This is achieved by optimizing the angle of both polarizers P1 and P2 and monitoring the output spectrum. The polarizer P2 is rotated and spectra are collected for maximum extinction and transmission. The two spectra are subtracted on a dB scale to obtain the PER. The measurement can also be performed in presence of bend or twist to evaluate the fiber robustness towards external perturbation.

With the same set up it is also possible to measure the fiber group modal birefringence (GMB), i.e. the difference in group effective index of the two polarization of the fundamental mode. The measure is done launching the linearly polarized light with an angle with respect to the fiber axis. Light at different wavelengths experience different phase shifts due to the wavelength dependence of the birefringence. Because of the polarizer P2 only linearly polarized light in one direction is collected and the resulting spectrum shows spectral interference. The GMB can be calculated by:

$$GMB = \frac{\lambda^2}{\Delta\lambda L} \tag{7.3}$$

where $\Delta\lambda(\lambda) = \lambda_i^{peak} - \lambda_{i-1}^{peak}$ is the spacing between neighboring maxima.

Another important quantity that characterize the polarization maintenance of a fiber is the polarization crosstalk. The polarization crosstalk (C) is defined [75] as the logarithmic ratio of the power P_x (P_y) coupled to the unexcited mode polarized along x (y) axis, with respect to the total transmitted power $P_x + P_y$ over a propagation length L, and it can be expressed in terms of the polarization holding parameter h:

$$C = 10\log\left(\frac{P_x}{P_x + P_y}\right) = 10\log\left(\frac{1 - \exp(-2hL)}{2}\right) \tag{7.4}$$

The product hL is therefore approximately equal to P_x/P_y for $hL \ll 1$ and h can be interpreted as the the percentage of power that in transferred to the other polarization per unit length.

To estimate experimentally the h-parameter using the set up in fig. 7.5 one can use the approximation [75]:

$$h \simeq \frac{2}{L(\rho_x + \rho_y)}, \qquad \rho_x = \frac{P_x(L)}{P_y(L)} \quad for\ P_y(0) = 0, \qquad \rho_y = \frac{P_y(L)}{P_x(L)} \quad for\ P_x(0) = 0 \tag{7.5}$$

where L is the length of the FUT and $P_x(l)$, $P_y(l)$ the optical powers in the two principle axis of the fiber at the given fiber length l.

Chapter 8

Conclusions

In this work I considered both PBG-HC fibers and AR-HC fibers, analyzing and comparing their optical properties in view of their application in high power beam delivery. In Chapter 2 I have described the guidance mechanism of hollow core fibers. The considerations done in this chapter regarding AR-HC fibers show that is possible to aim at large core hollow core fiber without giving up nearly single mode propagation and bend robustness. This is best achieved with a novel fiber structure with 7 non-touching cladding tubes. Following these numerical predictions I showed in Chapter 3 the efforts that were taken in NKT Photonics to fabricate AR-HC fibers with non-touching tubes. Even though we did not succeeded into drawing a fiber with the target structure we obtained several guiding AR-HC fibers and two with particularly remarkable optical properties. I showed experimentally that some of the HOMs are suppressed by resonantly couple them to high loss cladding modes. Moreover the strong agreement between the numerical calculations and the real fiber modal properties firmly encourage to pursuit a single mode large core AR-HC fiber. The realized AR-HC fibers proved to be far more robust towards bending than other AR-HC previously reported, making them viable candidate for applications where tight bending and continuous fiber movement are necessary. Moreover I showed that despite the LP_{11}-like modes have relatively low loss for a straight fiber it is possible to strongly suppress them through bending, therefore achieving a nearly single mode output beam. The encouraging numerical and experimental results resolved in a patent application on the 7-tube AR-HC fiber design [68].

Chapter 4 was dedicated to present the optical properties of two PBG-HC fibers that were used in the high power beam delivery experiment. In the chapter I also introduced a technique to numerically simulate the modal prop-

erties of a 7-cell PBG-HC that takes into account the peculiarities present in a real fiber structure. The numerical tool is used to get a deeper understanding of the measured modal properties.

In the frame of PBG-HC fibers the presence of low loss surface modes can affect the output beam quality and it can be detrimental in all those applications where strict single mode propagation is a required. I analyzed a way to minimize the surface modes in Chapter 5 by introducing a number of defects that are tunable during drawing. I showed both numerically and experimentally that the suppression of surface modes is achieved. Moreover one of the realized fiber shows very low cross-talk between the two polarization of the fundamental mode allowing it to maintain polarization over hundreds of meters. This fiber could potentially find application in the field of fiber optical gyroscopes.

The characterization of the polarization properties of a 7-cell PBG-HC in Chapter 5 showed a PER>15dB over 5 meters of fiber that is robust over external perturbations. This performance is good enough for several applications where a linearly polarized output is desired. I therefore measured experimentally the amount of phase birefringence in this fiber in order to define how much birefringence is needed for a PBG-HC to maintain the polarization over a short distance. This sets a target for future development of PM properties in hollow core fibers. In the same chapter I also characterize the polarization properties of one of the realized AR-HC. I showed that, despite it is possible to obtain a linearly polarized output over 5m of fiber, it is extremely sensitive to external perturbation and polarization cross-talk is present even for short fiber lengths. This means that the AR-HC can not maintain the polarization state of the input light and only different designs that exploit relative variations in the cladding tube sizes could potentially achieve polarization maintenance. Recent publications showed that the birefringence induced by a form factor in AR-HC fibers is very low and only considering complex structures with small core sizes can lead to large birefringence [44, 45]. This results are very interesting but because of the small cores and complex geometry are not very appealing, especially considering the actual state of the art in PM PBG-HC fiber. Hopefully future work will provide a large core AR-HC fiber with a high enough birefringence to maintain the state of polarization over short distances.

As a demonstration of the capabilities of HC in propagating high power pulsed light I characterized two PBG-HC fibers and a AR-HC fiber in delivering picosecond pulses. The outstanding optical powers that the HC fibers could deliver demonstrate, as many other works in literature, the huge po-

tential of these fibers as a non dispersive linear medium. In the specific field of beam delivery their employment will confer an otherwise unmatched flexibility to single mode high power pulsed lasers. More than that the laser system will be detached from the processing area allowing for fast and efficient maintenance.

The realization of a bend insensitive and polarization maintaining HC fiber that provides a single mode, diffraction limited beam is extremely challenging, and PBG-HC and AR-HC are complementary. PBG-HC fibers are extremely robust towards bending and can be more easily designed to maintain polarization, while the large core of AR-HC fibers relaxes the coupling tolerances and it allows for much higher peak and average powers.

8.1 Outlook

Future development on HC fibers for high power laser applications will certainly head towards truly single mode large core fibers, achieving lower losses and more robust bending performances. AR-HC core have proved to be an exciting platform for this aim. Improvements in the fabrication technique will allow more and more complex structures to be realized, and a fine tailoring of their modal properties will be possible. In this regard obtaining a significant birefringence in large core AR-HC fiber is likely the most challenging and appealing target.

Beside of development on the fiber itself, much work is still needed to integrate HC fiber in practical industrial applications. The development of connectors specifically designed to account for the features of HC fiber will be essential for a widespread employment of these fibers.

Bibliography

[1] N. Y. Joly, J. Nold, W. Chang, P. Hölzer, A. Nazarkin, G. K. L. Wong, F. Biancalana, and P. S. J. Russell, "Bright spatially coherent wavelength-tunable deep-UV laser source using an Ar-filled photonic crystal fiber," Phys. Rev. Lett. **106**, 203901 (2011). 1

[2] F. Benabid, J. C. Knight, G. Antonopoulos, and P. S. J. Russell, "Stimulated Raman scattering in hydrogen-filled hollow-core photonic crystal fiber," Science **298**, 399–402 (2002). 1, 3

[3] J. Henningsen, J. Hald, and J. C. Peterson, "Saturated absorption in acetylene and hydrogen cyanide in hollow-core photonic bandgap fibers." Opt. Express **13**, 10475–10482 (2005). 1

[4] M. Triches, M. Michieletto, J. Hald, J. K. Lyngsø, J. Lægsgaard, and O. Bang, "Optical frequency standard using acetylene-filled hollow-core photonic crystal fibers," Opt. Express **23**, 11227–11241 (2015). 1, 85

[5] P. G. Westergaard, J. W. Thomsen, M. R. Henriksen, M. Michieletto, M. Triches, J. K. Lyngsø, and J. Hald, "Compact , CO 2 -stabilized tuneable laser at 2 . 05 microns," Opt. Express **24**, 4872–4880 (2016). 1

[6] S. Vorrath, S. A. Muller, P. Windpassinger, K. Bongs, and K. Sengstock, "Efficient guiding of cold atoms through a photonic band gap fiber," New J. Phys. **12** (2010). 1

[7] M. Langbecker, M. Noaman, and P. Windpassinger, "Towards nonlinear optics with cold Rydberg atoms inside a hollow core fiber," Cleo_Si 2015 pp. 4–5 (2015). 1

[8] V. A. J. M. Sleiffer, P. Leoni, Y. Jung, H. Chen, M. Kuschnerov, S. U. Alam, M. Petrovich, F. Poletti, N. V. Wheeler, N. Baddela, J. Hayes, E. Numkam Fokoua, D. J. Richardson, L. Gruner-Nielsen, Y. Sun, and H. De Waardt, "Ultra-high capacity transmission with few-mode silica and hollow-core photonic bandgap fibers," Conf. Opt. Fiber Commun. Tech. Dig. Ser. pp. 4–6 (2014). 2

[9] J. R. Hayes, S. R. Sandoghchi, T. D. Bradley, Z. Liu, R. Slavík, M. A. Gouveia, N. V. Wheeler, G. T. Jasion, Y. Chen, E. N. Fokoua, M. N. Petrovich, D. J. Richardson, and F. Poletti, in , 2
(2016), p. Th5A.3.

[10] T. Ritari, J. Tuominen, H. Ludvigsen, J. Petersen, T. Sørensen, T. Hansen, and H. Simonsen, "Gas sensing using air-guiding photonic bandgap fibers." Opt. Express **12**, 4080–4087 (2004). 2

[11] A. M. Cubillas, J. Hald, and J. C. Petersen, "High resolution spectroscopy of ammonia in a hollow-core fiber." Opt. Express **16**, 3976–3985 (2008). 2

[12] F. Yang, W. Jin, Y. Cao, H. L. Ho, and Y. Wang, "Towards high sensitivity gas detection with hollow-core photonic bandgap fibers," Opt. Express **22**, 24894 (2014). 2

[13] V. Dangui, H. Kim, M. Digonnet, and G. Kino, "Phase sensitivity to temperature of the fundamental mode in air-guiding photonic-bandgap fibers." Opt. Express **13**, 6669–6684 (2005). 2

[14] M. Pang and W. Jin, "Detection of acoustic pressure with hollow-core photonic bandgap fiber." Opt. Express **17**, 11088–97 (2009). 2

[15] M. J. Digonnet, H. K. Kim, S. Blin, V. Dangui, and G. S. Kino, "Sensitivity and Stability of an Air-Core Fiber-Optic Gyroscope," Opt. Fiber Sensors p. ME1 (2006). 2

[16] S. Girard, J. Baggio, and J. Leray, "Radiation-Induced Effects in a New Class of Optical Waveguides : The Air-Guiding Photonic Crystal Fibers," IEEE Trans. Nucl. Sci. **52**, 2683–2688 (2005). 2

[17] F. Couny, F. Benabid, and P. S. Light, "Large-pitch kagome-structured hollow-core photonic crystal fiber," Opt. Lett. **31**, 3574–3576 (2006). 2

[18] Y. Y. Wang, N. V. Wheeler, F. Couny, P. J. Roberts, and F. Benabid, "Low loss broadband transmission in hypocycloid-core Kagome hollow-core photonic crystal fiber." Opt. Lett. **36**, 669–671 (2011). 2

[19] A. D. Pryamikov, A. S. Biriukov, A. F. Kosolapov, V. G. Plotnichenko, S. L. Semjonov, and E. M. Dianov, "Demonstration of a waveguide regime for a silica hollow-core microstructured optical fiber with a negative curvature of the core boundary in the spectral region > 3.5 μm." Opt. Express **19**, 1441–8 (2011). 2, 3, 7

[20] P. Jaworski, F. Yu, R. R. J. Maier, W. J. Wadsworth, J. C. Knight, J. D. Shephard, and D. P. Hand, "Picosecond and nanosecond pulse delivery through a hollow-core negative curvature fiber for micro-machining applications," Opt. Express **21**, 22742–22753 (2013). 2, 40, 71

[21] W. Belardi, "Design and Properties of Hollow Antiresonant Fibers for the Visible and Near Infrared Spectral Range," J. Light. Technol. **33**, 4497–4503 (2015). 2

[22] R. F. Cregan, "Single-Mode Photonic Band Gap Guidance of Light in Air," Science **285**, 1537–1539 (1999). 3

[23] P. Roberts, F. Couny, H. Sabert, B. Mangan, D. Williams, L. Farr, M. Mason, A. Tomlinson, T. Birks, J. Knight, and P. St J Russell, "Ultimate low loss of hollow-core photonic crystal fibres," Opt. Express **13**, 236–244 (2005). 3, 20, 54, 61

[24] K. Saitoh, N. J. Florous, T. Murao, and M. Koshiba, "Design of photonic band gap fibers with suppressed higher-order modes: towards the development of effectively single mode large hollow-core fiber platforms." Opt. Express **14**, 7342–7352 (2006). 3

[25] M. N. Petrovich, F. Poletti, a. van Brakel, and D. J. Richardson, "Robustly single mode hollow core photonic bandgap fiber." Opt. Express **16**, 4337–4346 (2008). 3

[26] J. K. Lyngsø, C. Jakobsen, H. R. Simonsen, and J. Broeng, "Single-mode 7-cell core hollow core photonics crystal fiber with increased bandwidth," 21st Int. Conf. Opt. Fibre Sensors **7753**, 77533Q–77533Q–4 (2011). 3, 15, 17, 59

[27] J. M. Fini, J. W. Nicholson, B. Mangan, L. Meng, R. S. Windeler, E. M. Monberg, A. DeSantolo, F. V. DiMarcello, and K. Mukasa, "Polarization maintaining single-mode low-loss hollow-core fibres," Nat. Commun. **5**, 5085 (2014). 3, 27

[28] R. Amezcua-Correa, N. G. Broderick, M. N. Petrovich, F. Poletti, and D. J. Richardson, "Optimizing the usable bandwidth and loss through core design in realistic hollow-core photonic bandgap fibers." Opt. Express **14**, 7974–7985 (2006). 3, 17

[29] M. Michieletto, J. K. Lyngsø, J. Lægsgaard, and O. Bang, "Cladding defects in hollow core fibers for surface mode suppression and improved birefringence." Opt. Express **22**, 23324–32 (2014). 3

[30] X. Chen, M.-J. Li, N. Venkataraman, M. Gallagher, W. Wood, A. Crowley, J. Carberry, L. Zenteno, and K. Koch, "Highly birefringent hollow-core photonic bandgap fiber." Opt. Express **12**, 3888–3893 (2004). 3

[31] P. J. Roberts, D. P. Williams, H. Sabert, B. J. Mangan, D. M. Bird, T. a. Birks, J. C. Knight, and P. S. J. Russell, "Design of low-loss and highly birefringent hollow-core photonic crystal fiber." Opt. Express **14**, 7329–7341 (2006). 3, 57

[32] B. Mangan, J. Lyngso, and P. Roberts, "Realization of low loss and polarization maintaining hollow core photonic crystal fibers," 2008 Conf. Lasers Electro-Optics 2008 Conf. Quantum Electron. Laser Sci. pp. 5–6 (2008). 3

[33] G. Kim, K. Hwang, K. Lee, K. S. Lee, Y.-G. Han, and S. B. Lee, "Experimental study of an elliptical-core photonic bandgap fiber with thin core wall and high aspect ratio and its birefringence characteristics," Appl. Phys. B **101**, 583–586 (2010). 3

[34] J. K. Lyngsø, C. Jakobsen, H. R. Simonsen, and J. Broeng, "Truly single-mode polarization maintaining hollow core PCF," 22nd Int. Conf. Opt. Fiber Sensors **8421**, 84210C–1–84210C–4 (2012). 3, 57, 64, 68

[35] Y. Wang, F. Couny, P. Roberts, and F. Benabid, "Low loss broadband transmission in optimized core-shape Kagome Hollow-Core PCF," Lasers Electro-Optics Quantum Electron. Laser Sci. Conf. (QELS), 2010 Conf. p. CPDB4 (2010). 3

[36] L. Vincetti and V. Setti, "Waveguiding mechanism in tube lattice fibers," Opt. Express **18**, 23133–23146 (2010). 3, 21, 23

[37] W. Belardi and J. C. Knight, "Effect of core boundary curvature on the confinement losses of hollow antiresonant fibers." Opt. Express **21**, 21912–7 (2013). 3, 7

[38] A. N. Kolyadin, A. F. Kosolapov, A. D. Pryamikov, A. S. Biriukov, V. G. Plotnichenko, and E. M. Dianov, "Light transmission in negative curvature hollow core fiber in extremely high material loss region." Opt. Express **21**, 9514–9 (2013). 3

[39] W. Belardi and J. C. Knight, "Negative curvature fibers with reduced leakage loss," Opt. Fiber Commun. Conf. **1**, Th2A.45 (2014). 3

[40] F. Poletti, "Nested antiresonant nodeless hollow core fiber," Opt. Express **22**, 23807–23828 (2014). 3, 20

[41] W. Belardi, "Design and Properties of Hollow Antiresonant Fibers for the Visible and Near Infrared Spectral Range," **33**, 4497–4503 (2015). 3

[42] M. S. Habib, O. Bang, and M. Bache, "Low-loss hollow-core silica fibers with adjacent nested anti-resonant tubes," Opt. Express **23**, 17394–17406 (2015). 3

[43] M. S. Habib, O. Bang, and M. Bache, "Low-loss single-mode hollow-core fiber with anisotropic anti-resonant elements." Opt. Express **24**, 8429–36 (2016). 3

[44] W. Ding and Y.-y. Wang, "Hybrid transmission bands and large birefringence in hollow-core anti-resonant fibers," **23**, 21165–21174 (2015). 3, 90

[45] S. A. Mousavi, D. J. Richardson, S. R. Sandoghchi, and F. Poletti, "First Design of High Birefringence and Polarising Hollow Core Anti-resonant Fibre," pp. 4–6. 3, 90

[46] N. M. Litchinitser, a. K. Abeeluck, C. Headley, and B. J. Eggleton, "Antiresonant reflecting photonic crystal optical waveguides." Opt. Lett. **27**, 1592–1594 (2002). 7, 17, 23, 24

[47] E. A. J. Marcatili and R. A. Schmeltzer, "Hollow Metallic and Dielectric Waveguides for Long Distance Optical Transmission and Lasers," Bell Syst. Tech. J. **43**, 1783–1809 (1964). 7, 25

[48] P. S. J. Russell, "Photonic-crystal fibers," J. Light. Technol. **24**, 4729–4749 (2006). 10

[49] T. Birks, P. Roberts, P. Russell, D. Atkin, and T. Shepherd, "Full 2-D photonic bandgaps in silica/air structures," Electron. Lett. **31**, 1941 (1995). 10

[50] F. Couny, F. Benabid, P. J. Roberts, M. T. Burnett, and S. a. Maier, "Identification of Bloch-modes in hollow-core photonic crystal fiber cladding." Opt. Express **15**, 325–338 (2007). 12

[51] T. a. Birks, G. J. Pearce, and D. M. Bird, "Approximate band structure calculation for photonic bandgap fibres." Opt. Express **14**, 9483–9490 (2006). 12

[52] F. Benabid and P. J. Roberts, "Linear and nonlinear optical properties of hollow core photonic crystal fiber," J. Mod. Opt. **58**, 87–124 (2011). 12

[53] F. Luan, A. George, T. Hedley, G. Pearce, D. Bird, J. Knight, and P. Russell, "All-solid photonic bandgap fiber," Opt. Lett. **29**, 2369 (2004). 14, 71

[54] F. Poletti, M. N. Petrovich, and D. J. Richardson, "Hollow-core photonic bandgap fibers: technology and applications," Nanophotonics **2**, 315–340 (2013). 14

[55] K. Saitoh, N. Mortensen, and M. Koshiba, "Air-core photonic band-gap fibers: the impact of surface modes," Opt. Express **12**, 394–400 (2004). 15

[56] J. A. West, C. M. Smith, N. F. Borrelli, D. C. Allan, and K. W. Koch, "Surface modes in air-core photonic band-gap fibers," Opt. Express **12**, 1485 (2004). 15

[57] S. Selleri, F. Poli, M. Foroni, and A. Cucinotta, "Surface mode free and highly birefringent single-mode hollow core photonic bandgap fibers - art. no. 65880S," Photonic Cryst. Fibers **6588**, S5880 (2007). 17

[58] E. Fokoua, F. Poletti, and D. J. Richardson, "Analysis of light scattering from surface roughness in hollow-core photonic bandgap fibers." Opt. Express **20**, 20980–91 (2012). 20

[59] J.-m. Moison, J. A. Levenson, S. Richard, G. Mélin, and M. Douay, "Surface Roughness and Light Scattering in a Small Effective Area Microstructured Fiber," **27**, 1597–1604 (2009). 20

[60] X. Buet, C. Brun, G. Tessier, J. Gateau, B. Bresson, M. Ciccotti, R. Sandoghchi, E. N. Fokoua, M. Petrovich, F. Poletti, and D. Richardson, in ,20 (2016), 1, pp. 6–8.

[61] E. Numkam, F. Poletti, and D. Richardson, "Dipole radiation model for surface roughness scattering in hollow-core fibers," Natl. Fiber Opt. Eng. Conf. pp. 2–4 (2012). 20

[62] E. R. Numkam Fokoua, S. R. Sandoghchi, Y. Chen, N. V. Wheeler, N. Baddela, J. Hayes, M. Petrovich, F. Poletti, and D. J. Richardson, "Accurate Loss and surface mode modeling in Fabricated Hollow-core Photonic Bandgap Fibers," Opt. Fiber Commun. Conf. p. M2F.5 (2014). 20

[63] K. Zamani Aghaie, M. J. F. Digonnet, and S. Fan, "Modeling loss and backscattering in a photonic-bandgap fiber using strong perturbation," **8632**, 86320K (2013). 20

[64] M. Michieletto, J. K. Lyngsø, C. Jakobsen, O. Bang, and T. T. Alkeskjold, "Hollow-core fibers for high power pulse delivery," Opt. Express **24**, 7103–7119 (2016). 26, 35, 58, 71

[65] P. Uebel, M. C. Günendi, M. H. Frosz, G. Ahmed, N. N. Edavalath, J. Ménard, and P. S. J. Russell, in ,27 (2015), p. FW6C.2.

[66] F. Yu and J. C. Knight, "Negative curvature hollow-core optical fiber," IEEE J. Sel. Top. Quantum Electron. **22**, 4400610 (2016). 37

[67] M. Alharbi, T. Bradley, B. Debord, C. Fourcade-Dutin, D. Ghosh, L. Vincetti, F. Gérôme, and F. Benabid, "Hypocycloid-shaped hollow-core photonic crystal fiber Part II: cladding effect on confinement and bend loss," Opt. Express **21**, 28597–28608 (2013). 40

[68] C. J. Mattia Michieletto, Jens K. Lyngsø, "Hollow core optical fiber and a laser system," (unpublished) p. Patent Apllication: DK PA 2015 70877 (2015). 48, 89

[69] R. Holzlöhner, S. Burger, P. J. Roberts, and J. Pomplun, "Efficient optimization of hollow-core photonic crystal fiber design using the finite-element method," J. Eur. Opt. Soc. Rapid Publ. **1**, 06011 (2006). 54

[70] B. J. Mangan, L. Farr, A. Langford, P. J. Roberts, D. P. Williams, F. Couny, M. Lawman, M. Mason, S. Coupland, R. Flea, H. Sabert, T. a. Birks, J. C. Knight, and P. Russell, in ,54
(2004), p. PD24.

[71] M. Michieletto, J. K. Lyngsø, J. Lægsgaard, and O. Bang, "Cladding defects in hollow core fibers for surface mode suppression and improved birefringence." Opt. Express **22**, 23324–32 (2014). 58

[72] N. A. Mortensen and M. D. Nielsen, "Modeling of realistic cladding structures for air-core photonic bandgap fibers." Opt. Lett. **29**, 349–351 (2004). 59

[73] E. R. Numkam Fokoua, M. Petrovich, N. Wheeler, N. Baddela, J. R. Hayes, F. Poletti, and D. J. Richardson, "Predicting Structural and Optical Properties of Hollow-Core Photonic Bandgap Fibers from Second Stage Preforms," Opt. Fiber Commun. Conf. Fiber Opt. Eng. Conf. 2013 p. OTh1J.1 (2013). 59

[74] E. N. Fokoua, M. N. Petrovich, N. K. Baddela, N. V. Wheeler, J. R. Hayes, F. Poletti, and D. J. Richardson, "Real-time prediction of structural and optical properties of hollow-core photonic bandgap fibers during fabrication." Opt. Lett. **38**, 1382–1384 (2013). 59

[75] R. Calvani, R. Caponi, and A. N. D. F. Cisternin, "Polarization Measurements on Single-Mode Fibers," J. Light. Technol. **7** (1989). 65, 87, 88

[76] S. O. Konorov, V. P. Mitrokhin, A. B. Fedotov, D. a. Sidorov-Biryukov, V. I. Beloglazov, N. B. Skibina, A. V. Shcherbakov, E. Wintner, M. Scalora, and A. M. Zheltikov, "Laser ablation of dental tissues with picosecond pulses of 1.06-microm radiation transmitted through a hollow-core photonic-crystal fiber." Appl. Opt. **43**, 2251–2256 (2004). 71

[77] W. Göbel, A. Nimmerjahn, and F. Helmchen, "Distortion-free delivery of nanojoule femtosecond pulses from a Ti:sapphire laser through a hollow-core photonic crystal fiber." Opt. Lett. **29**, 1285–1287 (2004). 71

[78] G. Humbert, J. Knight, G. Bouwmans, P. Russell, D. Williams, P. Roberts, and B. Mangan, "Hollow core photonic crystal fibers for beam delivery." Opt. Express **12**, 1477–1484 (2004). 71

[79] J. Shephard, J. Jones, D. Hand, G. Bouwmans, J. Knight, P. Russell, and B. Mangan, "High energy nanosecond laser pulses delivered single-mode through hollow-core PBG fibers." Opt. Express **12**, 717–723 (2004). 71

[80] a. Urich, R. R. J. Maier, B. J. Mangan, S. Renshaw, J. C. Knight, D. P. Hand, and J. D. Shephard, "Delivery of high energy Er:YAG pulsed laser light at 2.94 Âμmthroughasilicahollowcorephotoniccrystalfibre.''*Opt.Express***20**, 6677 – –84(2012). 71

[81] A. Ouzounov, D.G., Ahmad, F.R., Müller, D., Venkataraman, N., Gallagher, M.T., Thomas, M.G., Silcox, J., Koch, K.W. and Gaeta, "Generation of megawatt optical solitons in hollow-core photonic band-gap fibers," Science **301**, 1702–1704 (2003). 71

[82] J. T. Kristensen, A. Houmann, X. Liu, and D. Turchinovich, "Fusion splicing of single-mode fibers and hollow-core photonic crystal fibers , relevant for monolithic fiber laser pulse compression," Opt. Express **16**, 9986–9995 (2008). 71

[83] F. Gérôme, K. Cook, a. K. George, W. J. Wadsworth, and J. C. Knight, "Delivery of sub-100fs pulses through 8m of hollow-core fiber using soliton compression." Opt. Express **15**, 7126–7131 (2007). 71

[84] P. J. Mosley, W. C. Huang, M. G. Welch, B. J. Mangan, W. J. Wadsworth, and J. C. Knight, "Ultrashort pulse compression and delivery in a hollow-core photonic crystal fiber at 540 nm wavelength." Opt. Lett. **35**, 3589–3591 (2010). 71

[85] D. C. Jones, C. R. Bennett, M. a. Smith, and a. M. Scott, "High-power beam transport through a hollow-core photonic bandgap fiber," Opt. Lett. **39**, 3122–3125 (2014). 71

[86] P. Jaworski, F. Yu, R. M. Carter, J. C. Knight, J. D. Shephard, and D. P. Hand, "High energy green nanosecond and picosecond pulse delivery through a negative curvature fiber for precision micro-machining," Opt. Express **23**, 8498 (2015). 71

[87] C. J. Saraceno, F. Emaury, A. Diebold, C. Schriber, B. Debord, F. Gérôme, T. Südmeyer, F. Benabid, and U. Keller, "Kagome-type hollow-core photonic crystal fibers for beam delivery and pulse compression of high-power ultrafast lasers," Proc. SPIE **9346**, 93460Z (2015). 71

[88] B. Debord, M. Alharbi, L. Vincetti, a. Husakou, C. Fourcade-Dutin, C. Hoenninger, E. Mottay, F. Gérôme, and F. Benabid, "Multi-meter fiber-delivery and pulse self-compression of milli-Joule femtosecond laser and fiber-aided laser-micromachining." Opt. Express **22**, 10735–46 (2014). 71

[89] C. Dumitrache, J. Rath, and A. Yalin, "High Power Spark Delivery System Using Hollow Core Kagome Lattice Fibers," Materials (Basel). **7**, 5700–5710 (2014). 71

[90] F. Emaury, C. J. Saraceno, B. Debord, D. Ghosh, A. Diebold, F. Gèrôme, T. Südmeyer, F. Benabid, and U. Keller, "Efficient spectral broadening in the 100-W average power regime using gas-filled kagome HC-PCF and pulse compression," Opt. Lett. **39**, 6843–6846 (2014). 71

[91] S. Pricking, R. Gebs, R. Fleischhaker, J. Kleinbauer, A. Budnicki, D. Sutter, A. Killi, S. Weiler, M. Mielke, B. Beaudou, B. Debord, F. Gerome, and F. Benabid, in ,71 , vol. 9356 (2015), vol. 9356, pp. 935602–1.

[92] M. C. Funck, B. Wedel, I. Kayander, and J. Niemeyer, "Industrial beam delivery system for ultra-short pulsed laser," Proc. SPIE **9356**, 935603–1 (2015). 71, 79

[93] M. M. Johansen, M. Laurila, M. D. Maack, D. Noordegraaf, C. Jakobsen, T. T. Alkeskjold, and J. Lægsgaard, "Frequency resolved transverse mode instability in rod fiber amplifiers," Opt. Express **21**, 21847–21856 (2013). 72

[94] F. Luan, J. Knight, P. Russell, S. Campbell, D. Xiao, D. Reid, B. Mangan, D. Williams, and P. Roberts, "Femtosecond soliton pulse delivery at 800nm wavelength in hollow-core photonic bandgap fibers." Opt. Express **12**, 835–840 (2004). 75

[95] M. D. Skeldon and R. Bahr, "Stimulated rotational Raman scattering in air with a high-power broadband laser," Opt. Lett. **16**, 366–368 (1991). 77, 80

[96] A. M. Zheltikov, "Raman response function of atmospheric air." Opt. Lett. **32**, 2052–2054 (2007). 77

[97] S. R. P. Thomas T. Alkeskjold, Jens K. Lyngsø, Christian Jakobsen, Martin D. Maack, Mattia Michieletto, "Photonic crystal fiber assembly," (unpublished) p. Patent Application: DK PA 2015 70876 (2015). 80

[98] V. N. Kumar and D. N. Rao, "Using interference in the frequency domain for precise determination of thickness and refractive indices of normal dispersive materials," J. Opt. Soc. Am. B **12**, 1559–1563 (1995). 84

[99] J. Y. Lee and D. Y. Kim, "Versatile chromatic dispersion measurement of a single mode fiber using spectral white light interferometry," Opt. Express **14**, 11608–11615 (2006). 84